Raman Spectroscopy of InAs based Nanowires & Electronic Characterization of Heterostructure InAs/GaInAs Nanowires

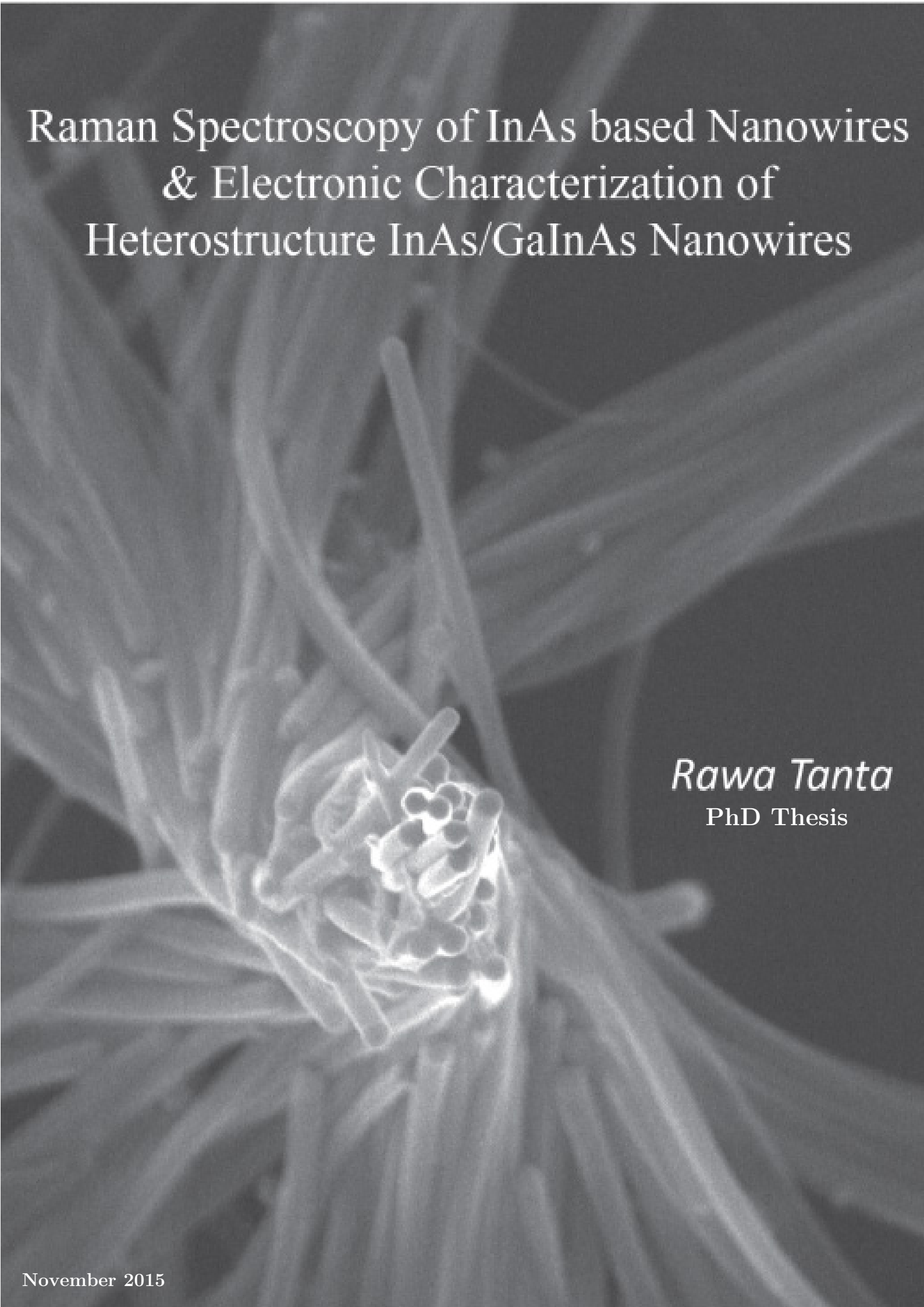

Rawa Tanta

PhD Thesis

November 2015

Raman Spectroscopy of InAs based Nanowires & Electronic Characterization of Heterostructure InAs/GaInAs Nanowires

Rawa Tanta

Ph.D. Thesis

Center for Quantum Devices

&

Nano Science Center

Niels Bohr Institute

Faculty of Science

Copenhagen University

Academic advisors:

Thomas Sand Jespersen & Jesper Nygård

November 2015

Table of Contents

Abstract

The work presented in this thesis represents two main topics. The first one, which covers a bigger volume of the thesis, is mainly about Raman spectroscopy on individual InAs based nanowires. The second part presents electronic characterization of heterostructure InAs/GaInAs nanowires.

Raman spectroscopy measurements on InAs based nanowires include several topics. Firstly, we use polarized Raman spectroscopy for determining the crystal orientation of the nanowires based on conventional Raman selection rules. We studied the effect of the high power laser irradiation on the nanowire, and its relation to the nanowire surface facets. We present controlled oxidation experiments on InAs nanowires enabled by fabrication of micro-trenches in the substrate and the electronic properties of the oxidized nanowire were also studied. Finally, we present an attempt to detect the LO phonon-plasmon coupled modes.

In the last chapter of this thesis we present a study on electrical characterization of InAs/GaInAs heterostructure nanowires. First, we performed selective etching experiments in order to locate the barriers. Second, the barriers were probed electrically by performing thermally activated transport measurements.

Resume

Denne phd afhandling beskriver to hovedemner. Det første, som optager hovedparten af afhandlingen, omhandler Raman spektroskopi udført på enkelte InAs-baserede nanotråde. Den anden del præsenterer elektriske målinger af heterostrukturerede InAs/GaInAs nanotråde.

Raman spektroskopien på InAs-baserede nanotråde berører flere aspekter. For det første udnytter vi polariseret Raman spektroskopi til at bestemme nanotrådenes krystal-orientering udfra sædvanlige Raman udvalgsregler. Vi undersøger effekten af intens bestråling med laserlys og relationen til nanotrådenes krystalfacetter. Vi viser desuden hvordan oxidation af nanotrådene kan kontrolleres ved hjælp af mikro-skala grøfter i substratet og de elektriske egenskaber af de oxiderede nanotråde studeres også. Endeligt præsenterer vi vores forsøg på at detektere fonon-plasmon koblede tilstande.

I afhandlingens sidste kapital beskriver vi elektrisk karakterisering af InAs/GaInAs heterostruktur nanotråde. Først udføres eksperimenter med selektiv ætsning for at lokalisere barrierne. Dernæst probes disse elektrisk ved termisk aktiverede transport-målinger.

Acknowledgments

Completing a PhD is a big step in a person's career path. During this exciting journey, which was an endless learning process, I grew up as a researcher. For this to happen essential elements had to come together to make it possible, was it the highly functional lab or the people around who had a huge influence on our daily life. I will always remember the nice discussions I had whether they were deep scientific ones or occasional chats at the coffee machine, which I am also grateful for! And now I would like to take the chance and thank those who had influenced my life as a PhD student. I had the privilege of being a part of a large group where we all do our lab work with harmony in a very well organized continuously functioning lab. This was possible by Charlie Marcus and Jesper Nygård. We so appreciate the huge efforts you are making to keep the lab running.

I want to thank again Jesper Nygård for being there along the way and all the support he has offered; without I don't think this would have been possible. Thanks for the freedom I had that enabled me to be independent and the constant mentorship you provided to keep me on the right track. Finally, I want to thank you for your understanding, kindness and patience.

When I was back from my maternity leave I had a nice chat with Thomas Sand Jespersen and from that a new turn was made. Thank you Thomas for introducing me to Tom and Raman spectroscopy! Working with you was a big pleasure and I've learned a lot from you; being a responsible researcher, how to design my experiments and to think outside the box. Also, I so admire how smart you are, always having new good ideas. In addition I am grateful to the person you are and the constant support I had from you. Working with Tom was a very joyful experience. I am very thankful for having access to your lab without restrictions and letting me build my electronic set-up on your microscope! Also thanks for your collaboration and your involvement in the strange world of nanowires! I would also thank Zhiyu Liao for the help I had during my Raman measurements.

I came to Kasper with my first working device and he got involved teaching me about electronic measurements. I am very grateful to you for your consistent presence in the lab during my measurements; it was very pleasant working with you. Since nanowires represent

the core of our work, a big thanks to the nanowires creators Peter and Morten; thank you for the variety of options we had besides the very fruitful discussions and collaborations.

I would also like to thank our collaborators in EPFL, Anna, Esther and Fransesca. My short visit to Lausanne was very memorable, the people there were very welcoming and supportive and I got to learn many new things by working in a different lab.

Here I would like to thank my friends in Qdev. A special thanks to Jessica Bolinsson; you were a huge support since you started in Qdev. Not only the good advices and the soft guidance but for the caring, responsible, smart and open person you are. It would have not been the same if it was not for you! Big thanks to Caroline Lindberg for being a very good friend and for all the "controversial" discussions we had. Besides, sharing an office with you was so much fun!. Thanks to Thomas Kanne for the TEM work he has done and Alexander Whiticar for proof reading a part of this work. I also want to thank; Erik Johnson, and for the nice chats and coffee breaks Joachim, Merlin, Guen, Charlotte, Sven and Morten. Katrine, thanks for being such a welcoming person and a friend; wish you the best in your future. The rest; Giulio, Jakob, Anders, Nina and Jeppe I wish you all good luck in your new career.

Being an experimentalist implies working in groups and I consider myself lucky for having such a dynamical group to work with. For this, I would like to thank Claus and Nader, you are the secret soldiers in the lab. Also, Shiv, your coordination skills and your passion to experimental work made our life easier, so thanks for your effort and for being a friend. A big thanks to Qdev administrative staff; you are doing a great job keeping things in order and coping with the increasing demands of our growing group. Jess, your extraordinary organization skills and high energy is remarkable. Katrin, your kindness and constant smile always made my day. Tina, thanks for your flexibility and gentleness. Really, you all are the candies you offer…!

Coming to Denmark and joining NBI would not have been possible if it was not for Per Hedegård, so thank you. I am also grateful to Henrik; may his soul rest in peace.

The way we make choices in our lives is hugely affected by our parents and the way we grow up. For this I am extremely thankful to my parents for having faith in me and for being responsible of the person I am; all who I am and what I achieved is due to both of you! The rest of the family thanks for all the small pieces that colored my life.

Last but not least, my little family. My beloved husband, friend, family, psychologist and companion Maher. All the love, care and support you gave me were a driving force for me to go on. Our consulting sessions on our way from and to daycare were priceless. I am glad that we are coming upon a new phase in our life and I am filled with hope that it will be more exciting and full of adventure as it always was. My little “flagermus heks” Reham; you filled our life with joy and actually helped us going through. I am really grateful for you; you gave us more than you took…!

Chapter I

1. Introduction

In the accelerating wheel of Nanotechnology, there is a constant competition between invention and production. As with the creation of new materials comes an obligation of new methods and techniques to characterize and device. Therefore, massive efforts are implemented in improving and revolutionizing characterization methods to cope with the highly advanced new material that have achieved already. An example of such advanced material of use is semiconductor nanowires (NWs) which were always of high attraction, due to the novel properties of semiconductors in addition to the confinement effect that the nanostructure provides. This had promoted semiconductor NWs to be a key element in devices with complex functionalities in areas ranging from chemical and biological sensing[1], optical devices and solar cells[2–5], next generation electronics[6] and quantum devices[7–9]. These advanced applications have generated the need for new fabrication techniques and characterization tools at the nanoscale. In this wide scope of research we focus on the characterization of InAs NWs using electronic and optical methods relevant to the probed element.

In this chapter we will list the outline of the thesis followed by a brief description of the nanowires investigated in this thesis. A short description of the growth mothed will be presented. The composition and the structure of the nanowires will also be described in details.

1.1 Outline of the thesis

A considerable amount of the work presented in this thesis is focused on Raman spectroscopy on InAs based NWs. In this chapter we will present the properties of the used NWs. In the second chapter we present basic theory of Raman spectroscopy in semiconductors. Chapter three illustrates the experimental details used in this thesis. The fourth chapter presents a study about the possibility of using polarized Raman spectroscopy in determining the crystal direction of the NW based on Raman selection rules for both

types of InAs NWs (zinc-blende and wurtzite). The fifth chapter studies the oxidation effect of high power Raman laser in the NWs. Here we analyze the oxidation resulted compounds by combination of Raman spectroscopy and transmission electron microscopy (TEM). We confirmed from Raman the existence of crystalline arsenic and that the observed modes violate the arsenic selection rules. From TEM analysis we detected poly-crystalline indium oxide. We also present surface-dependent oxidation effect by oxidizing InAs NWs with kinked geometry. In chapter six we show a controlled oxidation process enabled by substrate mico-trenches. The electronic measurements performed on the oxidized NWs showed that the NWs keep their semiconductor property with decrease in electric conductivity. Chapter seven presents an attempt to detect the LO plasmon-coupled modes of suspended InAs and core-shell NWs. The coupled modes were not observed in our spectra. Finally, we show electronic characterization experiments performed on axial heterostructure InAs/GaInAs NWs. The barrier formed due to bandgap offset is characterized by performing thermionic transport measurements on the NW.

1.2 InAs nanowires

Nanowires are nano-size objects which may be composed of a variety of materials and identified by their dimensions. Nanowires have two confined dimensions in the nanoscale while the third dimension has no restrictions. With this geometry NWs exhibit new properties, compared to bulk, which make them attractive elements in the future electronics, optics and quantum devices. Semiconductor NWs are of particular interest due to their discrete electronic states and material engineering flexibility. In particular, InAs NWs are one of the suitable candidates for advanced electronic devices, due to their unique properties such as: a direct small bandgap (0.35 eV), pinning of Fermi level at the surface[10], small effective mass ($m^*=0.023m_0$) and strong quantum confinement effects in thin NWs[11]. An example of NWs arrays (enabled by electron beam lithography) are presented in Figure 1.1.

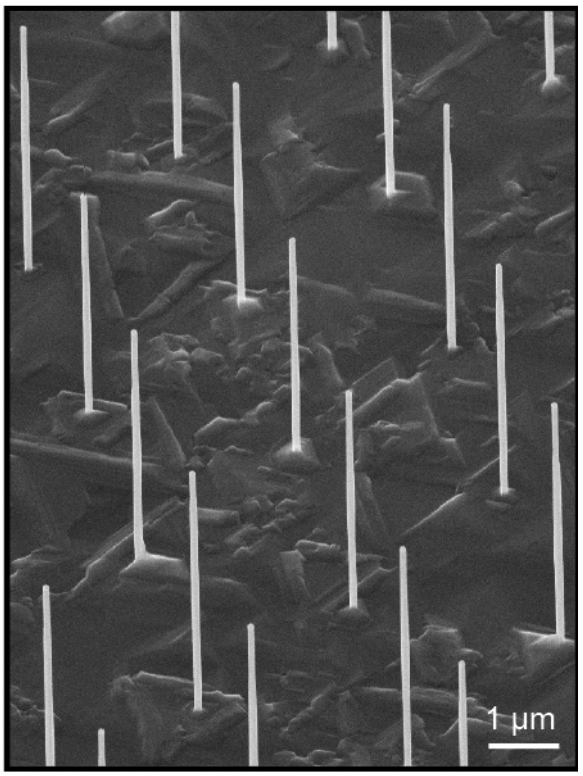

Figure 1.1 *Tilted SEM image of InAs nanowires arrays. Grown by Jessica Bolinsson*[*]*.*

Semiconductor NWs are generally grown in a system with multiple sources with the materials from which the NWs are composed[12,13]. One such system, in which the studied NWs in this thesis are grown, is Molecular Beam Epitaxy (MBE) where NWs can be grown via the Vapor-Liquid-Solid mechanism as one of the possible mechanisms (see Figure 1.2(a)). Nanowires are typically grown with a metal seed particle (metal seeded NWs) which has a catalytic effect on the growth process. Another approach is the growth of self-seeded NWs; an example of epitaxially growing self-seeded GaAs NWs is presented in Figure 1.2(b) and (c) where a Ga droplet drives the growth. For InAs NWs studied in this thesis, an InAs wafer is loaded to the MBE chamber and coated with a thin film of gold subsequently the wafer is

[*] Assistant Professor, Center for Quantum Devices & Nano-Science Center, Niels Bohr Institute. University of Copenhagen

heated until the gold forms droplets. Starting the flow of the desired material will initiate the growth of the NW.

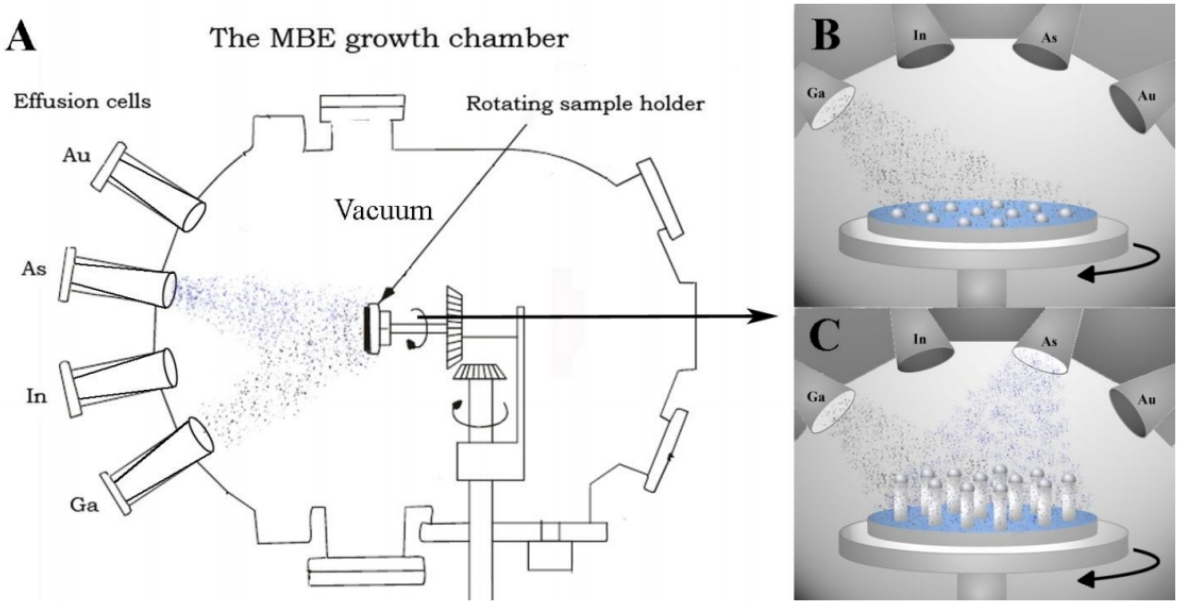

Figure 1.2 *(a) A schematic of the MBE chamber with typical sources cells. (B) and (c) Illustrate epitaxial growth of self-seeded GaAs NW. Adopted from reference*[14].

The crystal structure of InAs NWs can either be a cubic zinc-blende (ZB) structure, which is the same as bulk InAs, or a hexagonal wurtzite (WZ) structure. The two structures are mainly distinguished by their atomic stacking sequence along the <111> and <0001> crystal direction for the ZB and WZ structure, respectively. As illustrated in Figure 1.3 (adapted from referecne[15]) the ZB phase has a stacking of ABCABC, where each letter represents the bilayer of the group III and V atoms vertically aligned as one unit. The WZ structure has the stacking sequence ABAB instead. Nanowires can be found in pure ZB or WZ phases based on growth conditions or in a mixture of the two[13,16,17]. An interruption of the stacking sequence is normally denoted as a stacking fault, which can either be a repeated rotation in the atomic layer along the NW "twining" or presence of WZ layer in ZB dominant structure NW and vice a versa so-called "polytypism". These faults can appear randomly in a NW or can be controlled to engineer the electronic band structure of the NW.

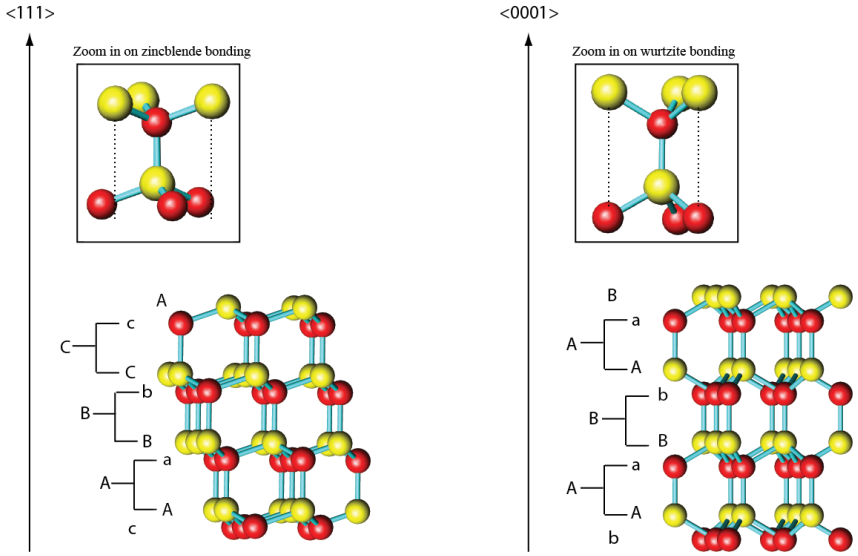

a) b)

Figure 1.3 *(a) and (b) The atomic structure of the ZB and WZ crystal phases, respectively. Adopted from referecne*[15].

1.3 List of the measured nanowires

Several types of InAs based NWs were investigated in the work presented in this thesis. Pure InAs NWs, core-shell InAs/InGaAs NWs and kinked InAs NWs were used for the Raman experiments, presented in chapters 4, 5, 6 and 7, while axial heterostructured InAs/$In_{1-x}Ga_xAs$/InAs NWs are investigated in chapter 8. A brief description of the NWs studied in this thesis will be listed in the following:

- Conventional InAs NWs were grown with dominant wurtzite crystal structure along the **[0001]** crystal direction. These NWs are tapered with diameter of ~40-140 nm from top to bottom and length of ~ 7 µm. TEM images of several NWs showed that wires differ in their crystal phase purity, since they contain a high density of stacking faults or have none (Figure 1.4).

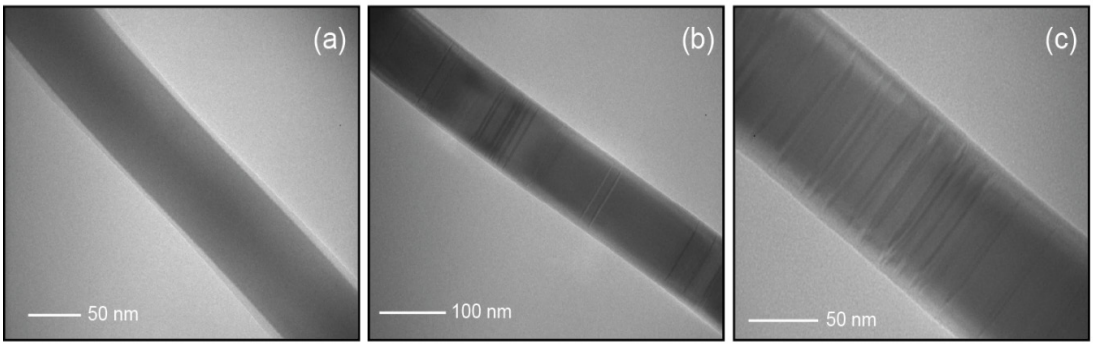

Figure 1.4 *TEM images of InAs NWs. (a) NW free of stacking faults. (b) and (c) NWs with stacking faults.*

- Core-shell InAs/$Ga_xIn_{1-x}As$ NWs were grown along the **[0001]** crystal direction. First, a conventional InAs stem is grown. Subsequently, a radial growth of ~5 nm $In_{1-x}Ga_xAs$ shell is promoted. Typical NW length and diameter are ~5 µm and ~120 nm, respectively.
- Kinked InAs NWs. Initially, ~1 µm long stems with diameter of ~100 nm were grown along the **[0001]** direction. Then, a pulse of Ga flux induces a shift of the gold droplet to a side facet of the stem, prompting the growth of a perpendicular branch along the **[01$\bar{1}$0]** direction, as illustrated in Figure 1.5(a). The branch has a length of ~2 µm and a diameter of ~80 nm. A TEM image of a representative NW is shown in Figure 1.5(b). It was noticed that the **[0001]** segment has plenty of stacking faults and these faults are inherited along the **[01$\bar{1}$0]** segment.

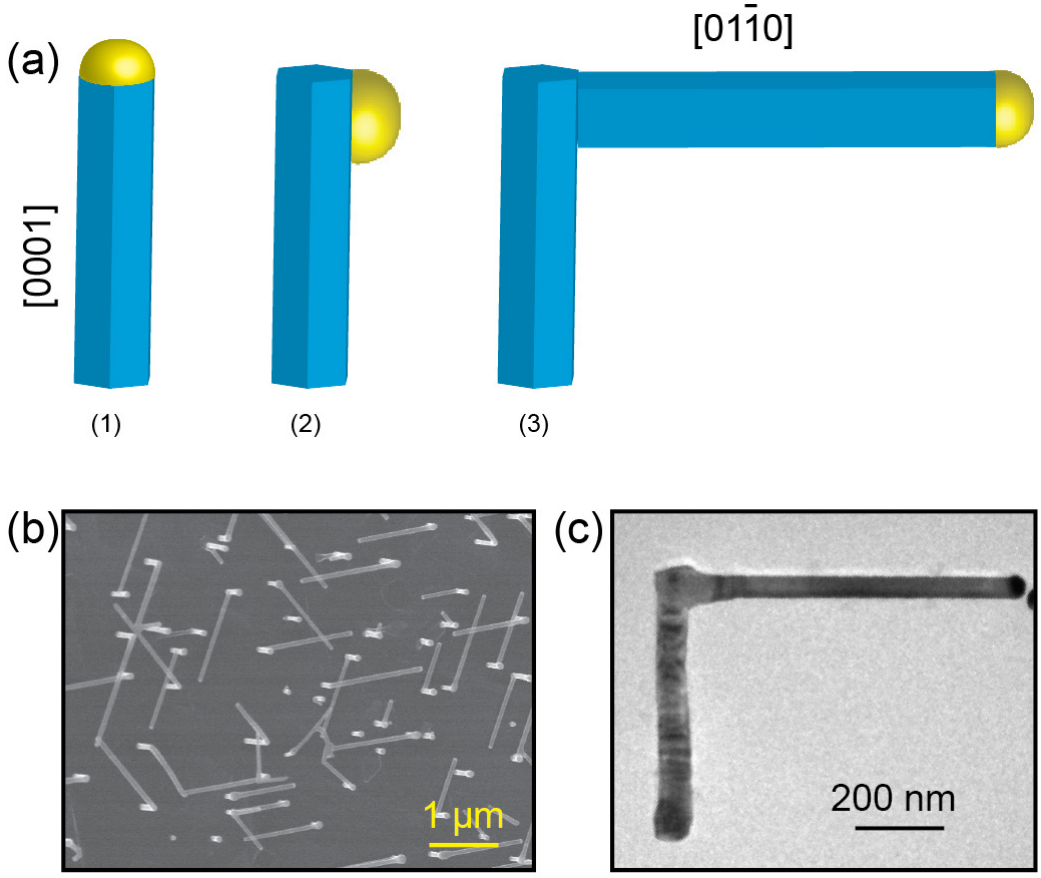

Figure 1.5 *(a) A schematic illustration of the growth steps of kinked InAs NW. (b) top view SEM image of the nanowires. (c) TEM image of a branched NW.*

- Heterostructure InAs/$Ga_xIn_{1-x}As$/InAs NWs. Growth started with conventional InAs stems followed by axial growth of $Ga_xIn_{1-x}As$ segments, initiated by Ga flux. Then, pure InAs segments were grown axially. Based on energy-dispersive x-ray (EDX) spectroscopy the Ga mole fraction x of the $Ga_xIn_{1-x}As$ segment is estimated to be ~0.1. A TEM image of a heterostructure NW is presented in Figure 1.6.

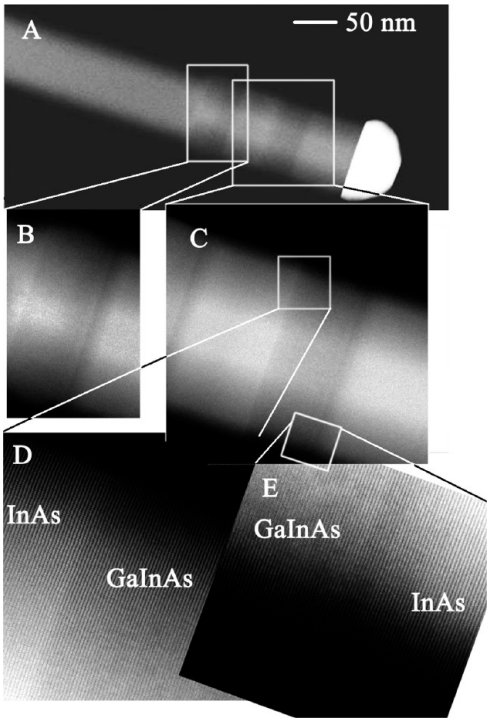

Figure 1.6 *TEM images of InAs/Ga_xIn_{1-x}As nanowire with two GaInAs segments. Reprinted from reference*[18].

There are two types of heterostructure NWs studied in this thesis. The first type contains 4 $Ga_xIn_{1-x}As$ segments that are ~20 nm long and equally separated as shown in the SEM image of a selectively etched NW presented in Figure 1.7. The NWs are ~4-7 µm in length and with ~120 nm diameter. The second type contains only a single $Ga_xIn_{1-x}As$ segment which has the same properties of the first type. A More detailed discussion of these NWs will be presented in chapter 8.

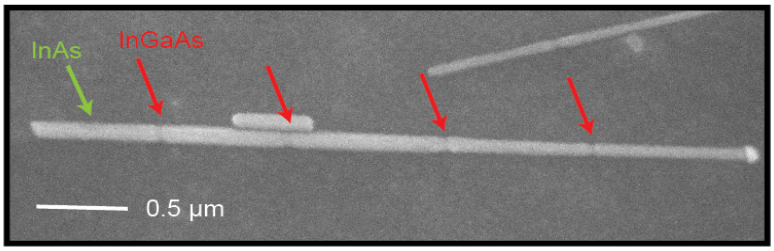

Figure 1.7 *SEM image of a selectively etched InAs/$In_{1-x}Ga_xAs$/InAs NW, where four barriers can be distinguished (indicated by red arrows).*

Chapter II

2. Introduction to Raman Spectroscopy of InAs nanowires

In this chapter we will present a classical basic introduction to the vibrational modes in the WZ and ZB crystal structure. We will also list the selection rules of those modes based on the crystal symmetry properties using group theory. We further introduce the reader to the Raman spectroscopy concept and the Raman selection rules. If the reader is interested in more details they are referred to references[19,20] where the material presented in this chapter are mainly based on.

2.1 Vibrational modes of wurtzite and zinc-blende InAs NWs

In a crystal having N atoms in the primitive unit cell, an excitation would cause collective oscillations with 3N normal modes of vibration. A quantized mode of vibration with energy $\hbar\omega_q$ and wavevector $\vec{q}$ is called a phonon. The normal modes of a crystal consist of 3 acoustic modes where atoms vibrate in-phase and 3N-3 optical modes where atoms vibrate out of phase. One can also distinguish two types of vibrations in both optical and acoustic vibrations, namely Transverse (TA and TO) and Longitudinal (LA and LO) modes, when the atoms displacements are transverse and parallel to the propagation direction, respectively. In polar crystals, where charge is not evenly distributed between neighboring atoms an additional Coulombic restoring force will affect the LO phonon modes which causes a TO-LO splitting, where the TO and LO modes splits into two different frequencies. The splitting magnitude is determined by Lyddane-Sachs-Teller relationship $\frac{\varepsilon_0}{\varepsilon_\infty} = \frac{\omega_L^2}{\omega_T^2}$, where ω_L and ω_T are the frequencies of the LO and TO modes, respectively, and ε_0 and ε_∞ are the low and high frequency dielectric constants of the material, respectively. These modes are dependent on the crystal structure and its symmetries, which will be discussed in the next paragraph.

Symmetry properties of crystals simplify the calculation of their electronic states and phonons, since the Brillouin zone remains invariant when applying a certain number of rotations and reflections (symmetry operations). When a crystal property such as an electronic state that has been transformed according to a symmetry operation remain unchanged it is called equivalent. The classification of crystal properties according to their symmetrical transformation operations can be done using group theory, where the symmetry operations will constitute the group of interest. In the following, a brief presentation of the use of group theory in determining the vibrational modes in the ZB and WZ crystal structure will be given.

The zinc-blende structure of a polar semiconductor with two atoms the primitive cell can be considered as two face-centered cubic lattices displaced relative to each other by a vector $\mathsf{a_0}/4.\,(1,1,1)$ where $\mathsf{a_0}$ is the lattice constant. Each atom is surrounded by four nearest neighbors forming a tetrahedron. This structure has 24 symmetry operations which are[19]:

E	the identity
C_3	eight clockwise and counterclockwise rotations of 120° about the $[111]$, $[\bar{1}11]$, $[1\bar{1}1]$, and $[11\bar{1}]$ axes, respectively
C_2	three rotations of 180° about the $[100]$, $[010]$, and $[001]$ axes, respectively
S_4	six clockwise and counterclockwise improper rotations of 90° about the $[100]$, $[010]$, and $[001]$ axes, respectively
σ	six reflections with respect to the (110), $(1\bar{1}0)$, (101), $(10\bar{1})$, (011), and $(01\bar{1})$ plans, respectively

These symmetry operations forms the $\mathsf{T_d}$ point group (a group of symmetry operations in the unit cell) which belong to the $\mathsf{T_d^2}$ or ($\mathsf{F\bar{4}3m}$) space group (a point group with the translational symmetry operations of the unit cell).

A symmetry operation, applied on a coordinate system, can be represented by a matrix, which transforms the coordinates according to the symmetry operation. For example, a four-

fold rotation about the x axis would transform x, y, and z into x'=x, y'=z, z'=-y and the matrix M representing this operation is:

$$M = \begin{pmatrix} 1 & 0 & 0 \\ 0 & 0 & 1 \\ 0 & -1 & 0 \end{pmatrix}$$

Often the notation $(xyz) \rightarrow (xz\bar{y})$ is used. All other symmetry operations can be represented by a similar matrix. These matrices or their combinations form a group, which is known as a representation. In the following some definitions about the representation group will be listed:

- *Order* of a group: the number of elements (symmetry operations) in the group, which is 24 for the Zinc-blende case.
- Reducible and *irreducible* representation: a block form that contains all the matrices in the group is called to be reducible representation. This reducible representation can be decomposed into irreducible matrices, which will form an irreducible representation.
- *Basis:* the set of functions that transform according to each irreducible representation.
- *Characters*: the traces (the sum of the diagonal elements) of an irreducible transformation matrix. Equivalent operations have the same character.
- *Class* of the group: the group of elements of the same operation, which also have the same character. The number of inequivalent irreducible representations of a group is equal to the number of classes. The zinc-blende structure, at the Γ point of Brillouin zone, has 5 classes leading to 5 irreducible representations which are according to BSW[†] notations ($\Gamma_1, \Gamma_2, \Gamma_{12}, \Gamma_{15}$ andΓ_{25}) or in molecular notations (A_1, A_2, E, T_1, T_2).
- *Character table*: is the table of the characters of classes for each irreducible representation and their basis functions. It has an equal number of rows and columns (equal to the number of classes). The character table of the zinc-blende structure with

[†] Bouckaert, Smoluchowski, and Wigner

its basis functions (which might be found in different forms in other references) is listed in

- [19]. The characters of $\{E\}$ represent the dimensions of each irreducible representation. The character table elements can be found by inspection using the orthogonality relations which are:

$$\sum_k \chi_i(C_k)^* \chi_j(C_k) N_k = h\delta_{ij} \tag{1.1}$$

$$\sum_i \chi_i(C_k)^* \chi_i(C_l) = (h/N_l)\delta_{kl} \tag{1.2}$$

where χ_i is the character of class C_k with number of elements N_k, h is the order of the group and δ_{ij} is the Kronecker delta, and * denotes the complex conjugate. Equations (1.1) and (1.2) can be realized by applying them on each row and column of the character table respectively.

Table 2.1 *The character table and the basis functions of the T_d point group (zinc-blende structure). Adopted from reference*[19]

	$\{E\}$	$\{3C_2\}$	$\{6S_4\}$	$\{6\sigma\}$	$\{8C_3\}$	Basis functions
Γ_1	1	1	1	1	1	x^2+y^2, z^2
Γ_2	1	1	-1	-1	1	$x^4(y^2-z^2)+y^4(z^2-x^2)+z^4(x^2-y^2)$
Γ_{12}	2	2	0	0	-1	$\left\{(x^2-y^2), z^2-\frac{1}{2}(x^2+y^2)\right\}$
Γ_{15}	3	-1	1	-1	0	$(x,y,z),(xy,xz,yz)$
Γ_{25}	3	-1	-1	1	0	$\{x,y,z\}$

Regarding crystal vibrational modes, the basis functions in the character table determine if a mode, associated with an irreducible representation, is IR (Infrared) or Raman active mode. A vibrational mode is IR active when the basis function is linear with x, y and z. On the other hand, a mode associated with a representation which at least for one of its basis functions is a second order of x, y, z, like x^2, xy, zy, etc., is Raman active[20]. The irreducible representations with higher order functions are associated with silent modes. At

the center of the Brillouin zone, a vibration includes the nearly uniform displacements of identical atoms in all unit cells. Since the primitive cell of the ZB structure contains two atoms, a vibrational mode at the zone center can be specified by two vectors. These vectors correspond to the displacement of each atom and they can transform according to the Γ_{15} irreducible representation. Hence, the six normal modes of the zinc-blende crystal belong to the Γ_{15} irreducible representation as $2\Gamma_{15}$. Three of these modes are acoustic, and the rest are optical modes. The optical modes are two degenerate transvers modes and one longitudinal mode, whose frequencies values for InAs are listed in Table 2.2.

Table 2.2 *Zone center Raman active modes frequencies for InAs at room temperature.*

	TO (cm^{-1})	LO (cm^{-1})
InAs	216	237

As discussed above, InAs NWs can also exist in the WZ structure, with its cohesive energy being very close to that of the ZB. Similarly, one can define the character table and vibrational modes. The primitive cell of the WZ structure contains four atoms and the lattice structure consists of two hexagonal lattices displaced by $\vec{u} = [\frac{1}{3}(2\vec{a}_1 + \vec{a}_2) + \frac{\vec{c}}{2}]$, where $\vec{a}_1$, $\vec{a}_2$ and $\vec{c}$ are the vectors describing the primitive cell. The space group of the wurtzite structure is C_{6v}^4 which has 12 symmetry operations divided into 6 classes. The symmetry operations of the wurtzite structure are listed below:

E the identity

C_2 180° rotation about the c-axis[‡] followed by a translation by the vector (0,0,c/2), which means this is a screw axis operation

C_3 two clockwise and anticlockwise 120° rotations about the c axis

[‡] The c-axis is along the [0001] crystal direction

C_6 two clockwise and counterclockwise 60° rotations about the c axis, followed by translation by the vector (0,0,c/2)

σ_d three reflections in the symmetry plans normal to $\vec{a}_1$, $\vec{a}_2$, and $\vec{a}_1 + \vec{a}_2$, respectively, with translation by the vector (0,0,c/2)

σ_v three reflections in the symmetry plans along the $\vec{a}_1$, $\vec{a}_2$, and $\vec{a}_1 + \vec{a}_2$, respectively

The six classes of the WZ structure imply that it has six irreducible representations which are often labeled as: A_1, A_2, B_1, B_2, E_1 and E_2. The characters associated with these irreducible representations, at the zone center, and their functions are listed in Table 2.3. The basis functions imply that the modes associated with the A_1 and E_1 are both Raman and IR active, while the mode associated with E_2 representation is Raman active, and the modes assigned to the A_2, B_1 and B_2 are silent modes.

Table 2.3 *The character table and its basis functions of the wurtzite crystal structure*

	$\{E\}$	$\{2C_6\}$	$\{2C_3\}$	$\{C_2\}$	$\{3\sigma_v\}$	$\{3\sigma_d\}$	Basis functions
A_1	1	1	1	1	1	1	x^2+y^2, z^2, z
A_2	1	1	1	1	-1	-1	
B_1	1	-1	1	-1	1	-1	
B_2	1	-1	1	-1	-1	1	
E_1	2	1	-1	-2	0	0	$(xz, yz), (x, y)$
E_2	2	-1	-1	2	0	0	(x^2-y^2, xy)

The total representation at the zone center can be decomposed into irreducible representations presented in equation (1.3)

$$\Gamma_{tot} = 2A_1 + 2B_1 + 2E_1^{(2)} + 2E_2^{(2)} \tag{1.3}$$

The superscripts indicate the double degeneracy of the E_1 and E_2 modes. Unlike the ZB case the vibrational modes are associated with different symmetry representations. These modes are the three acoustic modes A_1 and $E_1^{(2)}$, and the Raman active modes $\boldsymbol{A_1}$, $\boldsymbol{E_1}$ (polar modes)

and E_2. As mentioned before, the A_2, B_1 and B_2 are silent modes. The atomic displacements of the vibrational modes in the WZ structure are depicted in Figure 2.1, where the A_1 mode vibrates along the c-axis ([0001]), and the E_1 and E_2 modes vibrate in the perpendicular plane.

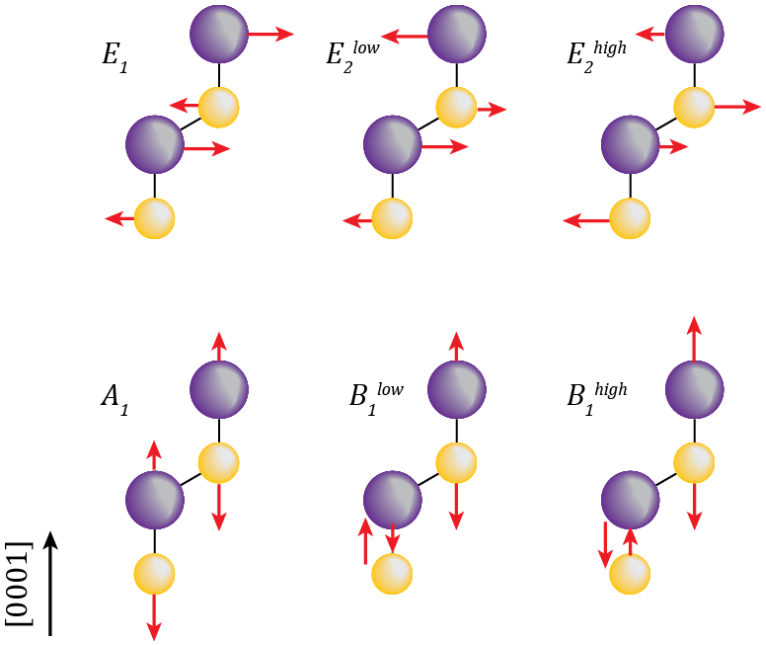

Figure 2.1 *Atomic displacements of the zone-center optical vibrational modes in WZ structure. Adapted from reference* [20]

Since bulk InAs has only the ZB structure, the frequencies of the zone-center optical modes of the WZ InAs NWs are listed in Table 2.4[21]

Table 2.4 *Raman active phonon frequencies of InAs in the WZ structure*[21].

WZ InAs	E_2^{low}	E_2^{high}	$A_1(TO)$	$E_1(TO)$	$A_1(LO)$	$E_1(LO)$
(cm^{-1})	43.6	219.2	225.5	226.0	246.3	246.8

The table shows that the values of the $A_1(LO)$ and $E_1(LO)$ are very close to each other and can hardly be resolved, and the $A_1(TO)$ and $E_1(TO)$ modes are only different by 0.5 cm^{-1}.

Also, the value of the $A_1(TO)$ and $E_1(TO)$ modes of the WZ structure are very close to the TO and LO modes of the ZB structure. In general, Raman peaks of the ZB and WZ structure of the same material are very similar and a high resolution detection set-up is required to resolve the A_1 and E_1 modes of the WZ structure. Otherwise the detected spectra will contain an overlap of the two modes in non-polarized measurements. This will be discussed in more detail in the following chapters.

2.2 Raman Spectroscopy

Different interactions may occur between an incident light and a medium (Figure 2.2). Most of the incident light is reflected or transmitted into the medium, while, with very low probability, some of the transmitted light gets reemitted with different energy (this process is known as photoluminescence), or may be scattered by inhomogeneities. Scattering by elementary excitations such as optical phonons is known as ***Raman scattering***. The latter scattering is inelastic scattering with a very low intensity (factor of 10^6 weaker) compared to the elastic scattering. The Raman scattering is conventionally used to probe the vibrational modes of a material which can in turn be used to identify the material composition. In crystals Raman scattering can also probe the vibrational modes besides the crystal purity and orientation.

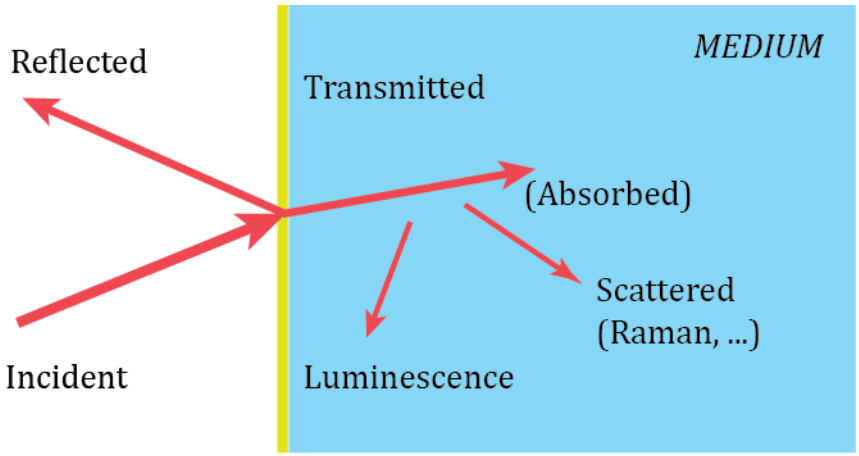

Figure 2.2 *Schematic diagram of the linear optical processes occur in a medium, assuming that light comes from vacuum. Adapted from reference*[19].

2.2.1 Historical review

Since Raman spectroscopy is only rarely used in the field of nanowire research we will give a brief introduction to its historical background.

After the publication of C.V. Raman Nature paper '*A New Type of Secondary Radiation*' in 1928[22], there was a huge focus on Raman experiments. Over 1757 papers were published by the year 1939[23]. The progress was limited and, eventually, slowed down due to the use of the mercury vapor lamp as an excitation light source. Keeping in mind that the inelastic Raman scattering is very week compared to the elastic Rayleigh scattering, a high illumination source is required. The low energy lines of the vapor mercury lamp (maximum 1 eV=8066 cm^{-1}) excluded Raman measurements of most crystals, especially semiconductors. By the invention of laser in 1960[24] Raman experiments were accelerated again. The first published laser Raman Spectroscopy paper in 1962[25], which used a ruby pulsed laser as an excitation source, was the beginning of the new phase of Raman Spectroscopy. Ever since, the rapid development of lasers provided excitation sources with wide range of spectral lines. This made Raman an appropriate characterization tool for most types of materials. On the other hand, the optics used in Raman experiments were also dramatically improving over time, where currently a laser spot of sub-micrometer diameter is routinely used in a μ-Raman set up.

The submicron laser beam size validates Raman spectroscopy as a proper characterization tool to investigate nanostructures including nanowires. This opens the door for the development of Raman experiments to study, in details, NWs structures. As InAs NWs are of our interest we will continue tracking the published Raman experiments on InAs NWs, which are in fact rather limited. Raman spectroscopy was initially used to characterize the structure of GaAs and InAs NWs in 2008[26]. Three years later, three articles on InAs NWs were published. The confinement effect on optical phonons was presented by M. Cantoro et al[27]. It was found that there is no confinement effect and a surface optical (SO) mode was observed. M. Möller et al[21] presented a detailed study of Raman spectroscopy on InAs NWs with WZ and ZB crystal structures. Polarization dependent Raman measurements, resonant Raman spectroscopy and the detection of surface optical mode were also presented. N. G. Hörmann et al[28] presented a Raman study of the stacking variation in InAs NWs. Raman spectra were recorded for different stacking sequences with WZ and ZB

inclusions. A shift in the TO mode, besides a violation of the bulk selection rules was observed. In 2012, another work was presented by J. K. Panda et al[29] where Raman spectroscopy combined with TEM investigation were used to estimate the wurtzite structure in mixed phased NWs. Lately, Raman spectroscopy has also been used as one of the applied techniques to investigate the growth quality of the NWs[30,31]. Interestingly, resonant Raman experiments were conducted on wurtzite NWs by I. Zardo et al[32], where an unusual method was followed to achieve resonance, either conventionally by tuning the laser wavelength, or by modifying the band gap by applying an external pressure at fixed laser wavelength. The measured Raman spectra showed a reduction in the band gap of wurtzite NWs compared to zinc-blende InAs. Later in 2014, S. Yazji et al[33] published pressure dependent Raman measurements on InAs NW.

laser modification of InAs NWs by Raman measurements was presented by S. Pal et al[34]. Power dependent Raman measurements showed the appearance of new peaks, different from the conventional InAs modes, which were mainly assigned to crystalline arsenic as one of the compounds resulting from oxidation process. In the short review presented above, the following points can be pointed out: First, all measurements were either performed on ensembles of NWs on their growth substrate, or individual NWs deposited on Silicon wafers. Second, none of the above performed TEM analysis on the same NWs measured by Raman. In this case, the TEM analyzed structures could vary from the ones measured by Raman, considering the dissimilarity between NWs, even in the same batch.

2.2.2 The Raman Effect in semiconductors and selection rules

Polarized Raman spectroscopy is widely used to determine crystal orientation. Where the crystal direction of a probed surface can be identified using the polar maps of the intensity of the Raman spectra as a function of the incident and scattered light polarization angel. A classical preview of the origin of the Raman selection rules is presented in the following section and the Raman tensors of the ZB and WZ crystal structures, used in chapter 4, will be listed.

From a macroscopic point of view, let us consider an infinite medium with the electric susceptibility$\chi(\vec{k}_i, \omega_i)$, which is a second rank tensor determined by the electronic structure of the crystal. When exposing the medium to an electromagnetic field of the form[19]

$$\vec{F}(\vec{r},t) = \vec{F}_i(\vec{k}_i,\omega_i)\cos(\vec{k}_i.\vec{r} - \omega_i t) \tag{2.4}$$

a sinusoidal polarization $\vec{P}(\vec{r},t)$, with the same frequency and wavevector as the incident wave, will be induced where

$$\vec{P}(\vec{r},t) = \vec{P}(\vec{k}_i,\omega_i)\cos(\vec{k}_i.\vec{r} - \omega_i t) \tag{2.5}$$

$$\vec{P}(\vec{k}_i,\omega_i) = \chi(\vec{k}_i,\omega_i)\vec{F}_i(\vec{k}_i,\omega_i) \tag{2.6}$$

At finite temperature, the atomic displacements $\vec{Q}(\vec{r},t)$, associated with the normal vibration modes, can be expressed as a plane wave of the from

$$\vec{Q}(\vec{r},t) = \vec{Q}(\vec{q},\omega_0)\cos(\vec{q}.\vec{r} - \omega_0 t) \tag{2.7}$$

with the wavevector $\vec{q}$ and the frequency ω_0. In a quasi-static approximation, where the characteristic electronic frequencies which determine χ are much larger than ω_0, χ can be a function of $\vec{Q}$. Normally, the phonon amplitudes are much smaller than the lattice constant, normally. This enables expansion of χ as a Taylor series in $\vec{Q}(\vec{r},t)$ as follows:

$$\chi(\vec{k}_i,\omega_i,\vec{Q}) = \chi_0(\vec{k}_i,\omega_i) + \left(\frac{\partial\chi}{\partial\vec{Q}}\right)_0 \vec{Q}(\vec{r},t) + \cdots \tag{2.8}$$

The first term in equation (2.8) represents the static susceptibility, while the second term represents the oscillations induced by the lattice displacement vector. If we substitute (2.8) into (2.6) the polarization with atomic vibrations included will be expressed as

$$\vec{P}(\vec{r},t,\vec{Q}) = \vec{P}_0(\vec{r},t) + \vec{P}_{ind}(\vec{r},t,\vec{Q}) \tag{2.9}$$

where $\vec{P}_0(\vec{r},t)$ is the polarization vibrating in-phase with the incident electromagnetic wave, which is expressed by:

$$\vec{P}_0(\vec{r},t) = \chi_0(\vec{k}_i,\omega_i)\vec{F}_i(\vec{k}_i,\omega_i)\cos(\vec{k}_i.\vec{r} - \omega_i t) \tag{2.10}$$

On the other hand, the polarization induced by atomic vibrations $\vec{P}_{ind}(\vec{r},t,\vec{Q})$ is

$$\vec{P}_{ind}(\vec{r},t,\vec{Q}) = \left(\frac{\partial\chi}{\partial\vec{Q}}\right)_0 \vec{Q}(\vec{r},t)\vec{F}_i(\vec{k}_i,\omega_i)\cos(\vec{k}_i.\vec{r} - \omega_i t) \tag{2.11}$$

Here, the contribution from the macroscopic electric field associated with the LO phonon will not be considered. Substituting $\vec{Q}(\vec{r},t)$ in (2.7) into (2.11) we will get the following form of the induced polarization

$$\vec{P}_{ind}(\vec{r},t,\vec{Q}) = \left(\frac{\partial\chi}{\partial\vec{Q}}\right)_0 \vec{Q}(\vec{q},\omega_0)\cos(\vec{q}.\vec{r} - \omega_0 t)\vec{F}_i(\vec{k}_i,\omega_i)\cos(\vec{k}_i.\vec{r} - \omega_i t) \tag{2.12}$$

$$\begin{aligned}\vec{P}_{ind}(\vec{r},t,\vec{Q}) = \frac{1}{2}\left(\frac{\partial\chi}{\partial\vec{Q}}\right)_0 \vec{Q}(\vec{q},\omega_0)\vec{F}_i(\vec{k}_i,\omega_i)\{&\cos[(\vec{k}_i + \vec{q}).\vec{r} - (\omega_i + \omega_0)t] \\ &+ \cos[(\vec{k}_i - \vec{q}).\vec{r} - (\omega_i - \omega_0)t]\}\end{aligned} \tag{2.13}$$

Equation (2.13) shows that the induced polarization consists of two sinusoidal waves. Those waves are the *Stokes* shifted waves, for $\vec{k}_S = (\vec{k}_i - \vec{q})$ and $\omega_S = (\omega_i - \omega_0)$ and the *anti-Stokes* shifted waves, for $\vec{k}_{AS} = (\vec{k}_i + \vec{q})$ and $\omega_{AS} = (\omega_i + \omega_0)$. The scattered radiations will have a shift in the frequency, namely, stokes and anti-stokes shifts. This shift is called the

Raman frequency or the *Raman shift*. In Raman spectra, the inelastic scattering intensity is measured versus the Raman shift. In this work only the stokes shifts will be measured. The measured Raman intensity is the time integrated power of the radiations coming from the induced polarization into a unit solid angle. This intensity depends on the induced polarization $\vec{P}_{ind} \propto \left(\frac{\partial \chi}{\partial \vec{Q}}\right)_0 \vec{Q}(\omega_0)$ and the unit vector of the incident e_i and scattered e_s light polarization according to the formula

$$I_s \propto \left| e_i . \left(\frac{\partial \chi}{\partial \vec{Q}}\right)_0 . \vec{Q}(\omega_0) . e_s \right|^2 \tag{2.14}$$

Here we approximate $\vec{q} \approx 0$ due to wave vector conservation laws, considering that excitation laser emission is in the optical range and that in semiconductors the maximum value of q is in the order of 10^6 cm^{-1} which is much smaller than the boundary of the corresponding Brillouin zone. Therefore, the one-phonon scattering process occurs at the center of Brillouin zone. Here we define the Raman tensor as

$$R = \left(\frac{\partial \chi}{\partial \vec{Q}}\right)_0 . \hat{Q}(\omega_0) \tag{2.15}$$

where a unit vector parallel to the phonon displacement is defined as

$$\hat{Q}(\omega_0) = \vec{Q}/|\vec{Q}| \tag{2.16}$$

The Raman tensor defined in equation (2.15) is a second-rank tensor with complex components which correspond to the induced atomic displacements. This leads us to the well-known form of the Raman intensity

$$I_s \propto |e_i . R . e_s|^2 \tag{2.17}$$

Equation (2.17) is usually used to derive the selection rules of polarized Raman spectroscopy, where the Raman scattering is allowed when $I_s \neq 0$. We will get back to this later. For now we will present the Raman tensors for our ZB and WZ structures. These tensors can be directly obtained from the character tables discussed in section 0. For the ZB structure, the zone center optical phonons transform according to the Γ_{15} irreducible representation, whose basis functions determine the non-zero components of the Raman tensor. More details of how to extract the Raman tensors can be found in reference[19]. The optical phonons of the ZB structure are triply degenerate and they have the following Raman tensors along the main crystal axes [100], [010], and [001] which are denoted by x, y and z, respectively:

$$R_{e_1} = \begin{pmatrix} 0 & 0 & 0 \\ 0 & 0 & d \\ 0 & d & 0 \end{pmatrix} \quad , \quad R_{e_2} = \begin{pmatrix} 0 & 0 & d \\ 0 & 0 & 0 \\ d & 0 & 0 \end{pmatrix} \quad , \quad R_{e_3} = \begin{pmatrix} 0 & d & 0 \\ d & 0 & 0 \\ 0 & 0 & 0 \end{pmatrix} \tag{2.18}$$

where d is a constant related to the crystal. In polar semiconductors d becomes different for the TO and LO mode (due to the splitting induced by the macroscopic electric field associated with the LO mode as mentioned earlier). In practice, d is used for both the selection rules calculations. Likewise, one can list the Raman tensors for the Raman active optical modes for the WZ structure

$$E_1(x) = \begin{pmatrix} 0 & 0 & c \\ 0 & 0 & 0 \\ c & 0 & 0 \end{pmatrix} \quad , \quad E_1(y) = \begin{pmatrix} 0 & 0 & 0 \\ 0 & 0 & c \\ 0 & c & 0 \end{pmatrix} \quad , \quad A_1(z) = \begin{pmatrix} a & 0 & 0 \\ 0 & a & 0 \\ 0 & 0 & b \end{pmatrix}$$

$$E_2^{(1)}(x) = \begin{pmatrix} e & 0 & 0 \\ 0 & -e & 0 \\ 0 & 0 & 0 \end{pmatrix}, \quad E_2^{(2)}(x) = \begin{pmatrix} 0 & e & 0 \\ e & 0 & 0 \\ 0 & 0 & 0 \end{pmatrix} \tag{2.19}$$

The application of the selection rules for the ZB and WZ structure will be illustrated in chapter 4, where these tensors will be used to calculate the scattering selection rules.

Chapter III

3. Experimental and Fabrication

In the following we will describe the experimental techniques of the Raman measurements and devices presented in this thesis.

3.1 Raman set-up

Two different Raman setups were used for measurements. One was in the lab of Prof. Tom Vosch[§], Copenhagen University and the second one was in the lab of Prof. Anna Fontcuberta I Morral[**], EPFL. The first setup is home built for back-scattering μ-Raman by Prof. Tom Vosch, and was used to perform measurements on single NWs. Samples were mounted upside down on a piezo-scanning stage (Physic Instrument P5173CL) of an inverted confocal microscope (Olympus IX71) with a 100x, 1.3 NA oil immersion objective that focuses the laser beam into a diffraction limited spot of a diameter of ~250 nm at $\lambda_{laser} = 514.5\,nm$. An Argon ion laser (CVI Melles-Griot 35MAP431-200) was used for excitation at 514.5 nm. The scattered light was collected through two types of detectors: Princeton Instruments EPEC-10:100B/LN_eXcelon CCD camera with 1-030-500 grating 1200 g/mm @ 500 nm or a High quantum yield Avalanche Photo Detector (APD) which construct an image of the recorded photon number transmitted through a band pass filter positioned in front of the APD. Polarization dependent measurements were enabled by a

---

[§] Tom Vosch Group, Nano-Science Center Department of chemistry, University of Copenhagen.

[**] Anna Fontcuberta I Morral, Laboratoire des Matériaux Semiconducteurs, Institut des Matériaux, Ecole Polytechnique Fédérale de Lausanne

motorized λ/2 plate which was mounted in the laser path before the microscope, controlling the polarization angle of the incident light. The polarization of the scattered light was filtered by a linear polarizer in front of the spectrometer. A schematic of the setup is presented in Figure 3.1.

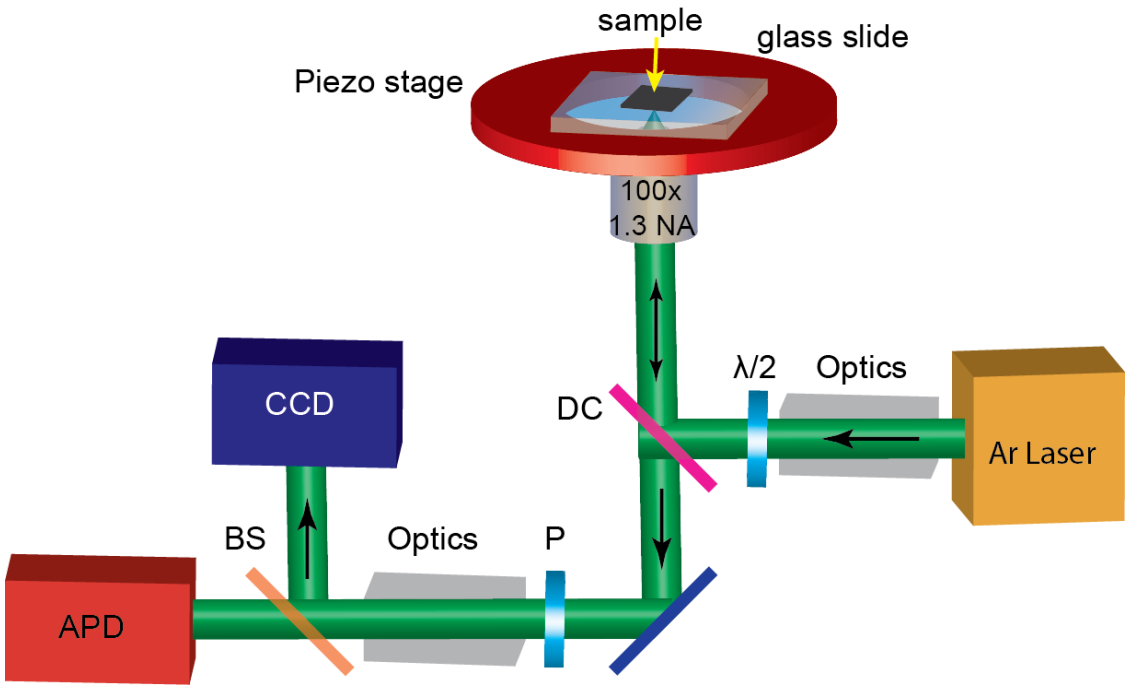

Figure 3.1 *Schematic illustration of the Raman setup.*

The second setup used is similar to the previous one except of the following points:

- Dry objective instead of the oil objective with 0.7 NA and focus the laser beam (at 520.8 nm) into ~1 μm spot.
- The objective is attached to the piezo scanner instead of the sample
- The sample is mounted facing upward on a manually adjusted stage
- Forward scattering experiments are possible
- A cryostat is implemented in the setup which enables measurements at vacuum and at low temperatures (@ 9 K) combined with electronic transport measurements
- This set-up does not include an APD detector

3.2 Home built electronic setup for Raman microscope

In order to perform electronic transport and Raman measurements simultaneously an electronic transport set-up was built on top of the Raman microscope stage as illustrated in Figure 3.2. A sample holder with connectors on the sides was attached and fixed to the microscope stage. This holder enables placing the wired socket, with a chip carrier plugged in, on top of the piezo stage. The chip with contacted wires was bonded to the chip carrier from the side of the chip so the bonding wires would not touch the glass slide (to prevent breaking of bonding wires and tilt of the chip).

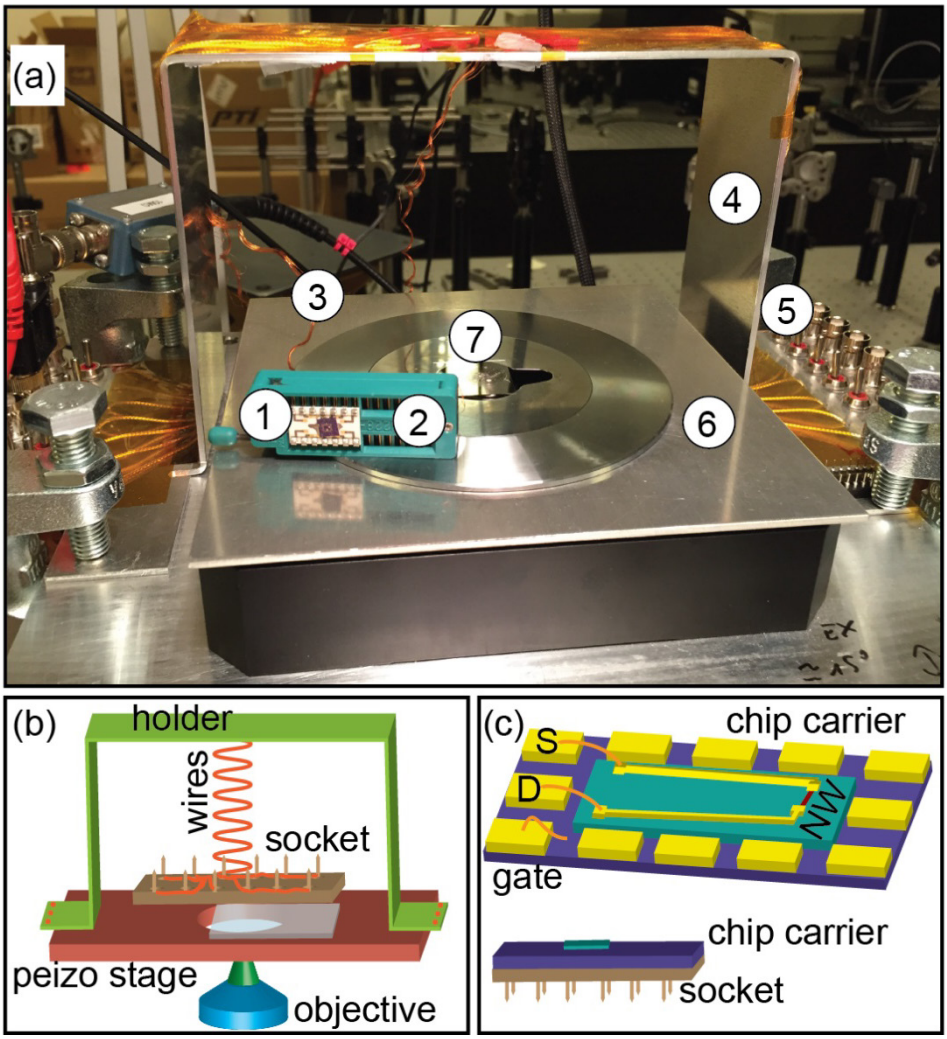

Figure 3.2 *(a) Photo of the transport setup. Numbers indicates the following: 1. Chip carrier. 2. Socket. 3. Connecting wires. 4. Holder. 5. Connectors. 6. Piezo stage. 7. Glass slide on top of the oil objective. (b) Schematic illustration of the*

set-up shown in (a). (c) Sketch of the socket and the chip carrier illustrating the FET contact geometry.

The NW was contacted in a field effect transistor (FET) geometry, as illustrated in Figure 3.2(c). The NW is contacted to a source and drain electrode, and a back-gate voltage was applied to the substrate to control the carrier density in the NW.

3.3 Substrates for Raman and TEM

A variety of substrates was used. For the Raman measurements a silicon wafer with 500 nm of silicon oxide on top was used. The identification of individual NWs was enabled by patterning the chips with numbered golden marks by e-beam lithography. Raman and TEM measurements were performed on the same NWs by using a commercial silicon TEM grid[35] with 50 nm thick Si_3N_4 membrane on top, as illustrated in Figure 3.3. These substrates are TEM compatible and they were used for detailed investigation of the structure of the measured NW and the potential modifications caused by the Raman laser. Nanowires were ultrasonically suspended from their growth chip in isopropanol, and then deposited on the substrate. Before measurements, the NWs were located by optical microscopy.

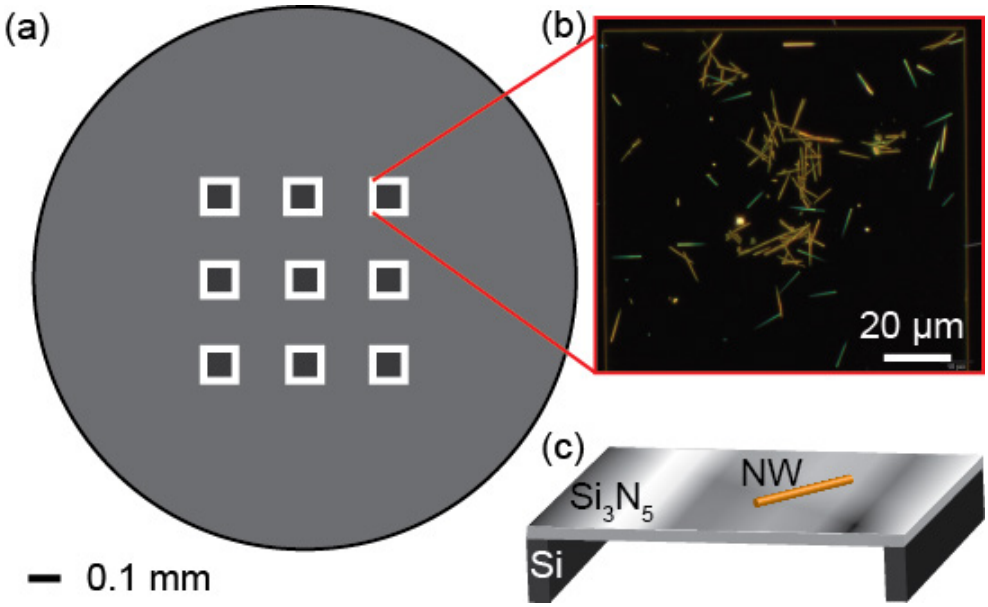

Figure 3.3 *(a) A sketch of the TEM grid. (b) Dark field optical image of the membrane with NWs on. (c) A sketch of the NW deposited on a Si_3N_5 membrane, supported by a solid silicon structure.*

3.4 Suspended NWs Devices

In order to study suspended NWs, we fabricated a special substrate. Silicon wafers were patterned with trenches etched through the silicon oxide layer. The trenches were 150 nm deep and 25 µm long with a width of several µm. Fabrication of trenches with sharp edges and smooth surfaces required the development of a process involving several steps of E-beam lithography:

1) a gold alignment grid was patterned
2) trenches were exposed in the E-beam resist and developed
3) trenches were etched into the silicon oxide, first, by a step of aligned Kaufmann argon ion milling at 45 ℃. Second, after the removal of the resist, a shallow angle milling step to remove the unwanted side walls of the trenches, which were deposited by the first milling step. This method produced precise dimensions and sharp edges of the trench, unlike the conventional wet etching method, using a solution of buffered hydrofluoric acid (HF), where trenches get non-uniform side walls and extra width caused by the undercut etching process.
4) Nanowires were deposited and located by optical microscopy.

An example of a suspended NW is presented in Figure 3.4, where dry etching technique was used to prepare precise trench dimensions with sharp edges. Milled trenches were used for the Raman measurements on suspended NWs presented in this thesis.

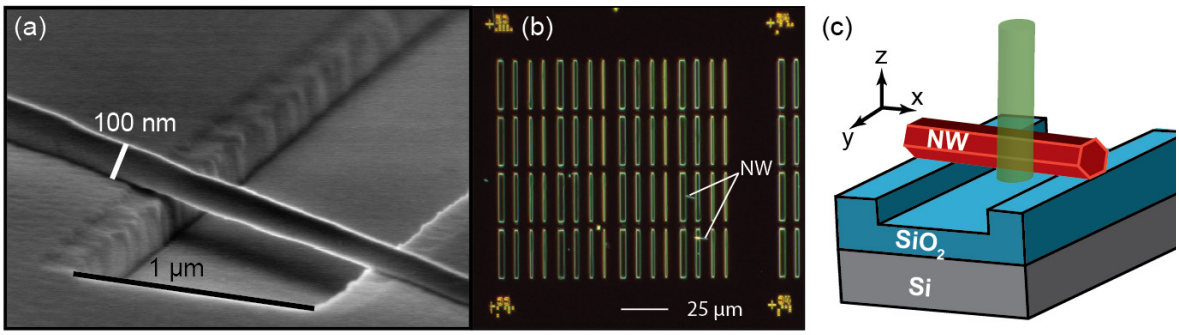

Figure 3.4 *(a) SEM image of an InAs NW suspended over a milled trench. (b) Optical dark field image of part of a chip with InAs NWs suspended over milled trenches. (c) Schematic of a measured suspended NW.*

3.5 Devices for combined Raman and electrical transport measurements

In later chapters we will present combined Raman and transport measurements on suspended InAs NWs. For this purpose devices were fabricated using e-beam lithography in the following order:

1) Au/Ti bonding pads and alignment marks were deposited on a silicon wafer with a 500 nm layer of silicon oxide. A special design for bonding pads was developed to maintain distance between the NWs and the bonding wires as shown in Figure 3.5(b). Thus, the part of the chip with the contacted NWs is mounted upside down on the glass slide on the Raman microscope objective, while bonding wires are beyond the edge of the glass slide (see Figure 3.2(b) and Figure 3.5(a)).
2) The chip is then patterned with trenches, as described in 3.4.
3) Nanowires were deposited and located with optical microscopy.
4) Au/Ti contacts to the chosen NWs were fabricated, see Figure 3.5(c) and (d). In order to get good Ohmic contact to the NWs, removal of the native oxide is required. This was achieved by using one of two methods, either sulfur passivation using Ammonium Polysulfide[36], or Kaufmann ion milling. Both methods were equally good. The average measured resistance of contacted 140

nm thick InAs NW at room temperature and zero gate voltage was around ~20 kΩ.

5) The chip was attached to a chip carrier (using silver paste) and bonded as shown in Figure 3.5(a).

The chip is then transferred to the Raman microscope and plugged in the socket where one can apply a source-drain bias and a backgate voltage and measure the current across the NW.

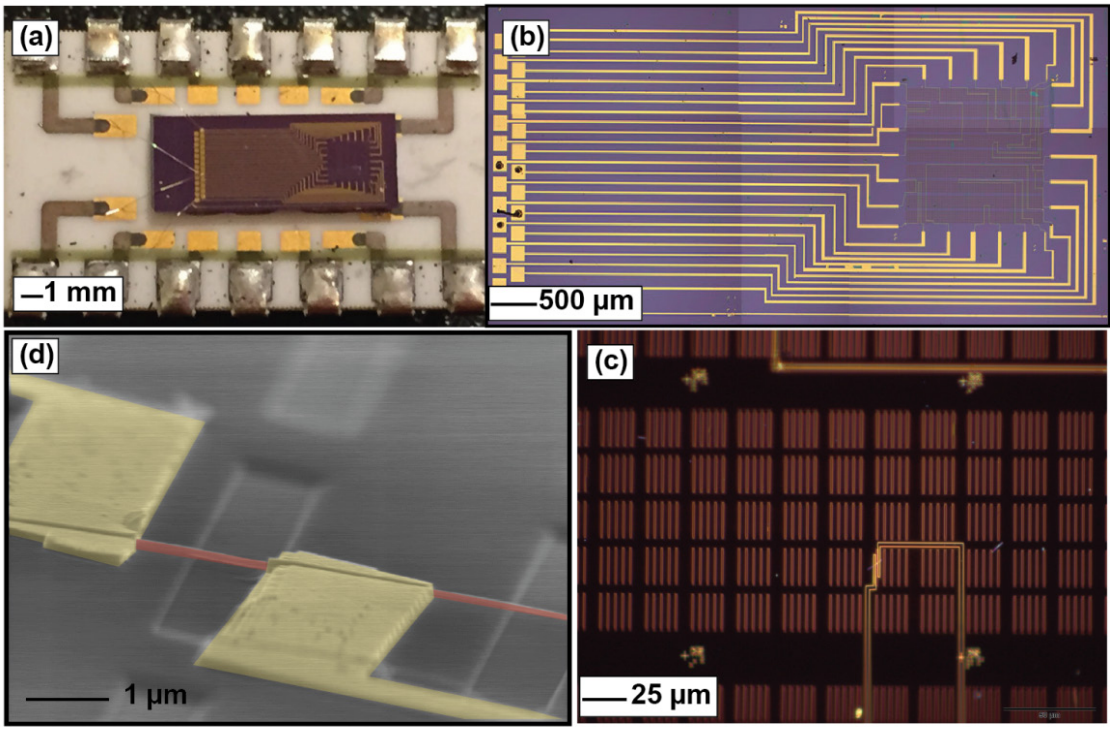

Figure 3.5 *Example of contacted NW for combination of Raman and TEM measurements, where sequence of zoomed images are presented. (a) Optical image of a chip carrier with bonded chip glowed to it. (b) Optical image of the chip. (c) Dark field optical image of the contacted NW. (d) SEM image of the contacted NW.*

Chapter IV

4. Determination of crystal orientation of InAs nanowires by Raman spectroscopy

As mentioned in chapter 2, the Raman scattering intensity of a Raman active phonon mode depends on the incident and scattered light polarization, which can be unique for different surface facets in a crystal. Thus, the angular dependence of the Raman intensity on the light polarization angle can be used to define the crystal orientation of the measured surface[37] ,or in the determination of the crystal direction of a NW. In this chapter we try to use the Raman selection rules to identify the crystal orientation of an InAs NW. This is relevant where Raman spectroscopy can be applied to NWs in devices in case it is important to define the crystal direction of the measured NW. An example of such a case is presented in Figure 4.1 where a kinked InAs NW is contacted by two gold contacts. In some cases, it is hard to distinguish one direction from another from the SEM images only, as shown in the inserts of Figure 4.1, where the two stems are distinguished by the gold droplet which position is not clear on which end of the NW. Another similar case is a catalyst free kinked InAs NWs.

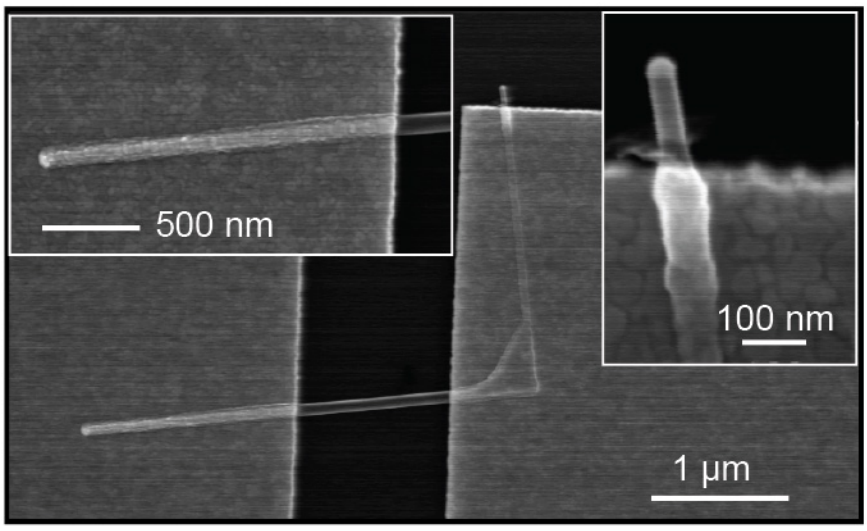

Figure 4.1 *SEM image of a contacted kinked InAs NW. Inserts are high magnification images of the two ends of the NW; illustrating the difficulty in identifying the end with the gold catalyst.*

In such cases it is useful to optimize a non-destructive optical method to identify the NW crystal direction, such as Raman spectroscopy. The applicability of this technique will be illustrated in the following chapter.

4.1 Selection rules of ZB InAs NWs

In the following section we will present the selection rules of the ZB and WZ structure for different possible growth directions and facets. First, we will present the selection rules calculation for the ZB structure. Let us consider the lab coordinate system according to the [111] or [0001] axes for ZB and WZ, respectively, as illustrated in Figure 4.2. We consider θ to be the angle between the incident light polarization e_i and the NW axis, assuming a light propagation direction along the x axis. We also introduce a rotation angle Φ, in the x-y plane around the z axis, in which the NW can rotate around its axis. The point of this rotation is to verify the difference in selection rules of different facet groups of the NW.

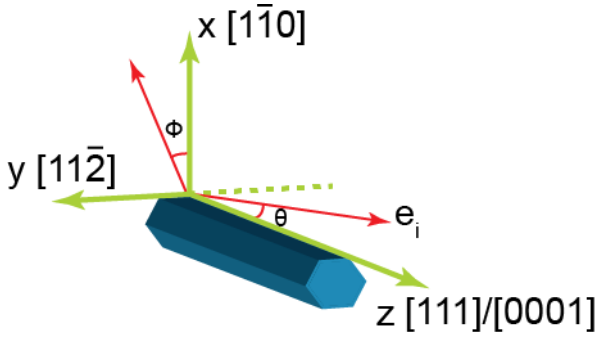

Figure 4.2 *sketch of the lab coordinate system according to the nanowire axis. θ is the angle between the incident light polarization and the nanowire axis. ϕ is the rotation angle around the z axis.*

The Raman tensors presented in equations (2.18) are for phonon vibrations along the principle axes of the crystal [100], [010], and [001] which form the $\{e_1, e_2, e_3\}$ basis. These tensors need to be transformed into the NW basis in order to calculate the selection rules of phonon displacements along the NW principle axes, which are $[1\bar{1}0] \parallel x, [11\bar{2}] \parallel y$ and $[111] \parallel z$ and form the $\{e_1', e_2', e_3'\}$ basis. First, we need to apply the following transformation matrix in order to get the Raman tensors assigned for atomic displacements along the NW axes.

$$M = \begin{pmatrix} \frac{1}{\sqrt{2}} & \frac{-1}{\sqrt{2}} & 0 \\ \frac{1}{\sqrt{6}} & \frac{1}{\sqrt{6}} & \frac{-2}{\sqrt{6}} \\ \frac{1}{\sqrt{3}} & \frac{1}{\sqrt{3}} & \frac{1}{\sqrt{3}} \end{pmatrix} \tag{4.1}$$

In the following we consider the facet with $[1\bar{1}0] \parallel x$ is the upper surface of the NW (as in Figure 4.2. The Raman tensors of displacements along x, y, and z in the $\{e_1, e_2, e_3\}$ basis can be obtained using

$$R'_{e_i} = \sum_{j=1}^{3} M_{ij} R_{e_j} \quad , i = 1,2,3 \tag{4.2}$$

The Raman tensors $R_{e_i'}$ in the new basis $\{e_1', e_2', e_3'\}$ then are be obtained by

$$R_{e_i'} = M R'_{e_i} M^T \tag{4.3}$$

Implementing the Raman tensors in (2.18) in (4.2) and (4.3) we get

$$R_{e_1'} = \begin{pmatrix} 0 & 0.82 & -0.58 \\ 0.82 & 0 & 0 \\ -0.58 & 0 & 0 \end{pmatrix}, \quad R_{e_2'} = \begin{pmatrix} 0.82 & 0 & 0 \\ 0 & -0.82 & -0.58 \\ 0 & -0.58 & 0 \end{pmatrix},$$

$$R_{e_3'} = \begin{pmatrix} -0.58 & 0 & 0 \\ 0 & -0.58 & 0 \\ 0 & 0 & 1.15 \end{pmatrix} \tag{4.4}$$

The optical modes are assigned to their tensors according to the phonon wavevector which is determined by the scattering geometry. For backscattering the phonon wavevector is along the light beam direction and in this case, is along $[1\bar{1}0] \parallel x$ in our lab coordinate system. This results into longitudinal vibration along the $[1\bar{1}0]$ direction which means that the LO mode selection rules are determined using $R_{e_1'}$ in the selection rules equation (2.17). The selection rules of the two TO modes (TO_y and TO_z) are the sum of the intensities obtained for each direction along y and z. The polarization vectors of the incident light e_i and the scattered light e_s are expressed according to the z axis (the NW axis) in Figure 4.2 as

$$e_i = \begin{pmatrix} 0 \\ sin\theta \\ cos\theta \end{pmatrix}, \qquad e_s^{\perp} = \begin{pmatrix} 0 \\ 1 \\ 0 \end{pmatrix}, \qquad e_s^{\parallel} = \begin{pmatrix} 0 \\ 0 \\ 1 \end{pmatrix} \tag{4.5}$$

where θ is the angle between the incident light polarization and the nanowire axis. In Figure 4.3(a) we present the calculated Raman polar intensity patterns, which shows the Intensity verses the incident light polarization angle for scattered polarization either parallel or perpendicular to the NW axis, of the TO mode. The calculated intensity matches the one measured of a bulk InAs wafer with the same crystal directions used as a reference. In this configuration the LO mode is not allowed for both parallel and perpendicular polarization and the bulk InAs spectra did not show any LO peak.

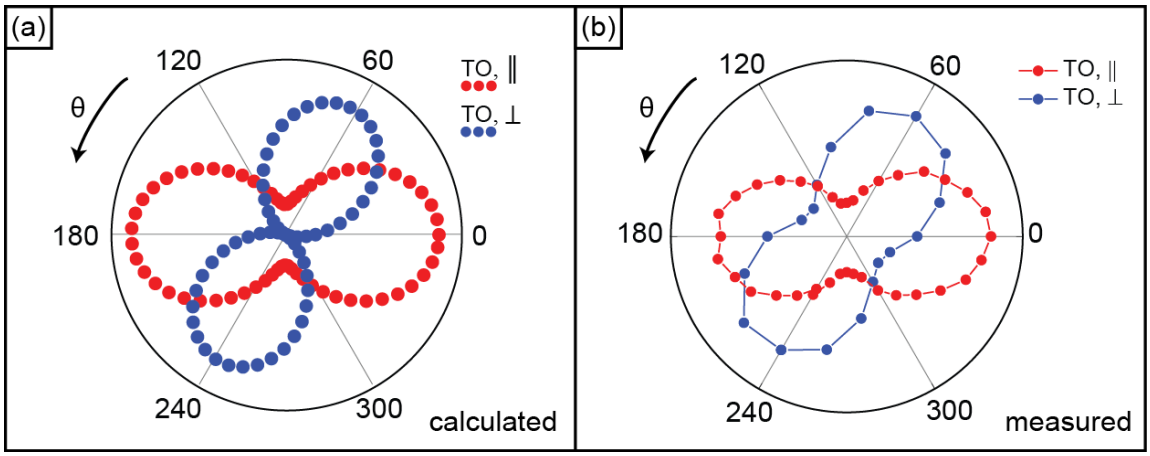

Figure 4.3 *(a) Raman intensity polar patterns as a function of incident polarization angle according to the [111] orientation of zinc-blende structure in back scattering geometry. Intensity is calculated for parallel and perpendicular polarization of the scattered light. (b) The measured Raman intensity of a reference bulk InAs with same conditions as (a).*

The previous calculations are valid for a surface facet that belongs to the $\{1\bar{1}0\}$ group. In order to examine the $\{11\bar{2}\}$ facet group we consider the upper surface of the NW to be a $[1\bar{1}0]$ facet. That can be achieved by rotating the NW around its axis by 90° and the rotation angle around the z axis will be denoted by ϕ. In order to consider this rotation in the Raman tensors a rotation matrix is multiplied by the transformation matrix M as:

$$T = S(\phi).M \tag{4.6}$$

where

$$S(\phi) = \begin{pmatrix} cos\phi & -sin\phi & 0 \\ sin\phi & cos\phi & 0 \\ 0 & 0 & 1 \end{pmatrix} \tag{4.7}$$

then T is considered in equations (4.2) and (4.3). This rotation will affect the LO mode selection rules as shown in Figure 4.4 which presents the polar intensity of the LO mode according to ϕ (the rotation angle around the NW axis). One can notice that for $\phi = 0$ which corresponds to the $[11\bar{2}]$ direction in the yz-plane, the LO mode is not allowed while for $\phi = 90$ ($[1\bar{1}0]$ direction is in the yz-plan) the LO mode is allowed for both scattered light polarization configurations (parallel and perpendicular). That could explain the

appearance of the LO mode in some cases when measuring ZB InAs NWs[21,28], where NWs may have different facets or a high density of stacking faults (which can be rotated atomic layers) is present in the NWs.

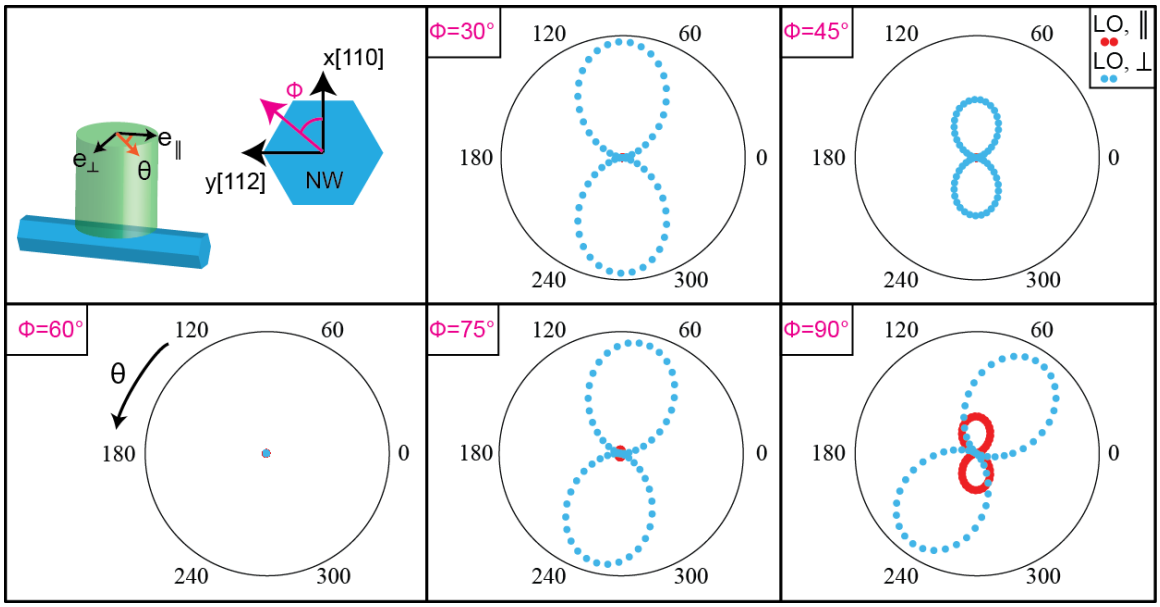

Figure 4.4 *Polar intensity of the LO mode as a function of* ϕ *for parallel and perpendicular polarization of the scattered light. The sketch illustrates the considered angles.*

The selection rules studied above can be violated due to several effects. For example, the observation of the forbidden LO mode could be explained by a resonance effect, where the laser wavelength matches an electronic transition in the electronic band structure as suggested in reference[10,1]. In other cases, the presence of stacking faults was assumed to induce the forbidden LO mode[38]. This is due to change in crystal orientation where the LO mode is allowed. This was observed in our Raman measurements performed on WZ InAs NWs (their selection rules will be presented later). A low intensity LO peak is present in a normalized line scan along the NW at few points of the NW as shown in Figure 4.5, where Raman spectra is recorded at parallel polarization configuration $x(z,z)\bar{x}$. This exemplifies that Raman spectroscopy can be used to estimate the variance in stacking faults position and density along the NW.

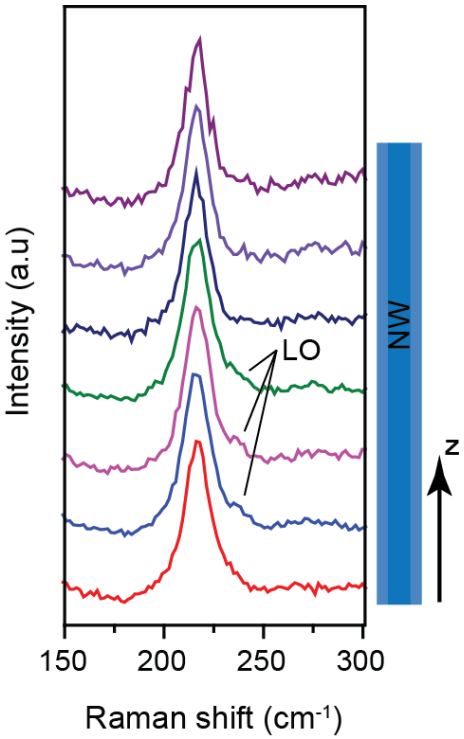

Figure 4.5 *A Raman line scan along the z axis of an InAs nanowire, on SiO_2 substrate, in parallel polarization configuration.*

The polar plots in Figure 4.3 are based on polarization angles according to the [111] crystal direction, a conventional growth direction for ZB InAs NWs. Another possible growth direction is the $[11\bar{2}]$ crystal orientation. Thus, we re-calculate the Raman polar plots according to the $[11\bar{2}]$ direction to show if Raman polar plots are useful to directly verify the crystal orientation of a random NW. This is done by re-calculating the polar plot as a function of polarization angle according to the $[11\bar{2}]$ instead of the [111] axis. This angle is defined as $\alpha = \frac{\pi}{2} - \theta$. The calculated polar plots of the TO mode according to α are presented in Figure 4.6(a), and they are consistent with the measured data of a bulk InAs according to α.

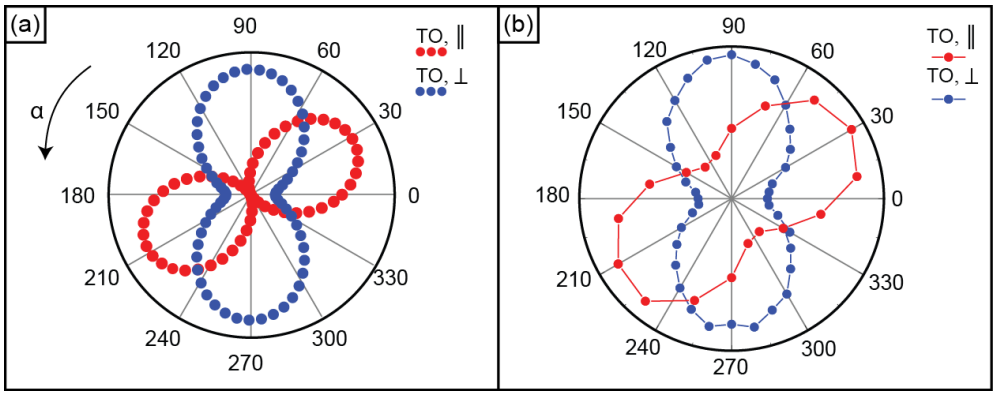

Figure 4.6 *(a) Raman intensity polar patterns as a function of incident polarization angle according to the* **[11$\bar{2}$]** *orientation of the ZB structure in back scattering geometry. Intensity is calculated for parallel and perpendicular polarization of the scattered light. (b) The measured Raman intensity of a reference bulk InAs with same conditions as (a).*

Comparing Figure 4.3 to Figure 4.6 will show a 30° shift in the maximum values for both parallel and perpendicular polarization. This can be used to identify the crystal orientation other than the **[111]** conventional direction, such as kinked InAs NWs with two **[111]** and **[11$\bar{2}$]** perpendicular stems (kinked nanowires grown in-house by Peter Krogstrup[††] have a WZ structure and will be discussed later). Another possible growth orientation in the ZB structure is **[001]**. An SEM image of **[001]** NW grown by Peter Krogstrup is shown in Figure 4.7(a). This type also has its unique polar Raman plots shown in Figure 4.7(b). The polar plots in (b) and (c) are identical but the difference is that only the TO mode is allowed when the **[100]** axis is in-plane, and only the LO mode is allowed when the **[010]** axis is in-plane. However, regardless of the in-plane axis the polar plots are still different from the cases of **[111]** or **[11$\bar{2}$]** crystal directions.

[††] Center for Quantum Devices, Niels Bohr Institute, Copenhagen University.

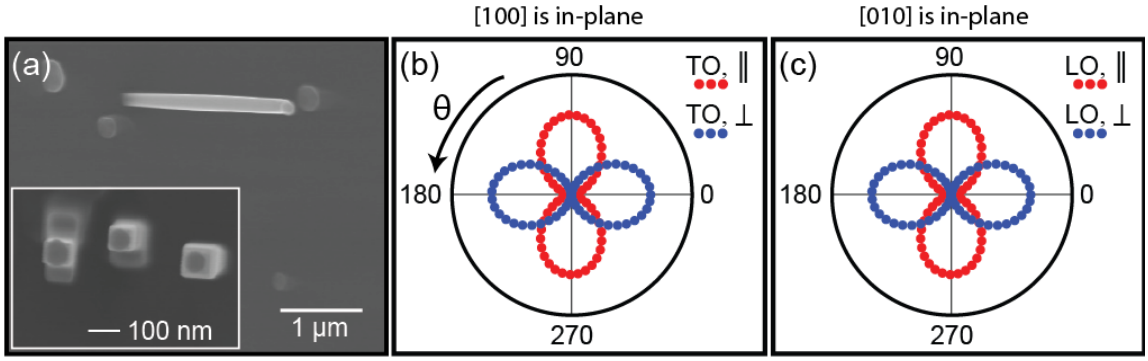

Figure 4.7 *(a) Tilt SEM image of an [001] InAs NW. Insert is a top view of the nanowire. (b) Raman polar intensity as a function of incident polarization angle according to the [001] crystal orientation, with [100] direction in-plan.*

The polar plots in Figure 4.7(b) show a 90° shift for the parallel scattering and 120° shift for the perpendicular scattering, compared to the TO mode for the [111] orientation. On the other hand, by comparing the LO mode polar plots to the ones in Figure 4.4 for $\phi = 90°$ one can notice that for parallel scattering there is no shift while for perpendicular scattering, there is shift of ~ -60°. The other plots where the LO mode is allowed (for $\phi = 30°, 45°$ and $75°$) there is a shift around 90°. This indicates the validity of polar Raman intensity maps to distinguish ZB NW with different growth axes.

4.2 Selection rules of WZ InAs NWs

For the WZ structure, which is the structure of our measured NWs, the transformation of the Raman tensors is not required, since the NW coordinate system matches the one of the primitive cell. As mentioned earlier, the Raman active vibrational modes are the two polar modes $A_1(TO, LO)$ and $E_1(TO, LO)$ (instead of one triply degenerate mode in the ZB case). They require the following method in order to assign and calculate the selection rules of the TO and LO modes based on the phonon wave vector dependent on the scattering geometry. We keep in mind that the A_1 mode only vibrates along the z or c-axis, while the E_1 mode vibrates in the x-y plane. Thus, in a backscattering geometry of [0001] nanowire along the z axis as depicted in Figure 4.2, the scattered phonon wave vector is parallel to $[11\bar{2}0] \parallel x$ resulting in an LO mode in the same direction and two TO modes in the perpendicular directions. In other words the $E_1(x)$ matrix from equations (2.19) will be assigned to the LO mode resulting in a forbidden LO in this configuration. The matrices of

$E_1(y)$ and $A_1(z)$ will be assigned to the two TO modes. The calculated $A_1(TO)$ and $E_1(TO)$ polar intensity is shown in Figure 4.8(a) and (b), respectively, for parallel and perpendicular scattering. Another interesting case is when the x-y plane is rotated by 90° around the z axis which transforms the $[11\bar{2}0]$ axis into the plane of measurement. In this case the allowed E_1 mode will be the longitudinal one instead of the transverse mode following the same intensity polar plots as listed in Figure 4.8(d). The non-polar E_2^{high} mode is only allowed for perpendicular scattering as shown in Figure 4.8(c).

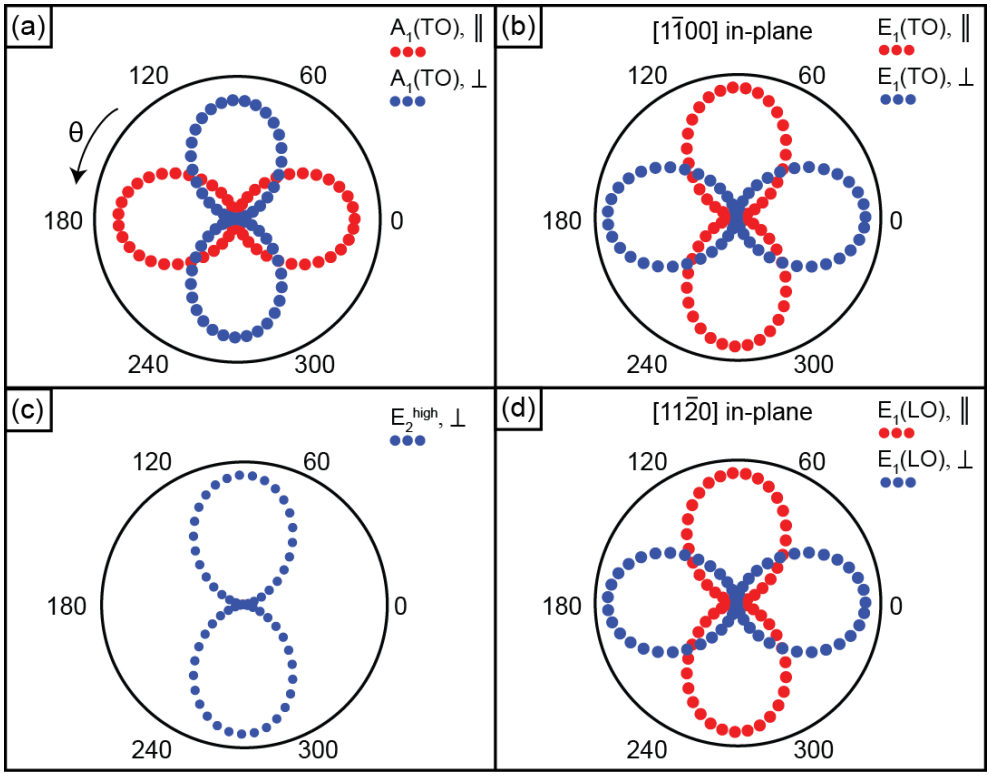

Figure 4.8 *polar plots of the WZ structure, for parallel and perpendicular scattering, of the following modes. (a) The $A_1(TO)$ mode. (b) The $E_1(TO)$ mode when the $[1\bar{1}00]$ axis is in-plan. (d) The $E_1(LO)$ mode in the case of $[11\bar{2}0]$ axis is in-plan. (c) The E_2^{high} mode (only perpendicular scattering since it's not allowed for parallel scattering).*

Similar to the ZB case, the Raman intensity polar plots can be recalculated for polarization angles according to the $[1\bar{1}00]$ axis instead of the $[0001]$ axis. This can be done by using the angle $\alpha = \frac{\pi}{2} - \theta$ in the Raman intensity equation (2.17). In this case no shift occurred in the polar plots, compared to Figure 4.8(a) and (b), which means that the $[1\bar{1}00]$ direction

cannot be distinguished from the [0001] by using Raman polar intensity plots. Figure 4.9 presents polarized Raman line scans recorded of two perpendicular branches of a kinked InAs NW as sketched in (e). No clear change is realized between the two stems. The LO mode appears for both segments and it is more pronounced for the $z(yy)\bar{z}$ polarization configuration. As mentioned earlier this is mostly due to high density of stacking faults in the NW.

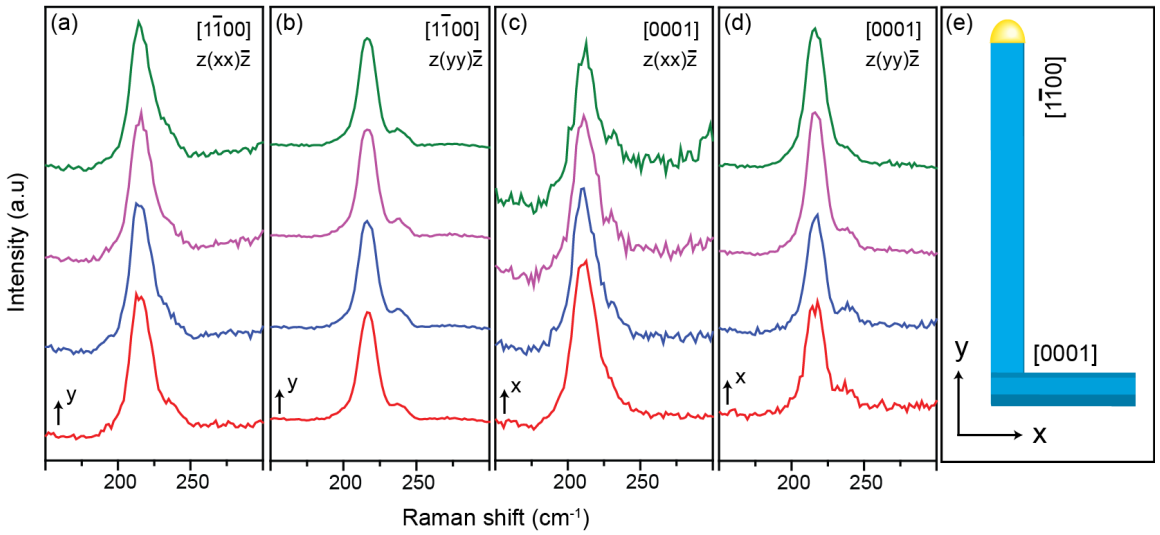

Figure 4.9 *Polarized Raman line scans of two perpendicular segments of a kinked NW as illustrated in (e). (a) and (c) are from the* [1$\bar{1}$00] *stem. (b) and (d) are from the* [0001] *segment. Polarization and scan direction are indicated on each graph based on the coordinate system in the insert.*

Unfortunately, no polar maps were recorded for the two segments of the nanowire, besides the high density of the stacking faults which will add an extra effect on the Raman spectra (violation of selection rules). This is one of the possible future measurements, where maps of stacking fault free kinked nanowires and the [001] oriented InAs nanowires, are to be measured. In conclusion, Raman intensity polar maps are a relatively easy approach to find the crystal orientation of InAs NWs with the ZB crystal structure, unlike the case of the WZ structure.

Chapter V

5. Surface-dependent oxidation of InAs nanowires

In this chapter we present a detailed study of laser induced oxidation of InAs nanowires. First, we induce the oxidation process by the Raman laser and record the polarized Raman spectra of the formed oxides. The very same nanowires are then imaged using transmission electron microscopy (TEM) and analysed. This effect is also studied on branched InAs nanowires where a direct measure of the surface-dependent oxidation effect can be realized.

5.1 Introduction

The development of NW based devices has generated the need for new fabrication techniques and characterization tools at the nanoscale. Transmission electron microscopy (TEM) has an important role as it provides atomic scale information about crystal structure, defects and chemical composition on the single NW level[39]. However, for the characterization of actual devices, the use of TEM is limited due to requirements of using electron transparent substrates[40]. On the other hand, scanning electron microscopy (SEM), atomic force microscopy (AFM) and optical techniques have been widely employed on a device level[41,42]. A convenient choice of a method is micro-Raman spectroscopy[26,27,29,32], which has proven to be a powerful non-invasive technique conveying information about the elemental composition[43,44], crystal properties[45] and defects[38] as well as free carrier densities and mobilities[46]. Also, at high intensities, the focused laser beam of a micro-Raman setup has been shown to enable controlled local cutting or chemical modification of InAs and GaAs NWs by local oxidation and formation of crystalline arsenic[34,47–49] and has been shown to enable welding of metal NWs[50]. This opens the possibility for using focused laser beams for engineering new functionality into NW devices as well as the conventional probing of the

NW. So far, laser modified semiconductor NWs have been characterized through their Raman spectrum and by AFM, SEM and photoluminescence, however, detailed morphologies have not been studied due to the substrate incompatibilities of TEM mentioned above. Here we show that 50 nm thick silicon nitride membranes can be used as an optimal substrate for correlating micro-Raman spectroscopy and TEM imaging. In the following, we will use this platform for analysing the change in NW morphology due to laser-induced chemical modification of InAs NWs. First, we will present the polarized Raman spectroscopy from the oxidized InAs NWs and find a strong enhancement of the Raman signal attributed to arsenic for parallel polarization in analogy to the antenna effect of pristine NWs[51]. Second, by applying the laser irradiation to branched InAs NWs, we show that the ability to locally induce modifications by laser irradiation depends strongly on the crystal orientation of the facets. This was verified by TEM inspection by T. Kanne[‡‡]. We try to explain this effect in terms of transition state kinetics of the free surfaces of the different crystal families of the facets based on the calculations of P. Krogstrup[§§]. Optical and thermal simulations were also performed by F. Amaduzzi[***] and M.H. Madsen[†††].

5.2 Experiments and results

In the following we will present Raman measurements of InAs based NWs, at high power regime, deposited on a 50 nm thick Si_3N_4 membrane. The insert in Figure 5.1 presents an illustrative sketch of the measurement with definition of the considered coordinate system.

[‡‡] Center for Quantum Devices & Nano Science Center, Niels Bohr Institute, University of Copenhagen, Universitetsparken 5, Copenhagen, Denmark

[§§] Center for Quantum Devices & Nano Science Center, Niels Bohr Institute, University of Copenhagen, Universitetsparken 5, Copenhagen, Denmark

[***] Laboratory of Semiconductor Materials, Ecole Polytechnique Fédérale de Lausanne, 1015 Lausanne, Switzerland

[†††] *Danish Fundamental Metrology A/S, Matematiktorvet 307, DK-2800 Kgs. Lyngby, Denmark*

Figure 5.1 shows typical Raman spectra for a bulk InAs reference and the two cases of a non-oxidized InAs NW deposited on SiO_2/Si wafer and an oxidized InAs NW on a TEM membrane.

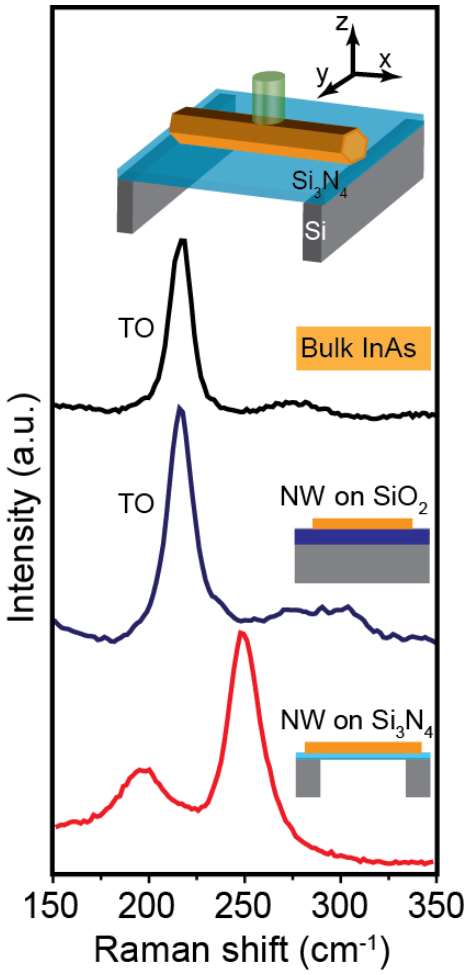

Figure 5.1 *Typical Raman spectra of bulk InAs (top curve), an InAs NW deposited on a SiO_2 surface (middle curve), and an oxidized InAs NW on a Si_3N_4 membrane (bottom curve). Spectra off-set for clarity. Insert is a schematic illustration of the setup and the definition of the coordinate system.*

The spectra of the bulk InAs and non-oxidized NW are almost identical and contain one main peak at ~216 cm^{-1} assigned to the InAs transverse optical (TO) phonon mode and a week side-peak at 237 cm^{-1} assigned to the longitudinal optical (LO) mode. According to the Raman selection rules of the WZ crystal structure only the TO mode is allowed in this polarization configuration[21], however, the LO mode may appear due to crystal stacking faults

in the NW[38]. As seen in the lowermost curve of Figure 5.1 the oxidized NW on the TEM grid shows a drastically different spectrum containing two high intensity peaks at 203 cm^{-1} and 250 cm^{-1} which do not match any phonon energies of the InAs structure.

Power dependent Raman spectra are presented in Figure 5.2 for excitation polarization parallel to the NW axis at laser wavelength of 520.8 nm. The anomalous peaks in the spectra are not observed at very low power, but irreversibly appear after applying illuminating powers above 120 kW/cm^2. In this measurement the NW was not suspended on a TEM grid but instead over a 1 μm wide trench etched in SiO_2. These results suggest laser induced modification of the crystal and the anomalous Raman spectra indeed matches that of crystalline arsenic[52], with the peaks assigned to the arsenic double degenerate E_g(TO) mode at 198 cm^{-1} and A_{1g}(LO) mode at 257 cm^{-1}

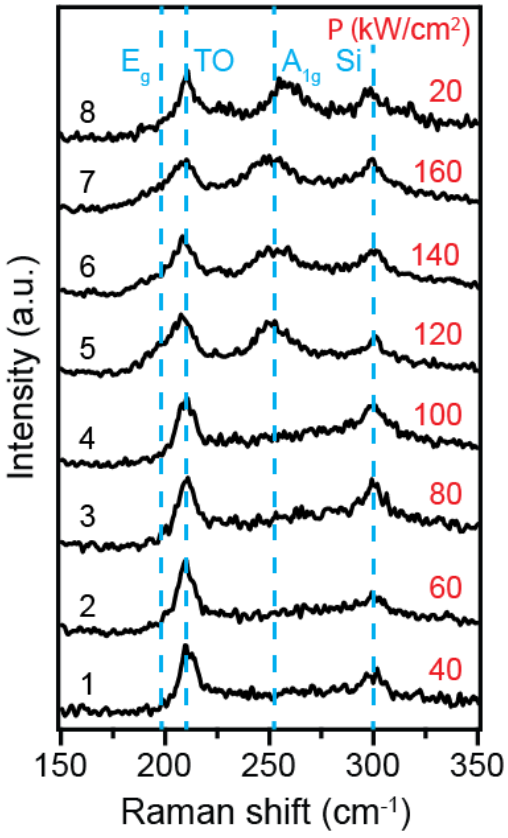

Figure 5.2 *Power dependent Raman spectra of suspended InAs NW at parallel excitation polarization. The power density of each spectra is indicated on the right. Leftmost numbers indicate the order in which the spectra were recorded.*

An observation of crystalline arsenic in a III-As semiconductor-oxide interface was reported in reference[53], where the two arsenic peaks were assigned to crystalline and not amorphous arsenic since they match the crystalline spectrum and exhibit a relatively high intensity Raman peak (~three order of magnitude higher than the InAs TO intensity), indicating a metallic nature of the formed layer. In bulk form, the thermal oxidation process on InAs surface will produce a mixture of the following compounds: As_2O_3, As_2O_5 and In_2O_3[54] according to the In-As-O ternary equilibrium phase diagram presented in Figure 5.3[55]. The detection of crystalline arsenic layer was also reported for thermally oxidized InAs surface[53,54,56]. This was explained by the proposal of three types of chemical reactions based on equilibrium phase diagram and thermodynamics of interfacial reactions:

$$3O_2 + 2InAs \rightarrow As_2O_3 + In_2O_3 \quad (1)$$

$$As_2O_3 + 2InAs \rightarrow In_2O_3 + 4As \quad (2)$$

or

$$4O_2 + 2InAs \rightarrow As_2O_5 + In_2O_3 \quad (3)$$

$$3As_2O_3 + 10InAs \rightarrow 5In_2O_3 + 16As \quad (4)$$

or

$$2O_2 + InAs \rightarrow InAsO_4 \quad (5)$$

$$3InAsO_4 + 5InAs \rightarrow 4In_2O_3 + 8As \quad (6)$$

According to Schwartz[55], in weak oxidation conditions reaction (2) has a higher possibility to happen, while reaction (1) and reaction (5) are possible for intermediate and strong oxidation conditions, respectively. Hollinger et al[54], found that, for thermally induced oxidation, reaction (5) is more likely to happen, since the authors could detect a single phase $InAsO_3$-like oxides and very little trace of arsenic. On the other hand, for optically oxidation of InAs surfaces a thinner oxide layer ~3 nm was produced and arsenic-rich phases were also detected. In this case it was proposed that the oxidation was dominated by photo-chemical effects.

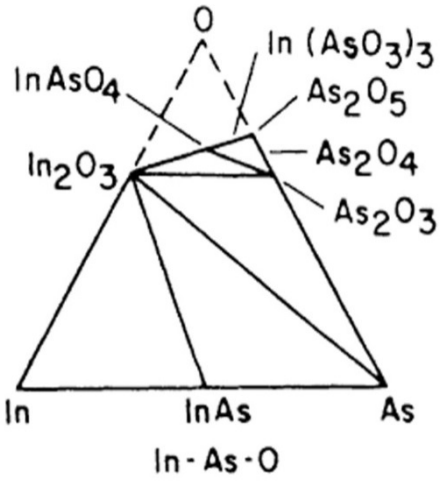

Figure 5.3 *In-As-O ternary condensed phase diagram. From reference*[55].

Crystalline arsenic was also detected by Farrow et al[53], when shining a high power laser beam on III-As surfaces (the same effect was also applied on III-Sb materials). Raman spectra of the treated sample were found to contain crystalline arsenic peaks. These peaks are polarization dependent according to crystalline arsenic selection rules indicating that arsenic was formed in a single crystalline phase. Therefore, we assign the anomalous spectra as the result of laser induced NW heating[57,53], possibly combined with photo-oxidation[54]. At these laser powers the oxidation is not significant for the NWs on the Si/SiO_2 substrates, probably due to more effective heat dissipation and resulting in lower temperatures of the NWs.

Figure 5.4(a) presents polarization dependent Raman spectra for a different nanowire on Si_3N_4 support, using a 514.5 nm laser with power density of 450 kW/cm^2. The spectrum with $z(xx)\bar{z}$ polarization configuration is identical to those in Figure 5.1 and Figure 5.2, and in addition to the InAs A_1(TO) mode at ~220 cm^{-1}, the two arsenic peaks are observed at ~203 cm^{-1} and ~255 cm^{-1} showing the laser induced arsenic formation. The arsenic peaks also appear for the $z(xy)\bar{z}$ configuration along with the E_1(TO) mode at 216 cm^{-1}, as expected from the WZ InAs NW selection rules[21]. Since the oxidation process takes place at the nanowire surface, the simultaneous appearance of the InAs and crystalline arsenic modes indicates that the crystalline semiconductor of the core remains intact.

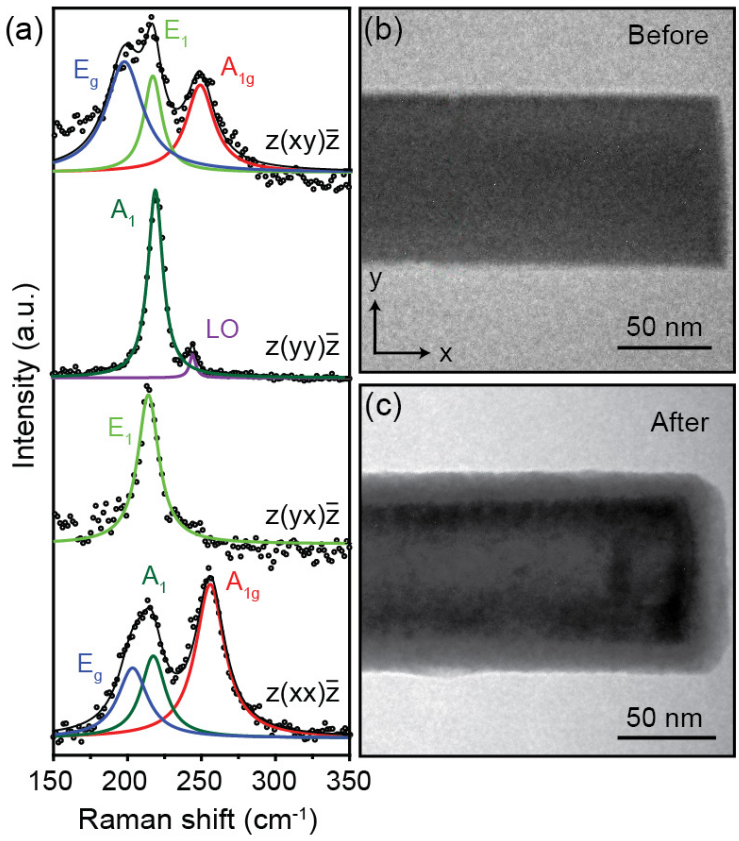

Figure 5.4 *(a) Polarization dependent Raman spectra of InAs nanowire on Si_3N_4 membrane. Spectra are fitted using a Lorentzian line shape and the InAs modes are observed at 220 cm^{-1} (A_1), at 216 cm^{-1} (E_1), and 243 cm^{-1}(LO), whereas the arsenic modes are E_g(TO) at ~200 cm^{-1} and the A_{1g}(LO) at ~253 cm^{-1}. (b), (c) TEM images of the measured nanowire bottom end, recorded before and after Raman measurements, respectively.*

Figure 5.4(b) and (c) show TEM images of the NW before and after the exposure to the laser. Initially, the NW has a uniform morphology containing only occasional stacking faults. After the laser irradiation the NW surface is more disordered and covered by a low contrast coating and decorated by 5-10 nm grains of higher contrast as seen in Figure 5.4(c).

We attribute the grains to either arsenic or polycrystalline In_2O_3 agglomerates (see below). The bulk of the NW appears unaffected, consistent with the persistence of the InAs TO modes. Interestingly, as observed in Figure 5.4(a), at polarization configuration $z(yy)\bar{z}$

and $z(yx)\bar{z}$, the InAs spectra, without any trace of the arsenic modes, are recovered when the excitation is polarized perpendicular to the NW axis. This peculiar polarization dependence has been observed on all 10 measured nanowires, but, the arsenic modes should not disappear for perpendicular polarized excitation according to arsenic selection rules[52], which has a trigonally distorted cubic structure with two atoms in the primitive cell. This structure has two phonon modes at the zone center, A_{1g}(LO) which is totally symmetric and the E_g(TO) mode which is doubly degenerate and their selection rules are determined by the following tensors:

$$A_{1g} = \begin{pmatrix} a & 0 & 0 \\ 0 & a & 0 \\ 0 & 0 & b \end{pmatrix}, E_g = \begin{pmatrix} c & 0 & 0 \\ 0 & -c & d \\ 0 & d & 0 \end{pmatrix}, E_g = \begin{pmatrix} 0 & -c & -d \\ -c & 0 & 0 \\ -d & 0 & 0 \end{pmatrix} \quad (5.1)$$

Thus, we attribute the polarization dependency to an antenna effect[51] of the nanowire geometry enhancing the arsenic signal when the excitation is polarized parallel to the NW axis. This effect can be directly observed by measuring Raman photon counts, with an APD detector (described in section 3.1) from a kinked NW. Here, a high Raman intensity is observed when the excitation light polarization is parallel to the NW axis. Figure 5.5(a) and (b), which represent a spatial Raman map of a kinked NW positioned as illustrated in the insert, shows a relatively high Raman scattering cross section when the polarization is parallel to the NW segment axis.

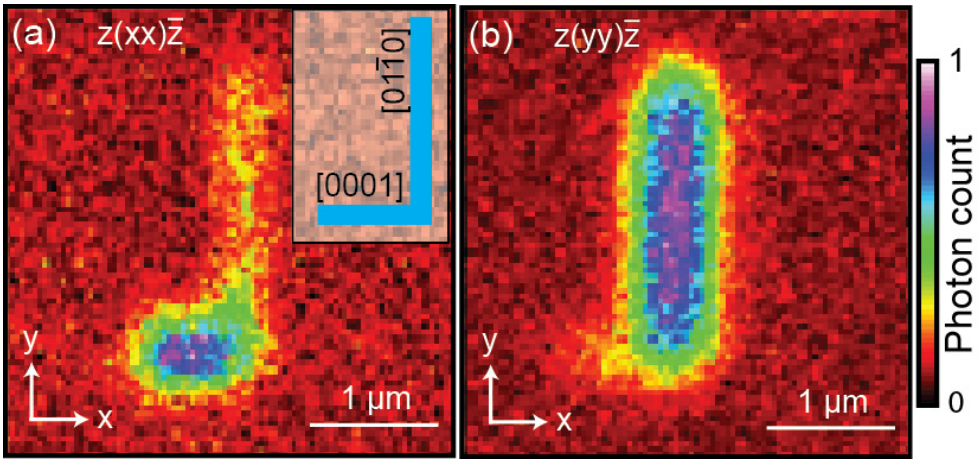

Figure 5.5 *(a) and (b) Raman image of a kinked InAs NW where Antenna effect is observed when the polarization is parallel to the wire axis. The insert in (a) is a sketch of the measured NW. The image is recorded by an Avalanche Photo Detector (APD).*

Since the oxidation reaction occurs at the surface of the NW, it is interesting to investigate the effect of laser induced heating on NWs with different surface facets. Figure 5.6 compares a NW grown in the conventional **[0001]** direction (having **{01$\bar{1}$0}** surface facets) to a NW grown in the perpendicular **[01$\bar{1}$0]** direction (having **{0001}/{11$\bar{2}$0}** surface facets). A schematic of the branched NW geometry is presented in Figure 5.6(a) and a typical structure is shown in the TEM image in Figure 5.6(c) prior to the laser exposure. The **[0001]** stem and **[01$\bar{1}$0]** branch are identified by the morphology of the structure and the position of the gold catalyst particle at the end of the branch.

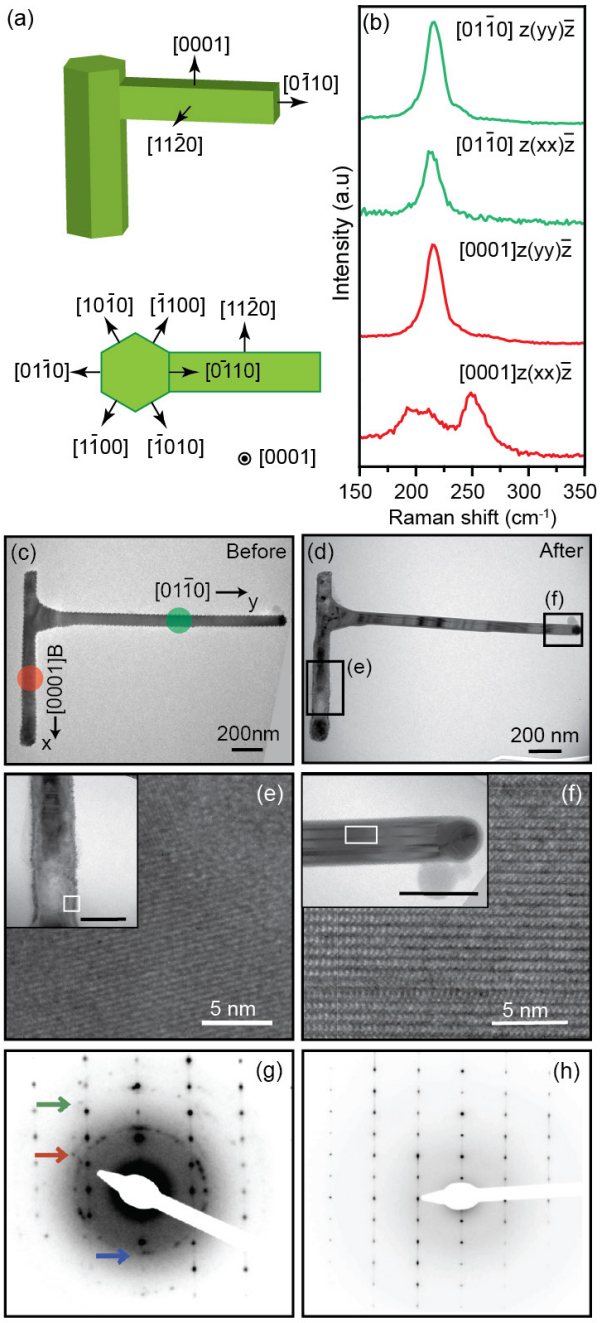

Figure 5.6 *(a) A schematic illustrating the geometry of the branched nanowire. (b) Raman spectra at the two stems of kinked InAs nanowire with polarization indicated by Porto notations. (c) and (d) TEM images of the nanowire measured in (b) before and after measurement, respectively. (e) and (f) high resolution TEM images of the regions indicated in (d). The scale bar in the inserts is 100 nm. (g) and (h) are selected area diffraction (SAED) patterns of (e) and (f), respectively. The arrows in (g) points at the diffraction rings correspond to polycrystalline* In_2O_3.

Figure 5.6(b) shows Raman spectra measured at the stem and branch for both parallel and perpendicular polarizations as indicated on the figure using laser a power density of 450 kW/cm^2. As for the **[0001]** NW in Figure 5.4, the arsenic peaks are observed for the **[0001]**

stem and only for parallel polarization. Interestingly, however, these peaks are absent in the $[01\bar{1}0]$ branch for both polarization configurations. The difference between the two directions is further verified by TEM inspection: Figure 5.6(e) shows a clear surface modification on the $[0001]$ stem while Figure 5.6(f) shows that the $[01\bar{1}0]$ branch remains unaffected by the laser irradiation. Figure 5.6(g) and (h) present the corresponding diffraction patterns of the stem and branch, respectively. The patterns related to the wurtzite InAs structure are present in both cases, confirming that a significant part of the crystalline NW remains intact. In addition, distinct ring-shaped patterns appear at the $[0001]$ stem consistent with (222), (400) and (440) high intensity crystal planes of poly-crystalline In_2O_3 as expected from the proposed oxidation reaction. The crystalline arsenic appearing in the Raman spectra of the $[0001]$ stem does not appear in the corresponding diffraction patterns, which we attribute to arsenic with a well-defined crystal orientation not allowing the diffraction in this particular orientation. These results show that the oxidation process did not evolve on the $[01\bar{1}0]$ nanowire branch.

The oxidation process may consist of several parallel reaction schemes, where each scheme typically includes two sequential reactions[34,54]. To understand why the $[01\bar{1}0]$ InAs NW branch is more stable towards oxidation than the $[0001]$ stem we study the oxidation reaction kinetics of InAs surfaces in general terms, valid for all possible reactions including InAs. This means that instead of identifying a specific rate limiting reaction, we can consider the irreversible transition rates Γ^{ox} of a general oxidation reaction of InAs, which can be written as[58]:

$$\Gamma^{ox} \propto c_{oxide} c_{InAs} exp\left[-\frac{\sum_A \delta h^A - \sum_{A,B} \delta \mu_B^A}{k_B T}\right] \tag{5.2}$$

Here c_{InAs} and c_{oxide} are the interfacial concentrations, and $\delta h^A \approx U^A - \gamma_j^A$ is the activation energy which is the energy required to dissociate an atom at the interface j of phase A with respect to a reference state. U^A is the bulk cohesive energy, γ_j^A is the interface energy excess per surface atom contributing with dangling bonds and represents a relative measure of the surface stability. $\delta\mu_B^A$ is the relative chemical potential (i.e. the thermodynamic driving force for the reaction) of element B (As, O or In) in phase A (such as: As_2O_3, InAs, In_2O_3, $InAsO_4$) relative to the reference state and is defined as:

$$\delta\mu_B^A = \delta\mu_B^{A,bulk} + \gamma_j \frac{\partial A_j}{\partial n_B} + A_j \frac{\partial \gamma_j}{\partial n_B} \tag{5.3}$$

where the first term relates to the bulk free energy (which we are not interested in here because it is the same for both types of wires) and the other two terms relate to the excess free energy associated with the interfaces. A_j is the area of the interface j, and n_B is the number of atoms B in the phase A. Because the oxides are polycrystalline with a dominant crystal direction, and because the reaction schemes are the same on the kink and on the stem, the only difference in the exponential of equation (5.2) is either γ_j^{InAs} (in the activation energy δh^A) or the size dependent part of the chemical potentials $\gamma_j^{InAs}\frac{\partial A_j}{\partial n_B}$ which is negligible due to the scale of the NWs. The third term in equation (5.3) is also negligible assuming the same response to change in surface energy at the two directions. This means the difference seen in the oxidation rates is solely a kinetic effect (δh^A) rather than driven by thermodynamic driving forces ($\delta\mu_B^A$). At thermal equilibrium, the differences in transition rates of the two types of facets are caused by differences in surface stabilities, with a reaction rate ratio given by $\Gamma_{01\bar{1}0}^{ox}/\Gamma_{11\bar{2}0}^{ox} \propto exp\left[\frac{\gamma_{01\bar{1}0}^{InAs}-\gamma_{11\bar{2}0}^{InAs}}{K_BT}\right]$ using equation (5.2). However, implementing reported values for surface energies in the literature[59], which is a measure of γ_j^A, do not show any significant differences between the stability of $\{01\bar{1}0\}$ facets of the stem and the $\{11\bar{2}0\}$ facets of the kink. Another mechanism could be the differences in surface roughness, which affect γ, due to the presence of Ga at the stem surface due to kinking procedure[60], could lead to the observed effect.

Alternatively, thermal gradients due to differences either in absorption efficiency or in thermal conductivity or dissipation to the substrate could play a role. To compare the effect of kinetic barriers with possible differences in temperature, we simulated the distribution of the electromagnetic radiation and light absorption. The calculations were realized for the two cross-section geometries and the corresponding diameter. The electromagnetic simulations were performed with the finite-difference time-domain package MEEP[61]. For the incident light, we considered a plane wave polarized along the nanowire axis. For the absorption efficiency, we have calculated the flux inside a box around the NW given by a top plane wave incoming onto it[62]. To normalize this value, we performed a reference simulation without the NW. From this simulation, we calculated the flux through the projected area of the NW on the bottom face of the box. The resulting values of the absorption efficiency for the parallel polarized light are 165 % and 157 % for the branch and the stem, respectively.

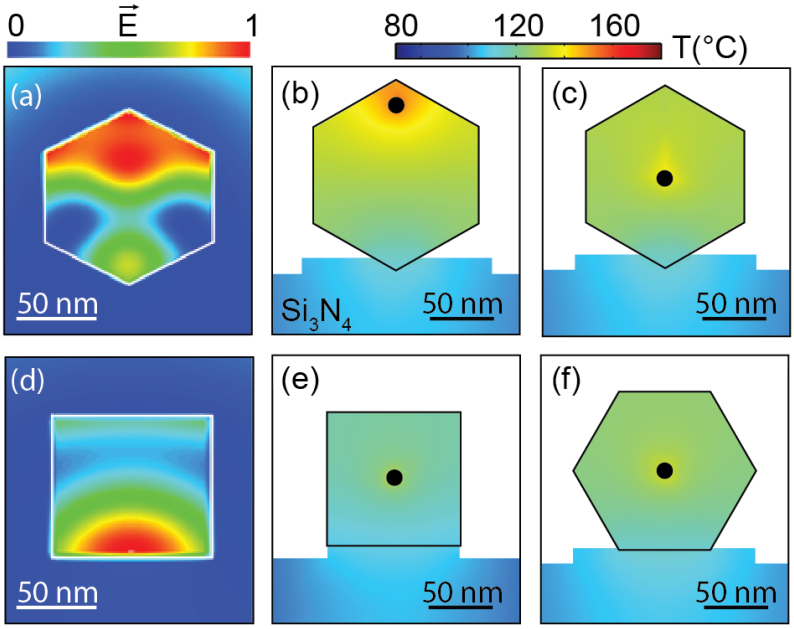

Figure 5.7 *(a) and (d) Cross-sectional maps of the normalized field energy distribution for the* [0001] *stem and the* [01$\bar{1}$0] *kink, respectively. (b), (c), (e) and (f) are temperature profiles of the stem and the kink for different position of the heat source. The black circle indicates the heat source position.*

Thus, there is not a significant difference in the absorption efficiency. However, the simulated internal field distribution in Figure 5.7(a) and (d) shows that the intensity is localized in different areas of the two cross-sections. In the case of the stem, the intensity is more intense at the top facets of the nanowire, which may lead to a poorer heat dissipation through the substrate as compared to the kink, where the higher absorption is at the bottom face with a larger contact area with the substrate. The good thermal contact of the facet with the substrate should improve the thermal dissipation limiting the oxidation process on the kink. Additionally, the temperature profile of the stem and the kink on a 50 nm thick Si_3N_5 substrate was simulated using COMSOL Multiphysics. Full 3D models of the two systems were built and the heat equations were numerically solved with finite element analysis. Figure 5.7(c) presents the temperature profile of the stem considering the heat source at the top of the NW cross-section, here there is a temperature difference of ~60 °C between the top and the bottom part of the NW, which could have a considerable impact on the reaction rate since it's exponentially related to temperature. However, moving the heat

source to the center will decrease the temperature by ~20 °C as shown in Figure 5.7(c), this is attributed to more efficient heat passivation though the substrate. Indeed, for the kink and the stem, with facets in planar contact to the substrate, the temperature decreases to 120 ℃ for the kink (Figure 5.7(e)) and 130 ℃ for the stem (Figure 5.7(f)) with equal temperature distribution around the heat source. This may explain the non-oxidation of the kink, but on the other hand we found that a conventional NW positioned as in Figure 5.7(f) did actually oxidized. The small bump in the Si_3N_5 substrate in Figure 5.7(c), (d), (e) and (f) is an isolation layer with the same properties as the substrate, which determines the contact area between the NW surface and the substrate, decreasing this area by a factor of 10 will increase the temperature of the NW by 80 °C. Finally, a combination of the effects mentioned earlier could cause the observed selective oxidation of the branched InAs NWs, but further experiments are needed to shed more light on these aspects.

5.3 Conclusions

In conclusion, we have studied the surface oxidation process of InAs nanowires by combining polarized micro-Raman spectroscopy and transmission electron microscopy on individual InAs nanowires, having been irradiated by a high power laser to promote oxidation. The Raman spectra of the irradiated NWs are consistent with an induced oxidation reaction leaving crystalline arsenic on the wire-oxide interface. This is consistent with TEM analysis showing a significant roughness of the surface and nanoscale agglomerates, presumably of crystalline arsenic or polycrystalline In_2O_3. The presence of polycrystalline In_2O_3 was confirmed by TEM diffraction. We measured the polarization dependence of the Raman spectra, which surprisingly showed only the arsenic modes for incident polarization parallel to the NW axis. Furthermore, the TEM analysis confirmed that the oxidation process occurs at the nanowire surface and that the InAs crystal remained in the NW core. Thus, focus laser irradiation may provide a method for local effective thinning of nanowires in electrical devices thereby inducing local regions with modified properties such as higher band-gaps for electrical barriers or increased sensitivity to the immediate chemical environment. Finally, we studied the dependence of the laser induced modification on the crystal direction of the InAs nanowire. By combined Raman and TEM analysis we find that NWs grown along unconventional directions $\langle 01\bar{1}0 \rangle$ are more resistive to high power laser irradiation. This observation was discussed in terms of transition state kinetics of NW facets, surface

roughness, and finally in terms of light absorption efficiency of geometries of the NW. Our work shows that nanowire crystal structure is an important parameter for engineering robust nanowire devices.

Chapter VI

6. Local oxidation of InAs nanowires enabled by substrate micro-trenches and laser irradiation

The potential of semiconductor NWs, in devices, can be expanded by improving or implementing new functionalities, therefore, methods of locally controlling the properties along the NWs are often required. Such control has been demonstrated either by advanced device architectures incorporating local electrostatic gates[63] or by modifying the crystal properties along the wire by changing material composition during or after growth[18,64–66]. As discussed in 5, an alternative approach which has recently emerged is the possibility of using a high intensity focused laser beam to locally induce chemical changes in the NW[47]. By combination of Raman spectroscopy[34,49] and transmission electron microscopy[67], we have shown that the irradiated parts of InAs NWs with high power laser promotes the oxidation process $As_2O_3+2InAs \rightarrow In_2O_3+4As$ which converts of the NW surface to crystalline arsenic and polycrystalline indium oxide. However, so far, only little is known about the properties of the resulting structures and the spatial resolution that can be achieved has not been analyzed. A similar process occurs for GaAs, and in Ref.[49] it was shown that the thermal conductivity of the NW is dramatically decreased upon irradiation, suggesting this method as a way of designing structures with enhanced thermoelectric properties.

Here we show that by suspending NWs over trenches etched into a SiO_2 substrate the temperature profile of the NW can be locally engineered. By tuning the laser intensity, only the suspended parts of the NWs will reach a temperature sufficient to activate the oxidation process. By means of Raman spectroscopy we demonstrate the viability of this approach, achieving a spatial resolution of at least 250 nm; the size of the detection area of our Raman

setup. Temperature distribution of the suspended NW was simulated by M.H. Madsen[‡‡‡]. We further study the electrical properties of the oxidized NWs and show that they maintain their ability to carry electrical current and also preserve the key semiconductor property of electrostatic tunability using a nearby gate electrode. Finally, we discuss the effect of the nanowire carrier density on the profile of the Raman spectrum of the oxidized nanowire.

6.1 Experiments and results

6.1.1 Suspended NWs

The NWs used in this chapter are conventional InAs NW grown in the [0001] direction of the wurtzite crystal structure with a length of ~7 µm and a tapered profile having diameters of ~130 nm at the base and 40 nm at the tip[68]. Substrates of degenerately doped silicon with a 500 nm SiO2 capping were prepared with metal alignment grids and arrays of 150 nm deep and 1 µm wide trenches fabricated using electron beam lithography and shallow angle Kaufmann ion milling (see 3.4). The NWs were ultrasonically suspended in isopropanol and randomly dispersed on the substrates. NWs bridging the trenches were located by optical inspection. Raman measurements were performed using a 514.5 nm laser beam focused into a ~250 nm diameter spot on the sample. The polarization of both incident and scattered light was oriented parallel to the NW axis unless otherwise noted. Figure 6.1 presents Raman spectra recorded, at power of 450 kW/cm^2, of two parts of a suspended NW as illustrated in the inserts. The spectrum acquired outside the trench shows the standard InAs spectrum with the transverse optical (TO) mode appearing at 216 cm^{-1}. For the wire part over the trench, on top of the InAs peak the spectrum contains two additional modes at ~195 and ~260 cm^{-1}. Previously, we showed that these two modes belong to crystalline arsenic[67] appearing as a result of the temperature sensitive oxidation process as described

---

[‡‡‡] *Danish Fundamental Metrology A/S, Matematiktorvet 307, DK-2800 Kgs. Lyngby, Denmark*

above. This indicates that over the trench the laser irradiation increased the temperature of the NW to have a considerable oxidation while the temperature was not sufficient for the NW segment on the substrate to form a detectable amount of arsenic.

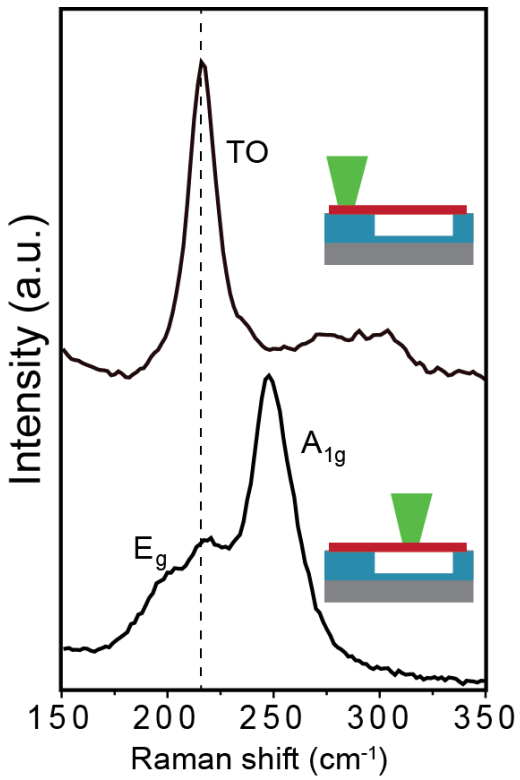

Figure 6.1 *Raman spectra of a suspended InAs NW, recorded as indicated in insert schematics*

Spatial variation and locality of the oxidation process was studied, Raman spectra where recorded along the suspended NWs with a step-size of ~100 nm. Figure 6.2 shows typical results of such a scan. The particular device is shown in Figure 6.2(a) with indications of the positions of the recorded spectra. Figure 6.2(b) maps the normalized spectra as a function of Raman intensity and scan position. While moving from the supported to the suspended part of the NW, the arsenic spectrum appears abruptly over a distance of ~200 nm, as evident in Figure 6.2(c). This scale is comparable to the size of the laser beam, which was used both for inducing and detecting the oxidation reaction.

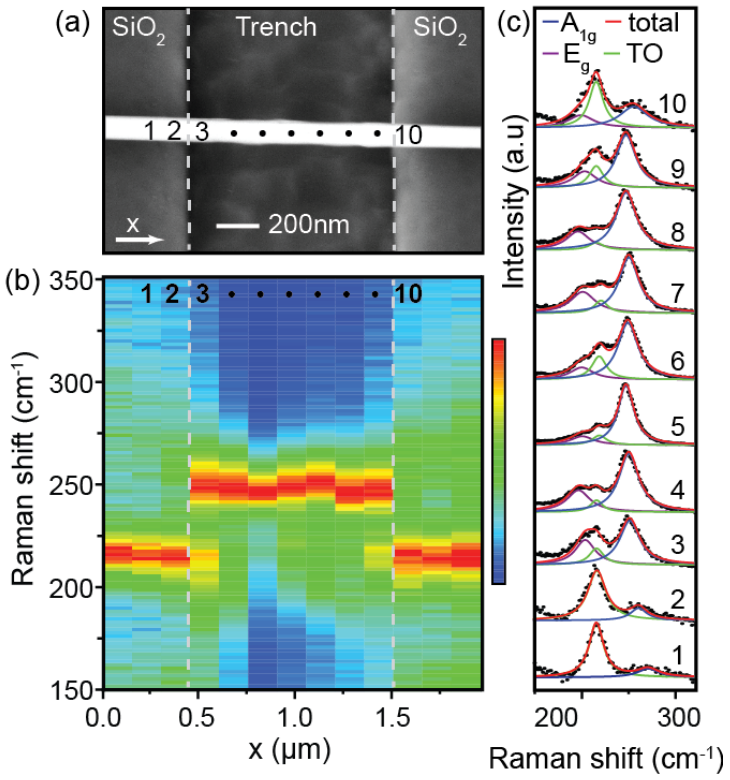

Figure 6.2 *(a) SEM image of the measured NW. The NW has a diameter of ~100 nm and is suspended over a 1 μm trench. The numbers indicate the position along the NW where spectra were recorded. The dashed line in (a) and (b) indicate the position of the trench. (b) Color representation of the Raman intensity as a function of Raman shift and position. Each spectrum was normalized to the maximum As A1g peak intensity. (c) Lorentzian fits of the spectra in (b) with the corresponding numbers.*

The oxidation rate grows exponentially with temperature and is expected to be significant for temperatures above 350 °C[54]. The temperature gradient during laser irradiation was investigated by numerical simulations using COMSOL Multiphysics. The model consists of a 1000 μm^3 Si block with boundaries fixed at 293 K, a 200 nm thick SiO_2 capping layer with a 150 nm deep and 1 μm wide trench bridged by a 7 μm long hexagonal InAs NW with a diameter of 100 nm. Bulk materials parameters were used except for the NW thermal conductivity where the experimental value, k_{InAs} = 10 W/mK, was used[69]. Assuming a Gaussian beam profile, the reflectivity of InAs at 514.5 nm and, assuming total absorption, the NW absorbs ~60 % of the energy of the incoming beam.

Figure 6.3(a) shows the temperature profile (black lines) of the suspended NW, as in the sketch on top, simulated for various positions of the laser using a power chosen to match that of the experiment. The maximum temperature was then found for each data set and plotted as a function of the position along the NW (red trace). Because of the reduced heat dissipation, significantly higher temperatures are reached at the suspended part of the NW and the maximum temperature is achieved when the laser excites the NW at the centre of the trench. Close to the trench edges we find a considerable temperature gradient of ~600 K/µm resulting in a temperature difference of 120 K over 200 nm. This then provides an explanation for the abrupt appearance of the A_{1g} arsenic mode over the trench. Figure 6.3(b) shows the experimental integrated area of the arsenic A_{1g} peak normalized to the total integrated area of the total spectrum along the NW extracted from spectra in Figure 6.2(b). The increase follows the calculated temperature with a minor dip in the middle region of the trench.

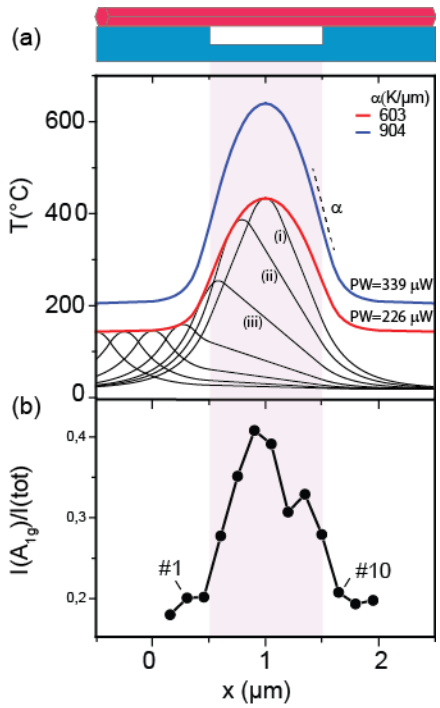

Figure 6.3 *Calculated temperature profile along a 100 nm diameter InAs NW suspended over a 1 µm trench. Top panel shows the geometry. (a) shows the temperature profile along the nanowire, (i) , (ii) and (iii) are for laser positiones at the center of the trench, 0.25 µm from the center and at the edge of the trench, respectively. The red curve shows the maximum temperature attained at position x when scanning the sample with a the laser. The blue curve shows the corresponding curve for a 50 % increase in the laser power. The integrated area of the arsenic A_{1g} mode normalized to the total inegrated area extracted from from Fig. 2(b).*

We have shown above that the temperature of the irradiated NW is sensitive to the contact with the substrate and also to the thermal conductivity of the substrate. For comparison we list Raman spectra recorded of a group of NWs (same growth as studied before) deposited on a verity of substrates in Figure 6.4. spectra were measured at same conditions of laser power and polarization mentioned earlier.

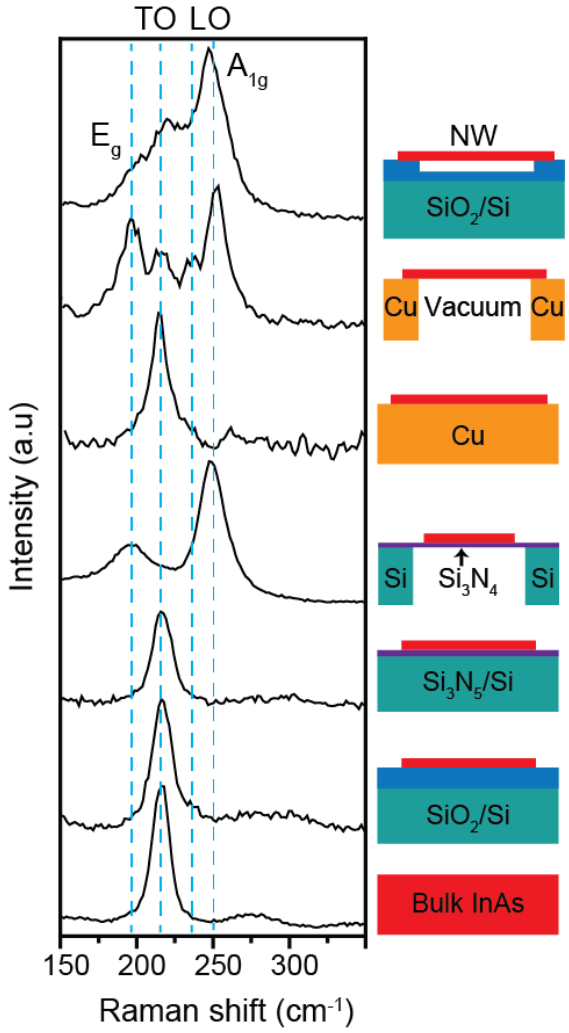

Figure 6.4 *Stack of Raman spectra recorded, at parallel polarization configuration, of InAs NWs deposited on variety of substrates indicated in the sketches at the right.*

All Raman spectra includes the TO mode at ~216 cm^{-1}, similar to the measured InAs bulk spectra with the same crystal direction. On the other hand, spectra of suspended NWs (over trench and vacuum) and NW deposited on a 50 nm Si_3N_4 membrane contain the arsenic E_g and A_{1g} modes at ~190 and ~250 cm^{-1}, respectively. This is consistence with the oxidation effect caused by additional heating, explained above, due to the lack of a dissipating substrate. High intensity (compared to TO) InAs LO peak is observed at ~240 cm^{-1} for the NW on vacuum, and a low intensity one is observed of NW on Cu. This arbitrariness in detecting the LO mode confirms its relation to the NW structure (stacking faults or change in facet).

6.1.2 Electronic properties of oxidized InAs NW

The results of Figure 6.2 and Figure 6.3 show that engineering the substrate can act as an effective route to rationally determine the positions where oxidation should occur along the NWs. As the oxidation process leading to the formation of crystalline arsenic occurs at the surface and the Raman spectra in Figure 6.2 contain the InAs TO mode also at the positions showing the arsenic modes we expect that a significant part of the InAs core remains intact. This has previously been demonstrated by TEM for oxidized InAs NWs suspended on TEM membranes[67] (see chapter 5). To investigate the electrical properties of the oxidized NWs, electrical devices consisting of InAs NWs bridging a 1 µm trench and contacted on both sides by 10/120 nm of Ti/Au Ohmic contacts were fabricated (Figure 6.5(a) shows SEM image of the measured device). The highly doped Si back plane of the chip acted as a gate electrode to electrostatically tune the carrier density of the suspended NW when biased by a voltage V_g. Figure 6.5(c) shows the conductance of the NW as a function of V_g before laser irradiation. The conductance increases with more positive V_g showing that the nanowire acts as an *n*-type semiconductor which is common for undoped InAs NWs[70].

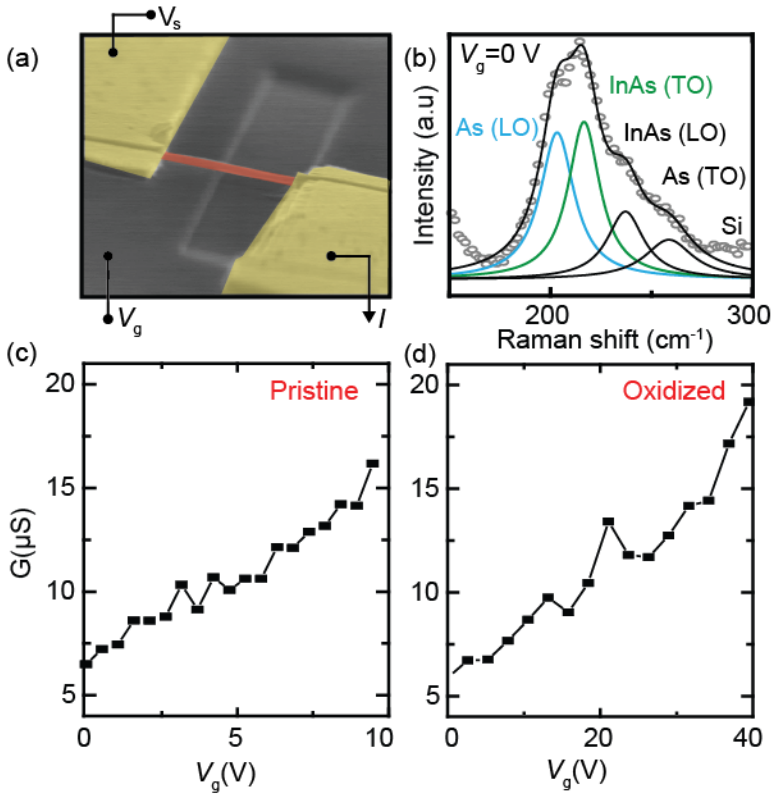

Figure 6.5 *(a) An SEM image of the measured device. (b) Deconvoluted Raman spectra of the NW at zero gate voltage, the peak at 300 is the silicon peak which was not considered in the fit. (c) and (d) Suspended NW conductance as a function of applied back gate voltage before and after laser irradiation.*

Figure 6.5(b) shows the resulting Raman spectrum after irradiating the suspended part of the NW with an irradiance of 450 kW/cm^2. The arsenic modes characteristic of the oxidation process are observed. We note that relative to the InAs TO mode, the arsenic peak has a lower intensity compared to the sample without electrical contacts in Figure 6.2. This is generally observed for contacted NW, and suggests a lower temperature of the contacted NWs due to more efficient thermal anchoring by the metal contacts. The electronic conductance of the NW after the oxidation is shown in Figure 6.5(d). While the overall conductance has dropped by a factor of 1.5-2 the qualitative dependence remains similar to the pristine NW, and upon applying gate voltages up to 40 V the conductance level is restored. Since in InAs NWs, a significant part of the current may be carried by a surface accumulation layer due to a pinning of the Fermi level in the conduction band at the

surface[71,72], we attribute the decreased conductivity to a combination of increased scattering due to increased surface roughness after the irradiation[49,67] and a higher threshold gate voltage as expected for an effectively thinner InAs core[70].

The observed conservation of the electrical properties of the InAs NW after activating the surface oxidation reaction, opens up for the use of this technique to engineer local functionality to electrical nanowire devices. As an example, it was shown in Ref[49] that for GaAs NWs the analogous oxidation process, which converts the GaAs to Ga_2O_3 and crystalline arsenic, significantly decreases the thermal conductivity of the NWs. If the electrical conductivity remains as shown in Figure 6.5(d) this suggest an enhanced thermoelectric effect in the treated NWs which may also be further increased by the large temperature gradients caused by the trench geometry[73]. Furthermore the locality of the laser-induced process which results in left-over metallic arsenic may provide a route for welding of NWs into electrically connected circuits or networks[50], and by performing the irradiation in an controlled environment possibly containing metalorganic gasses the technique may allow control of the induced reaction.

However, oxidation of InAs NWs was prevented by protecting the InAs wire by adding a shell of GaInAs. Performing high power measurements on suspended core-shell InAs/GaInAs NWs resulted damaging of the NW instead of forming oxides like the case of pure InAs NWs. Polarized Raman measurements in the high power regime (intensity 450 kW/cm^2) were performed on suspended core shell InAs/GaInAs NWs. Figure 6.6(a) and (b) show SEM images of the measured NWs deposited on 1µm and 2 µm wide trenches after the measurements. It is obvious that laser irradiation had caused damage to the NW in both cases.

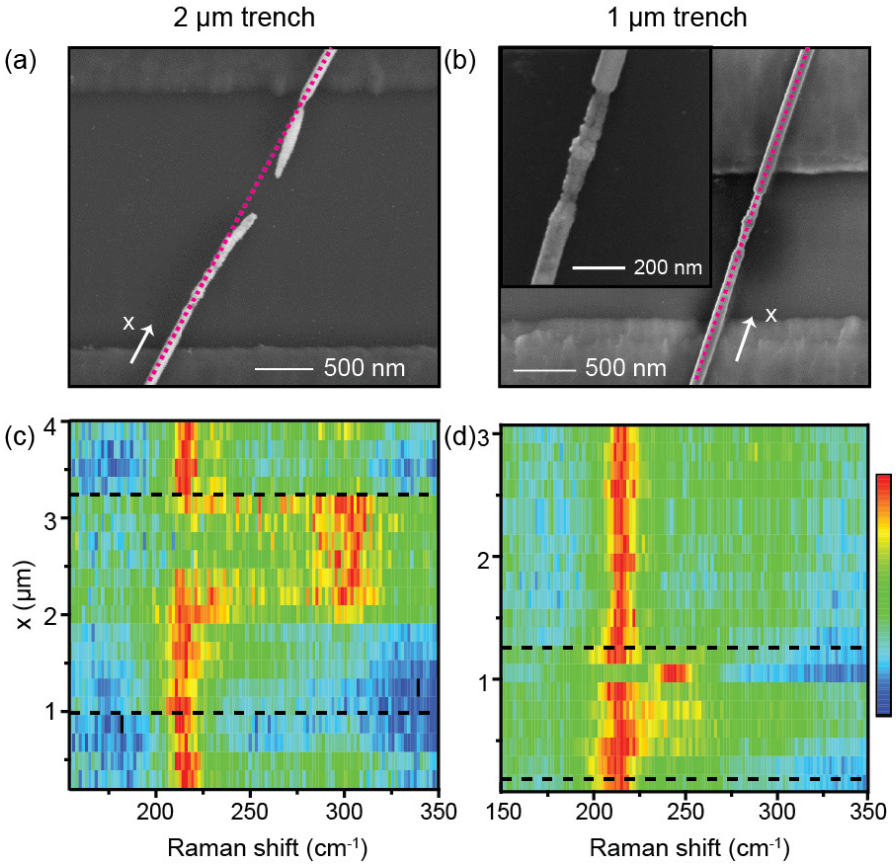

Figure 6.6 *(a) and (b) SEM images of the measured NWs in (c) and (d), respectively, after measurement. (c) and (d) Raman line scans of suspended core-shell NWs, normalized to the maximum TO mode. Trenches are indicated by the dashed lines.*

The measured spectra, presented as normalized line scans at parallel polarization, in Figure 6.6(c) and (d) show the InAs TO mode at ~216 cm^{-1} and an LO mode at ~240 cm^{-1} in one spectrum at the 1 µm trench edge. Surprisingly, the spectra do not contain any trace of the arsenic or oxides peaks. The peaks at 300 cm^{-1} in (c) are related to the silicon substrate and the NW signal does not appear, since the wire was broken (as shown in the SEM image in Figure 6.6(a)). We also performed polarized Raman measurements on the same NWs deposited on silicon nitride membrane with the same power and the Raman spectra contained only the InAs TO mode. Although, oxidation of suspended GaAs NWs, forming oxide compounds including crystalline arsenic, at high laser power density, has been reported[49]. In our case no oxides signal was observed from any measured NW.

6.2 Conclusions

In conclusion, we showed that by a combination of engineered micro trenches in silicon substrates and focused laser irradiation, local oxidation on the scale of ~200 nm could be induced in InAs nanowires. The local surface oxidation was confirmed by micro-Raman spectroscopy and was found to be consistent with numerical simulations of the temperature profile of the suspended NW. By incorporating suspended NWs into electrical devices we showed that the electrical properties of the oxidized nanowires are consistent with a conducting semiconductor core of reduced diameter demonstrating the viability of this technique for engineering functionality into electrical devices.

Chapter VII

7. LO phonon-plasmon coupled modes

This chapter describes our attempt to measure the LO phonon-plasmon coupled modes by low power Raman measurements. First, a theoretical background is present as well as earlier experiments on bulk InAs. Consequently, the results of our measurements on suspended NWs are presented; unfortunately the coupled modes were not detected.

7.1 Introduction

In polar semiconductors including the III-V group, a macroscopic longitudinal electric field is generated by the uniform displacement of the oppositely charged atoms associated with the longitudinal optical phonon. On the other hand, free carriers, which can be produced by doping or by thermal or optical excitation, also exhibit a screening electric field. This plasma (free carriers) oscillates collectively in a form of simple longitudinal harmonic oscillator at a natural frequency $\boldsymbol{\omega_p}$. At a frequency range close to the LO phonon frequency the collective plasma oscillations can couple to the macroscopic electric field of the LO phonons, forming the so called LO phonon-plasmon coupled modes (LPPC)[74]. The LPPC modes were first predicted by Varga[75], and first observed with Raman spectroscopy of n-type GaAs by Mooradian and Wright[76]. Later, many studies, theoretical and experimental, of the LPPC modes in polar semiconductors have been reported[74,76–83]. A very interesting method (which will be discussed later) was also established, where the frequency and the bandwidth of the high-frequency LPPC mode can be used to determine the carrier concentration and mobility[77] which are key parameters for characterizing the electrical properties of semiconductors. In Ref. [84], this method was demonstrated to work well, especially, in determining the carrier concentration, while the mobility values were a bit far from the results of electronic Hall measurement of the same samples. Thus, the detection of the coupled modes has a huge advantage in providing a non-invasive contact-less method which can determine the free carrier concentration and mobility in the NW. In particular for NWs

it would be attractive, considering the geometry of the NW where the standard Hall bar measurements are very challenging. In the following paragraphs a short introductory theory of the coupled modes will be presented. Then follows, the experiments performed by us in the attempt to detect the coupled modes in InAs NWs by modulating the NW surface carrier density. This was done by measuring on suspended NWs with the following functionalities: conventional InAs NWs with and without an external control of carrier density, achieved by applying an external electric field. Core-shell InAs/GaInAs NWs where surface carrier would be depleted.

7.2 Theoretical background

When the natural plasma frequency resonate with the LO phonon a coupling will occur. This coupling can be detected using Raman spectroscopy where two extra peaks may be present in the measured spectra instead of the LO peak (the number of the observed peaks and frequency depends on the properties of the measured semiconductor as we will see latter). The Raman scattering intensity of the coupled modes is proportional to the dielectric response function $\varepsilon(0,\omega)$ as [85]

$$I(\omega) \propto Im[-\frac{1}{\varepsilon(0,\omega)}] \tag{7.1}$$

here we will consider the long wavelength approximation ($q \approx 0$), for more accurate expression the proportionality constant will depend on the scattering mechanism which can be one of the following based on the studied system[86,77]: *The deformation potential (DP)* and the *electro-optic (EO)* process or the *charge density fluctuation (CDF).* In general, the dielectric function for polar crystals can be expressed as[75,85]:

$$\varepsilon(0,\omega) = \varepsilon_\infty + \frac{\omega_L^2 - \omega_T^2}{\omega_T^2 - \omega^2 - i\omega\gamma} + \frac{\omega_p^2}{\omega^2 + i\omega\Gamma} \tag{7.2}$$

Here ε_∞ is the high frequency dielectric constant, ω_T and ω_L are the frequencies of the transvers and longitudinal optical modes, respectively, γ and Γ are the atomic and electronic damping factors, respectively. The second term in the dielectric function expresses the

atomic core contribution and the third term represents the electronic contribution in the classical Drude model where the electronic damping factor is given by

$$\Gamma = \mathrm{e}/m^{*}\mu \tag{7.3}$$

where m^{*} is the electron effective mass and μ is the carrier mobility. Since we consider the $q \approx 0$ case the *plasma frequency* can be expressed as[46]

$$\omega_p^2 = \frac{ne^2}{\varepsilon_0 \varepsilon_\infty m^*} \tag{7.4}$$

where n is the free carrier density. The line-shape of the coupled modes can be approximated to $Im(-\frac{1}{\varepsilon})$ in case of low plasmon frequencies, where the difference from the real value can be neglected. For high plasmon frequencies the proportionality factor in (7.1) should be considered[77]. On the other hand, in a low damping regime, the frequency of the coupled modes $\mathrm{L}^{\pm}$ (or $\omega_{\pm}$ in some references) can be determined from $Re\{\varepsilon(\omega)\} = 0$ and is expressed as[87]:

$$\omega_{\pm}^2 = \frac{1}{2}\left\{\left(\omega_p^2 + \omega_L^2\right) \pm \left[\left(\omega_p^2 - \omega_L^2\right)^2 + 4\omega_p^2(\omega_L^2 - \omega_T^2)\right]^{1/2}\right\} \tag{7.5}$$

Figure 7.1 shows the coupled modes frequencies of InAs based on equation (7.5) as a function of carrier density. Thus, carrier density can be determined by finding the coupled modes frequency. Moreover, from the bandwidth of the higher mode peak the electronic damping factor can be determined from which the mobility can be determined as well.

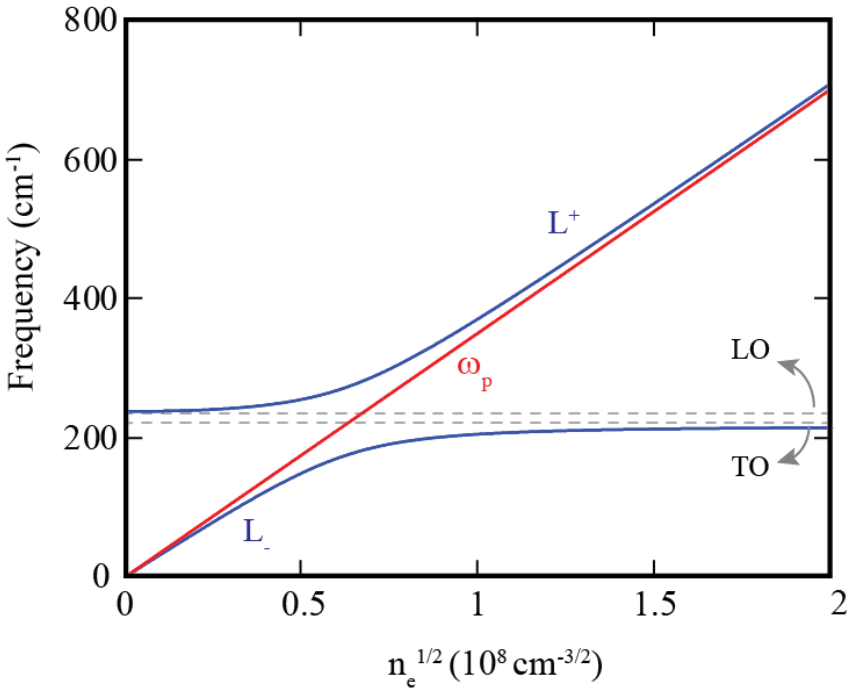

Figure 7.1 *Frequency of the coupled modes of InAs based on equation (7.8).*

A practical method for finding carrier density and mobility is well illustrated by *G. Irmer et al*[77] , where the frequency and bandwidth of the high frequency coupled mode L^+ is used. The shifts from the LO phonon mode can be directly used to estimate the mobility and carrier concentration. This technique is very useful for NWs and, indeed, it has been reported for p-type GaAs NWs[46], self-assembled GaN NWs[88], InN NWs[89] and GaAs/AlAs multi quantum well NWs[90]. Surprisingly, no record was found for InAs based NWs. However, the limiting values which determine the Raman efficiency of the coupled modes are the plasmon frequency (determined by the carrier concentration) and the plasmon damping (determined by the effective mass and the mobility)[81].

7.3 Earlier experiments on bulk III-V systems

Experimentally, the coupled modes were first detected by *Mooradian and McWhorter*[76] in n-type GaAs, which is represented in Figure 7.2(a). They showed that the data fits well with equation (7.5), unlike n-type InAs which *Slusher et al*[91] had shown that effective mass should depend on carrier density for the fit to workout, as shown in Figure 7.2(b) where only the lower branch was observed. While massive amount of

publications treat both n-type and p-type GaAs were reported[74,76,81], a modest number was reported for InAs.

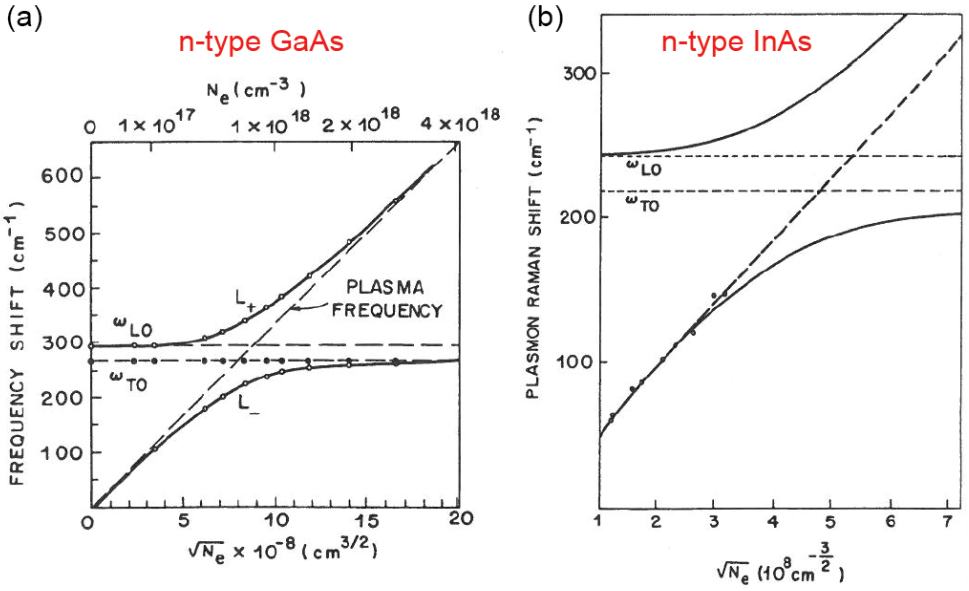

Figure 7.2 *(a) Raman shift of the CPPL modes of n-type GaAs. The solid lines are calculation of equation (2.7). (b) Raman shift of the CPPL modes of n-type InAs. Only plasmon like lower modes were observed. The solid line is the same fit, but with dependency of the electron effective mass on the plasma frequency. Depicted from reference*[92].

After the work of *Slusher et al* which was the first paper on InAs, *Buchner and Burstein*[93] presented a Raman study of n-type InAs with high carrier concentration up to $3.5 \times 10^{18}\ cm^{-3}$. Here also, only the L^- mode was observed beside the appearance of the LO mode which was unexpected. The LO mode was also observed by *Li et al*[80] along with the L^+ and L^- modes, who also performed Raman measurements of highly doped ($n = 4 \times 10^{19}\ cm^{-3}$) n-type InAs. Another interesting approach in measuring the coupled modes in InAs is measuring on Metal-Insulator-Semiconductor structure. This was, initially, performed by *Ching et al*[87], where backgate dependent Raman measurements were performed on both n-type and p-type InAs, at 77 k. Along with the conventional TO and LO modes, an extra peak was observed between the TO and LO. The extra peak frequency was not sensitive to the backgate, i.e. independent of the carrier density in the measured region. However, its intensity ratio to the LO peak was depending on the back-gate voltage, as shown in

Figure 7.3(a), which represents the measured Raman spectra. For negative back-gate voltage, where carriers are almost completely depleted, the extra peak disappeared from the Raman spectra. This peak was attributed to the low frequency coupled LO-phonon mode.

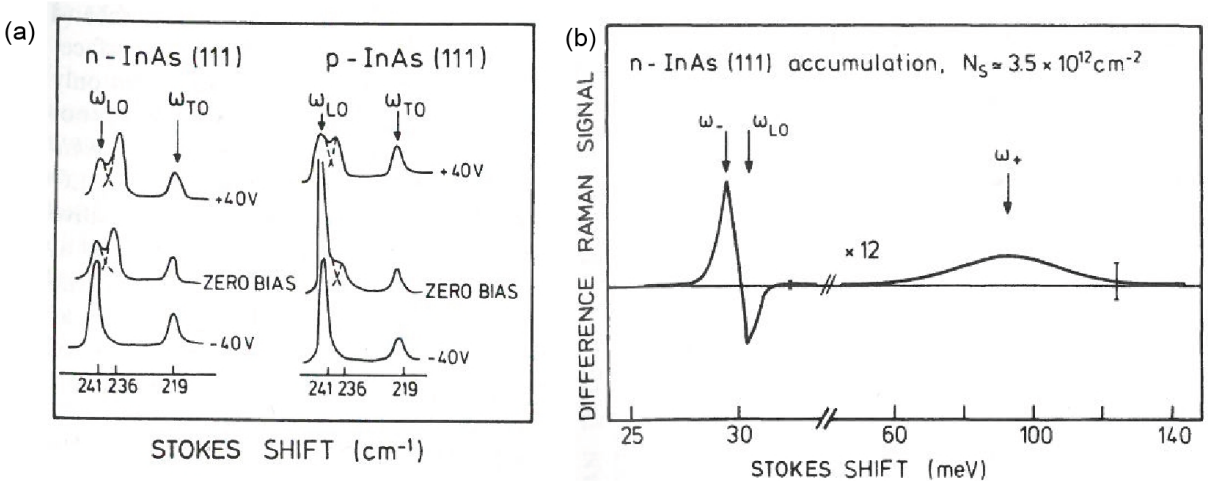

Figure 7.3 *(a) Raman spectra of MIS structure for n-type and p-type InAs. Laser wavelength near resonance. LO and TO phonons are observed, besides, mixed surface intersubband coupled mode. (b) Differential Raman spectrum obtained with fluctuated gate voltage at a n-type InAs surface. Coupled modes are observed at* ω_- *and* ω_+*. A negative signal appears at* ω_{LO} *indicating decrease in the LO intensity. From*[87]

Another similar experiment was proposed by *Abstreiter*[87] , where an AC backgate voltage was applied. A lock-in was then used to detect the surface-electron-induced changes of the Raman spectra. The results are represented in Figure 7.3(b), which shows the two coupled modes. The dip at the LO peak indicates the decrease in the LO mode intensity due to the high accumulation in the surface layer. To our knowledge no more reports of Raman measurements of coupled modes in InAs exist. Unfortunately, the coupled modes were not detected by us either, but the method which was followed in order to detect them will be presented in the following paragraphs.

7.4 Experiments and results

To our knowledge there has not been any publication confirming the observation of the coupled modes on InAs NWs with Raman spectroscopy unlike the case of GaAs which has a similar crystal structure. This could be due to the difference in the electronic properties of InAs which generally has a higher carrier density and mobility besides the electronic accumulation layer at its surface. Therefore, we performed Raman measurements on InAs NWs with the control of their electronic properties. This was achieved either by applying an external electrostatic field (we do not show results of the gating experiments since in all cases the NWs oxidized as discussed in section 6.1.2) or performing measurements on core-shell InAs/InGaAs NWs. We also removed the substrate effect on the carrier distribution by measuring on suspended NWs. Another possible advantage of the suspension is the change of selection rules where the LO mode can be allowed then the coupled modes would be allowed as well since they follow the LO mode selection rules. A study on the effect of the trench on the selection rules is presented in paper 3 in section *List of publications*.

7.4.1 InAs NWs

InAs NWs were suspended over 2 µm wide trenches. Polarized Raman spectra were recorded at 520.8 nm wavelength, 5 kW/cm^2 power density and a ~1 µm laser spot (here a dry objective with 0.75 NA was used). Figure 7.4 presents Raman spectra of a suspended NW measured (a) in vacuum (pressure $\sim 3 \times 10^{-3}\, mbarr$) at 10 K, and (b) at room temperatures. At low vacuum and temperature we minimize the surface interactions with the surrounding medium, besides, the carrier density of a semiconductor is temperature dependent. Spectra were recorded at two points (inside and outside the trench) for excitation polarization parallel ($\parallel$) and perpendicular ($\perp$) to the NW axis. There was no polarizer installed in front of the CCD camera in this measurement.

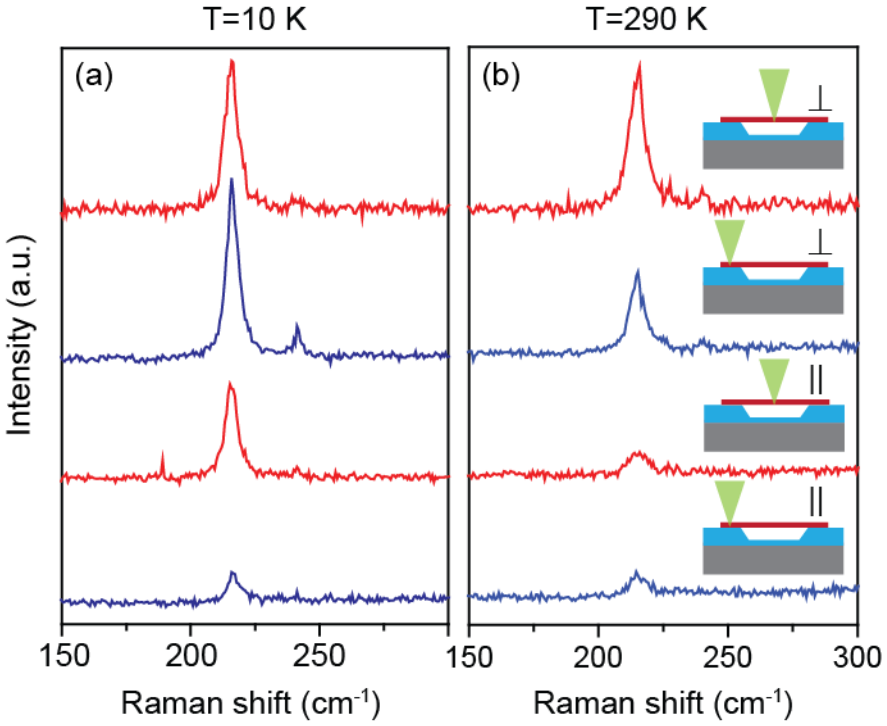

Figure 7.4 *Raman spectra of a suspended InAs NW (a) at 10 K and (b) at 290 K. Green arrows indicate the measured spectrum position. Incident polarization is either parallel or perpendicular to the NW axis.*

The spectra in Figure 7.4(a) and (b) show the InAs TO mode at ~216 cm^{-1} in all cases, also, a low intensity LO mode at ~240 cm^{-1} from the unsuspended part of the NW for perpendicular excitation polarization. The measured spectra do not show any extra features other than the usual spectra of InAs NWs. During measurements at 10 K, very low power was required (5 kW/cm^2) to collect the Raman spectra, otherwise, the exposed area of the NW evaporated completely (detected by optical microscopy).

7.4.2 Core-shell InAs/GaInAs NWs

The GaInAs shell in core-shell InAs/GaInAs NWs, which has a higher electronic band gap than the InAs core, would cause depletion of the electrons from the NW surface. This is due to the bandgap alignment between a high and low gap semiconudtors[94]. Raman measurements were performed on these types of NWs in ambient conditions at 514.5 nm and 160 kW/cm^2 laser power, a high power compared to the pure InAs case. A line scan was

performed with ~100 nm step size, and ~250 nm laser spot size (here an oil objective was used with 1.3 NA). Both incident and scatterd light polarization are parallel to the NW axis. Figure 7.5(a) shows a normalized Raman line scan along the NW as illustrated in (b). The insert is a sketch of the measured NW.

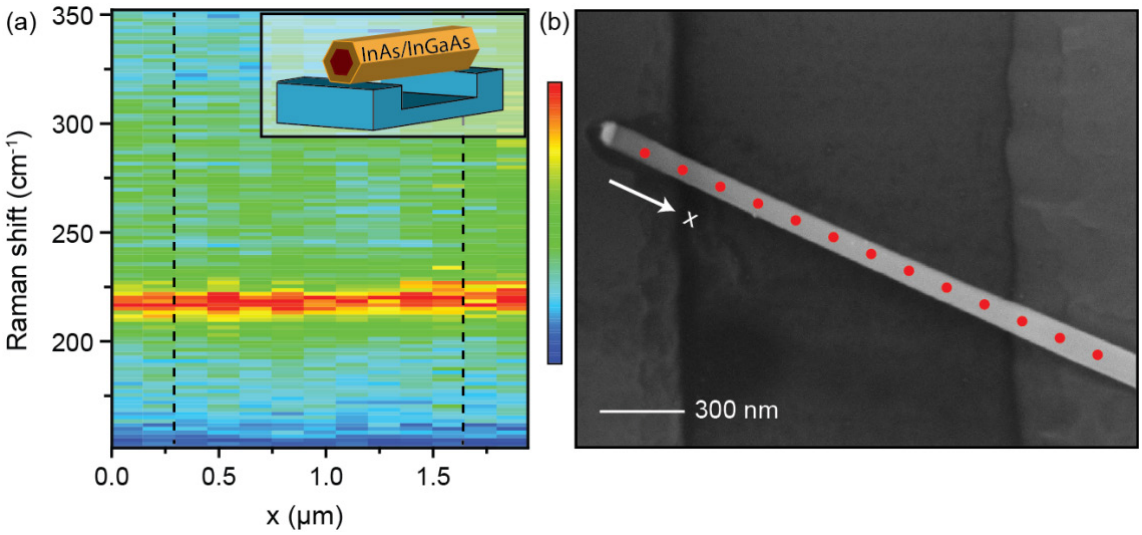

Figure 7.5 *(a) Normalized Raman line scan of a suspended core shell InAs/InGaAs NWs, with parallel polarization configuration; the position of the trench is indicated by the dashed line. The insert represent a sketch of the measured NW. (b) SEM image of the measured NW with the line scan indicated by the red dots indicate.*

The spectra in Figure 7.5(a) show only the TO mode of InAs at ~216 cm^{-1} along the NW. Normalization of the spectra was required due to the enhancement of the Raman signal over the trench. Here also no extra peaks were detected.

7.5 Conclusions

We have attempted to detect the LPPC modes in InAs NWs using Raman spectroscopy by modifying the NWs substrate. The surface accumulation layer of InAs NW was expected to be affected by the substrate and by removing that effect the coupling

between the LO phonon and the plasmons might be induced. It turned out that suspending the NWs had no effect on detecting the LPPC modes since only the InAs phonon modes were detected. However, the same results were found when repeating the same measurements on core-shell InAs/GaInAs NWs where a different carrier distribution is expected. Further experiments, where carriers can be controlled by a back-gate voltage, are more promising as it was the approach for detecting these modes in bulk InAs as well.

Chapter VIII

8. Electronic characterization of heterostructure InAs/GaInAs nanowires

In this chapter we deviate from Raman spectroscopy of NWs as was the focus in the previous chapters. Here we use another characterization method relevant for semiconductor NWs where thermally activated transport experiments are performed on axial heterostructure InAs/GaInAs NWs. The main goal of this experiment is to electrically characterize the barrier potential of the high bandgap segment (GaInAs) included in the low bandgap NW (InAs). For these experiments NWs based devices were fabricated so temperature dependent electrical transport measurements can be performed on the NWs and the results of such measurements are presented in the following chapter.

8.1 Introduction

Starting by the invention of the transistor, electronic semiconductor devices (field effect transistors (FETs), bipolar transistors, modulation-doped high-mobility FETs, light emitting diodes LEDs and diode lasers) have revolutionized modern technology. These devices mainly include functional interfaces or heterostructures which are either dielectric-semiconductor junctions, metal-semiconductor junctions, semiconductor heterojunctions or p-n homojunctions. In an electronic device these heterointerfaces have one of the following functionalities: passivation, electrical isolation, charge transfer and internal field generation[95].

In thin films, when forming heterostructures, the lattice mismatch between the two joined materials will cause misfits and dislocations in the interface area which have undesired effects on the electronic transport and on the optical properties of the heterostructure[96,97]. This problem can be avoided in heterostructure NWs, since the stress induced by the lattice

mismatch can be released into the side facets of the NW, due to the geometry of the NW and the high surface to volume ratio[98]. This allows for unstrained heterostructure NWs with sharp interfaces that are useful for bandgap engineering, although other competitive approaches are possible where the electronic states of semiconductor NWs can be externally engineered[95,99]. Indeed, axial heterostructure NWs have been deployed in devices[100,101] such as resonant tunnel diodes[102], single-electron transistors[103], optically active quantum dots[104] and field-effect transistors[105]. The axial growth of III-V heterostructure NWs by the interchanging of the group V element is well controlled and fairly sharp interfaces in both directions have been reported[106,107]. An example of such structure is shown in Figure 8.1, adopted from Björk et al[108] and *Samuelson, L. et al*[109], where heterostructure InAs/InP NWs were presented.

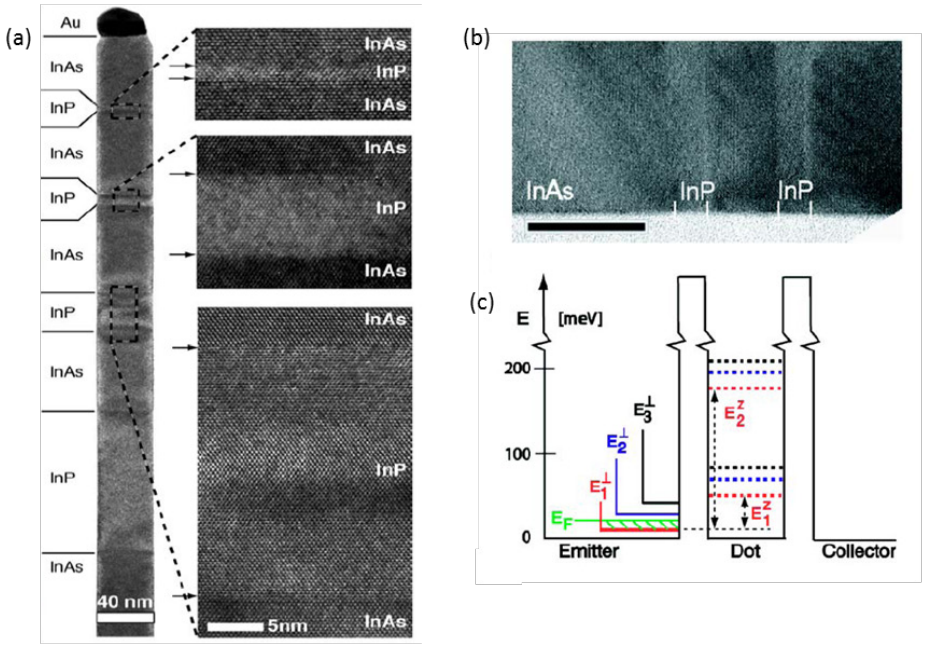

Figure 8.1 (a) High resolution TEM image showing alternating InAs and InP segments in a nanowire, which have interface abruptness on the atomic level. (b) TEM image showing InAs nanowire including double barrier lined up with energy diagram for emitter – barrier – dot – barrier – collector structure (c) Energy band diagram for the emitter and the collector showing the 1D density of state of each quantized state, and the fully quantized energy structure of the 0D quantum dot in between. From Samuelson, L. et al (Lund University)[109].

Figure 8.1(a) presents a TEM image showing the superstructure of an InAs NW which includes multiple InP barriers. The magnified images illustrate the interfaces of the barrier regions. The TEM image of a resonant tunneling diode structure formed by a double

barrier NW is shown in Figure 8.1(b). The corresponding energy diagram of the double barrier structure shown in Figure 8.1(c) illustrates the 1D density of states of the collector and the emitter regions that enclose the centered confined 0D quantum dot with discrete energy levels. For III-V axial heterostructure NWs formed by interchanging the group III element completely, only one interface direction will result the growth of a straight NW[110]. In the case of InAs/GaAs heterostructures, which is in our interest, the growth of straight GaAs on top of InAs NWs is well demonstrated[111,112], while for growth of GaAs on top of InAs the NWs will kink and no straight NW can be achieved[110,113]. This is attributed to the high interfacial energy between the catalyst gold droplet and InAs compared to GaAs. Since the system will tend to minimize its free energy the gold droplet will slide downward and initiate growth in different direction. One way to avoid the NW kinking is the growth of ternary heterostructures as $Ga_xIn_{1-x}As$ instead of pure GaAs. Indeed, heterostructure NWs based on InAs/$Ga_xIn_{1-x}As$/InAs were grown by our group[18]. Such a structure is presented in Figure 8.2 (M. H. Madsen et al[114]), which shows high resolution TEM images of multi-barrier InAs/$Ga_xIn_{1-x}As$ NWs.

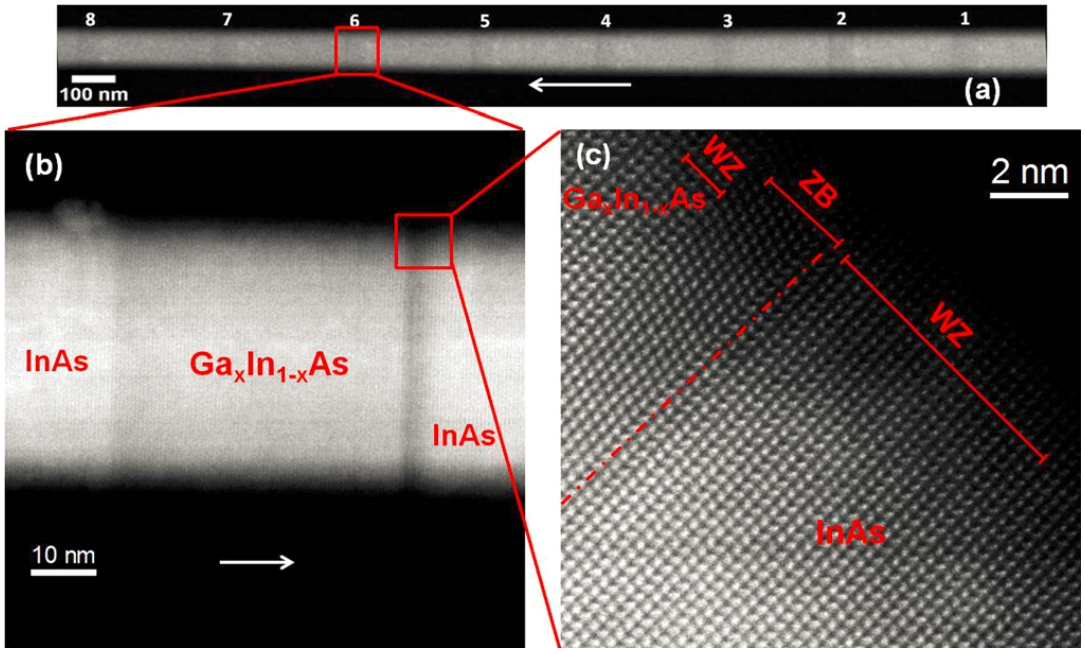

Figure 8.2 *(a) Overview HAADF-STEM image of $Ga_xIn_{1-x}As$ segments in InAs nanowire. (b) High magnification image of on barrier. (c) Atomic resolution HAADF Z-contrast image, the Ga enriched regions are with the dark contrast. From ref*[114]

The higher band gap of the $Ga_xIn_{1-x}As$ segment will cause an off-set in the conduction band resulting a potential barrier inside the NW which could enable engineering of the NW band structure. The potential barrier height is mainly controlled by the Ga mole fraction x, which will be shown in this chapter to be limited by the NW kinking. Further attempts to grow pure axial InAs/GaAs NW heterostructures with sharp interfaces was, eventually, realized by M. E. Messing et al[115], by controlling the phases (WZ or ZB structure) of the two segments. This was optimized by K. A. Dick et al[116] who showed that by pulsing the Ga source before growing the GaAs segments one can obtain sharper interfaces and the radial growth will be limited. Very recently, D. Scarpellini et al[31], succeeded in avoiding the gold catalyst limiting effect by growing self-assisted axial InAs/GaAs heterostructure NWs with atomically sharp interfaces.

In this chapter we will present a study performed on $InAs/Ga_xIn_{1-x}As$ heterostructure NWs grown in-house. The barrier formed by the bandgap engineering at the $Ga_xIn_{1-x}As$ segment will be identified and electronically characterized by thermionic emission measurements[§§§].

8.1.1 Electrical properties of $InAs/Ga_xIn_{1-x}As/InAs$ NWs

When two different types of semiconductors (S_1 and S_2) are, hypothetically, placed adjacent to each other they will form a heterojunction. These two materials can have different band structure and the discontinuity in the conduction or valence band can be represented by a constant potential term V(x) as illustrated in Figure 8.3(a). When a high bandgap semiconductor is sandwiched between two layers of lower bandgap it will form a barrier with certain height and width (see Figure 8.3(b)). The barrier height depends on band gap alignment of the two materials as well as the lattice mismatch which can modify the strain in the barrier region, in turn affecting the barrier band gap. The barrier width is mainly depending on the actual width of the barrier segment.

[§§§] In the remaining of this chapter the $Ga_xIn_{1-x}As$ segment would be referred to as the barrier in the nanowire.

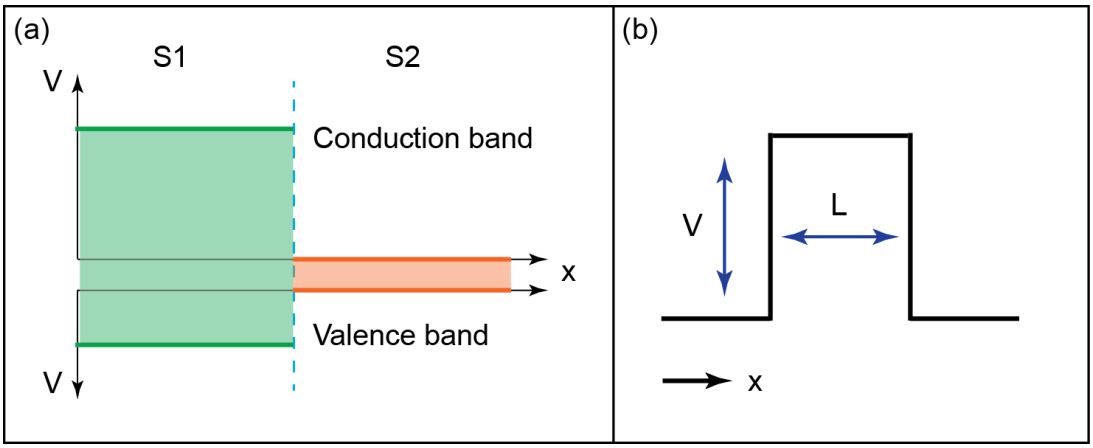

Figure 8.3 *Diagram of (a) the one dimensional potential V(x) that occurs at the heterojunction (at the dashed line) between two semiconductors with different bandgaps S1 and S2 and (b) single barrier structure.*

When applying an electric field perpendicular to the sandwiched layers (x direction in Figure 8.3(b)), a current may flow across the barrier due to two mechanisms:

1. *Tunneling:*

Free carriers with energy less than the potential height V(x) of the barrier will either be reflected at the barrier or tunnel through the barrier with a finite probability. The probability for an impinging carrier to tunnel through the barrier and contribute to the current, is denoted as the transmission coefficient[117]. In the following study the tunneling effect will be neglected since the thermally activated transport (used in our analysis for barrier extraction) is dominated by the thermionic emission discussed below.

2. *Thermionic emission:*

At room temperature, the transport across the barrier along the NW will be governed by thermionic emission, where carriers are thermally excited and have large enough energy to pass over the barrier. In this case, the quantum tunneling will be neglected compared to the thermal effect.

The barrier height can be calculated based on thermally activated transport over the barrier[118]. In this classical model, which is relevant at low bias voltages[108,119], the thermally

activated current across a barrier is related to the temperature according to the following equation[118]

$$I(T) = AA^*.T^2.exp\left[\frac{-q(\emptyset_B - V)}{k_B T}\right] \tag{8.1}$$

where A^* is the effective Richardson coefficient, A the area of the transport channel cross-section, T temperature, k_B Boltzmann constant, $q\emptyset_B$ the barrier height and V is the applied potential.

The barrier height can be extracted by measuring the linear response (zero-bias) conductance G as a function of temperature, given by the following expression:

$$G(T) = \frac{dI}{dV}$$
$$G(T) \propto C.T.exp\left[\frac{-q(\emptyset_B - V)}{k_B T}\right] \tag{8.2}$$

where C is a constant

Equation (8.2) of the conductance was shown to be relevant for NW systems[119]. The barrier can be extracted by plotting the linear dependence of ln(G/T) vs 1/T where the barrier height can be extracted from the (negative) slope.

8.1.2 Barrier height estimation

The height of the barrier formed in the heterostructure InAs/$Ga_xIn_{1-x}As$/InAs NW is basically the offset of the conduction band. We expect this value is approximately similar to the bulk system. The conduction band offset is controlled by the barrier segment bandgap and the bandgap alignment of the different sandwiched materials. The bandgap alignment calculated by Palankovski, V and Nam, H. *et al* [120,121] is presented in Figure 8.4[120] and shows a slight deviation in the center of the bandgaps of GaAs and InAs (the red lines are symmetric around zero). The InAs conduction band is slightly shifted downward, which could decrease the barrier efficiency. For simplicity, in this thesis, the barrier height is estimated to be the direct difference in the bandgaps of the two interfaces divided by two.

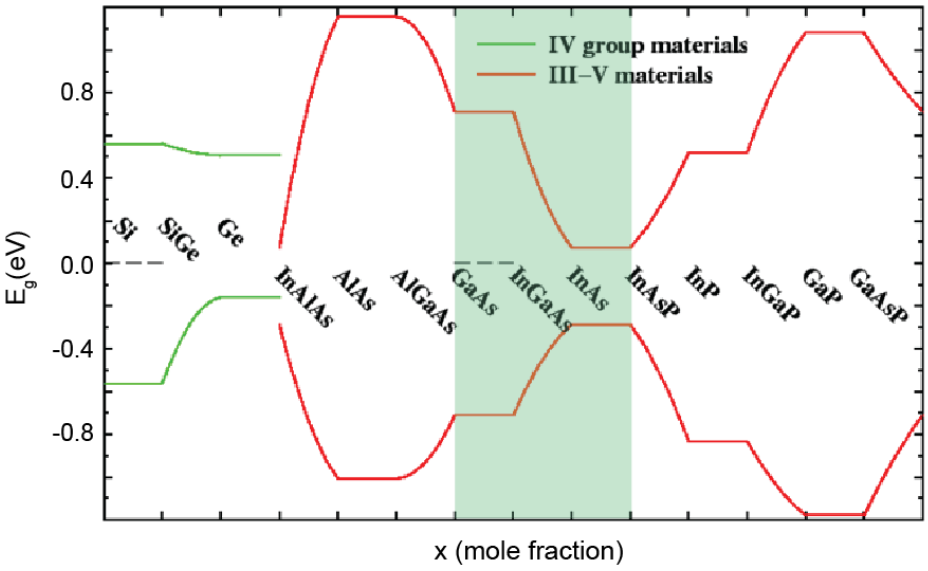

Figure 8.4 *Band gap alignment calculated for a group of semiconductors. Adapted from Palankovski* [120].

The band gap of the $Ga_xIn_{1-x}As$ segment is controlled by the Ga mole fraction (x), strain and the growth direction[122]. For an unstrained barrier with minimum lattice mismatch, the band gap can have the form[123]

$$E_{g1}(x) = 0.35 + 0.63x + 0.45x^2 \quad (eV) \tag{8.3}$$

while for a strained $Ga_xIn_{1-x}As$ junction (high lattice mismatch) the band gap will depend on strain which in turn depends on the value of (x). in this case a good estimate of the bandgap will be the following[122,124,125]

$$E_{g2}(x) = 0.77 + 0.21\,x + 0.45x^2 \quad (eV) \tag{8.4}$$

According to the previous equations, one can estimate the barrier height from the Ga mole fraction (x). Figure 8.5 represents the calculated bandgap of $Ga_xIn_{1-x}As$ as a function of the Ga mole fraction according to equations (8.3) and (8.4), respectively.

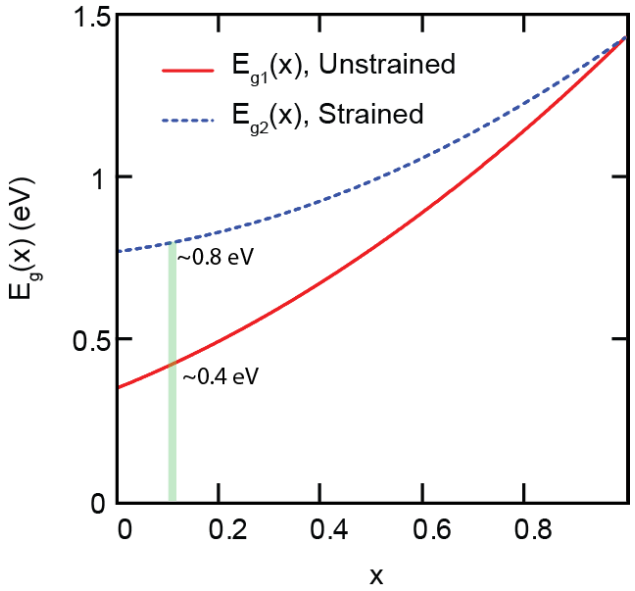

Figure 8.5 *The bandgap E_g of $Ga_xIn_{1-x}As$ as a function of the Ga mole fraction x. $E_{g1}(x)$ and $E_{g2}(x)$ represent equations (8.2) and (8.3), respectively. The bandgap values for the expected value of x=0.1 are noted.*

Figure 8.5 shows that the bandgap of the $Ga_xIn_{1-x}As$ segment has lower values for an unstrained junction, while the band gap is higher, in particular at low values of x, for a strained segment. Due to growth mechanism, there is a limit on the value of x. For higher values than this threshold the nanowire would kink. This happens during the growth of InAs on top of $Ga_xIn_{1-x}As$, where the gold catalyst particle can slide to a side facet and continue the nanowire growth along a perpendicular direction[18], as discussed in 1.1. Regarding the NWs used in this thesis the value of x was estimated from the growth parameters, but not verified, to be ~0.1. At this value the barrier bandgap is around 0.4 and 0.8 eV for the unstrained and strained barrier, respectively as indicated in Figure 8.5. One can estimate the barrier height $\emptyset_b$, which is the offset in the conduction band assuming a perfect bandgap alignment, to be

$$\emptyset_b = \frac{E_g(GaInAs) - E_g(InAs)}{2}$$

which has the values of 33 meV and 220 meV, for the unstrained and strained barrier, respectively. Based on the bandgap alignment presented in Figure 8.4 one would expect a lower actual value of the barrier height.

The purpose of the following study is to identify and electrically characterize the grown barrier. Two types of heterostructure NWs are investigated, single barrier nanowires and nanowires that include four barriers. The barriers in both types of nanowires have ideally the same Ga mole fraction (x)(based on growth parameters) which should induce similar barrier height. The barriers in both types of NWs have similar dimensions, with a barrier segment of ~20 nm width and a diameter of ~120 nm.

8.2 Experimental

In order to characterize the barrier in a heterostructure nanowire, devices were fabricated so that electronic transport experiments could be performed. An additional requirement for these types of nanowires is the identification of the barrier location, in order to avoid putting contacts on top of the barriers. In the following the device preparation steps will be presented along with the challenges.

8.2.1 Device fabrication

Electronic devices were fabricated on heterostructure nanowires in a conventional FET geometry, described in section 3.2. This was done using conventional e-beam lithography according to the following steps:

1) Devices were fabricated on a base chip of n-doped Si covered with 500 nm SiO_2, which enables applying a back-gate voltage to the contacted NW. The substrate is prepared with Ti/Au bonding pads and alignment marks.
2) Nanowires were ultrasonically removed from the growth wafer and then deposited on the base chip. Subsequently, nanowires were located using either optical or scanning electron microscopy.

3) Ti/Au (10/120 nm) source and drain contacts to the chosen NWs were fabricated. This step includes removal of native oxides, which was done by either Sulfur passivation, or Kaufmann ion milling (see p. 36).

4) The chip, with contacted nanowires, was glued to a chip carrier using conductive silver paste and bonded.

8.2.2 Determination of barrier position

The fabrication of Ohmic contacts to the NW that includes a barrier requires an alignment between the contacts and the barrier, so that the barrier is located between contacts. This is not a straight forward procedure, since neither optical nor conventional electron imaging techniques can resolve the barrier. This would not be the case for high resolution TEM microscopy, which however cannot be used due to the substrate limitations, or for advanced SEM equipped with a back-scattering detector, which was unavailable. An alternative way to resolve the barrier position is by using a selective wet etching step. Hence, the nanowires were etched with citric acid, for which the etching rate at the barrier region is higher than the rest of the nanowire. This result in a new morphology of the nanowire which defines the barrier segments by a smaller diameter compared to the rest of the nanowire. The selectivity of the citric acid varies according to the change in the volume ratio to hydrogen peroxide as listed in Table 8.1[126].

Table 8.1 *Citric acid etching rates. From ref* [126]

	Etch Rate Å/min.		
$C_6H_8O_7$: H_2O_2	**GaAs**	**$Ga_{0.47}In_{0.53}As$**	**InAs**
1 : 2	60	1235	655
1 : 1	69	1116	826
2 : 1	85	1438	n/a
3 : 1	2169	n/a	n/a
4 : 1	2235	n/a	n/a
5 : 1	3140	1433	895
7 : 1	2882	1421	n/a
10 : 1	2513	1020	727
15 : 1	1551	1013	n/a
20 : 1	762	665	473
50 : 1	397	303	n/a

According to the estimated value of the Ga mole fraction in our nanowires, the etching rate of $Ga_{0.47}In_{0.53}As$ was considered, since it was the closest found in literature. The used volume ratio of $C_6H_8O_7$:H_2O_2 was 1:2 for which the etching rate of the barrier is two times higher than the rest of the nanowire. Figure 8.6 shows examples of nanowires, etched on the growth chip while the imaged NWs were separated from the growth chip during the etching process. The barriers, indicated by the arrows, are easily resolved on both types of nanowires.

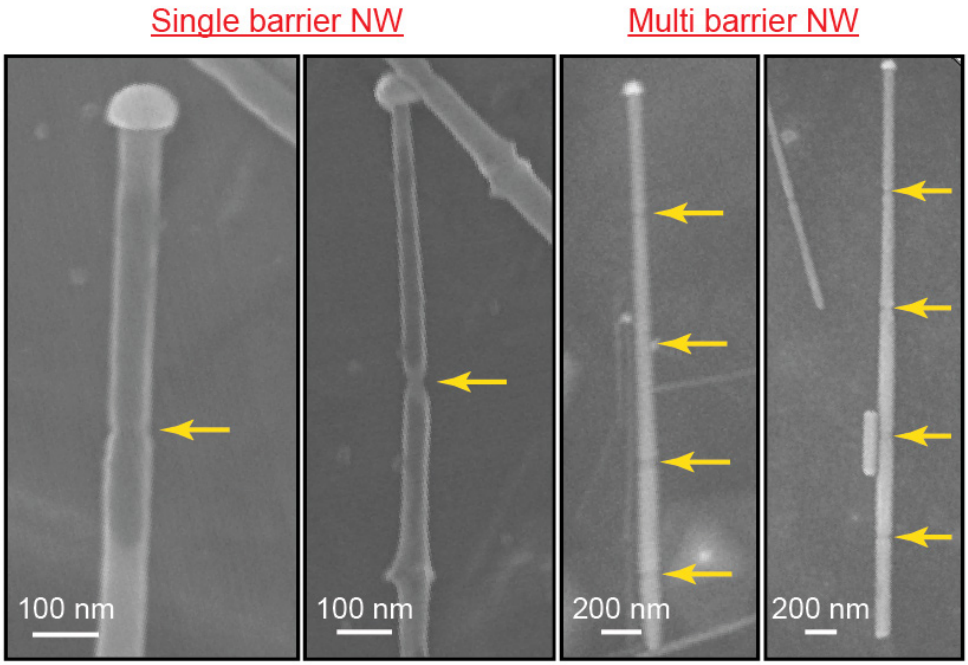

Figure 8.6 *Selectively etched heterostructure nanowires. Etched barriers are indicated by arrows.*

The previous selective etching experiments provide a rough estimate of the barrier position, where the NWs were found to have a relative uniform distribution of the barriers along the NW, regarding the NWs with four barriers. However, the selective etching method is limited by the barrier thickness and the Ga mole fraction. An attempt to be selective etching resolve <10 nm thick barriers with SEM was not successful. Besides, the etching rate and isotropy is different when performing etching on NWs deposited on a substrate. More efforts are needed to optimize the etching process in order to enable the modification of the NW geometry[127–129], so that the NW would be uniformly narrowed at the barrier regions

producing higher radial confinement and a much complex morphology could be engineered, possibly desired for quantum transport experiments.

An exact positioning of the barrier will enable accurate contacts relative to the barrier position. Although, this may add extra barriers to the measured device due to thinning of the NW diameter induced by the etching process. A selective etching step was included in the device fabrication process (NWs contacts), right after the NWs were deposited on the chip. Several devices were fabricated but unfortunately no working device was achieved due to the following challenges:

- The efficiency of the selective etching to the NWs deposited on a substrate was not similar to the NWs standing on their growth substrate. Hence, barriers were not easily distinguished, as seen in Figure 8.7(a). The yellow arrows point at the position of the barriers which are not as obvious as in Figure 8.6. Moreover, the whole NW is severely etched and a clear surface roughening can also be observed.
- All NWs that have gone through a selective etching process were eventually over-etched at the contacts area when removing the native oxide on the NW using a wet etching technique. This will influence the nanowire morphology by diminishing the nanowire near contacts regions. An example of such device is presented in Figure 8.7(b).

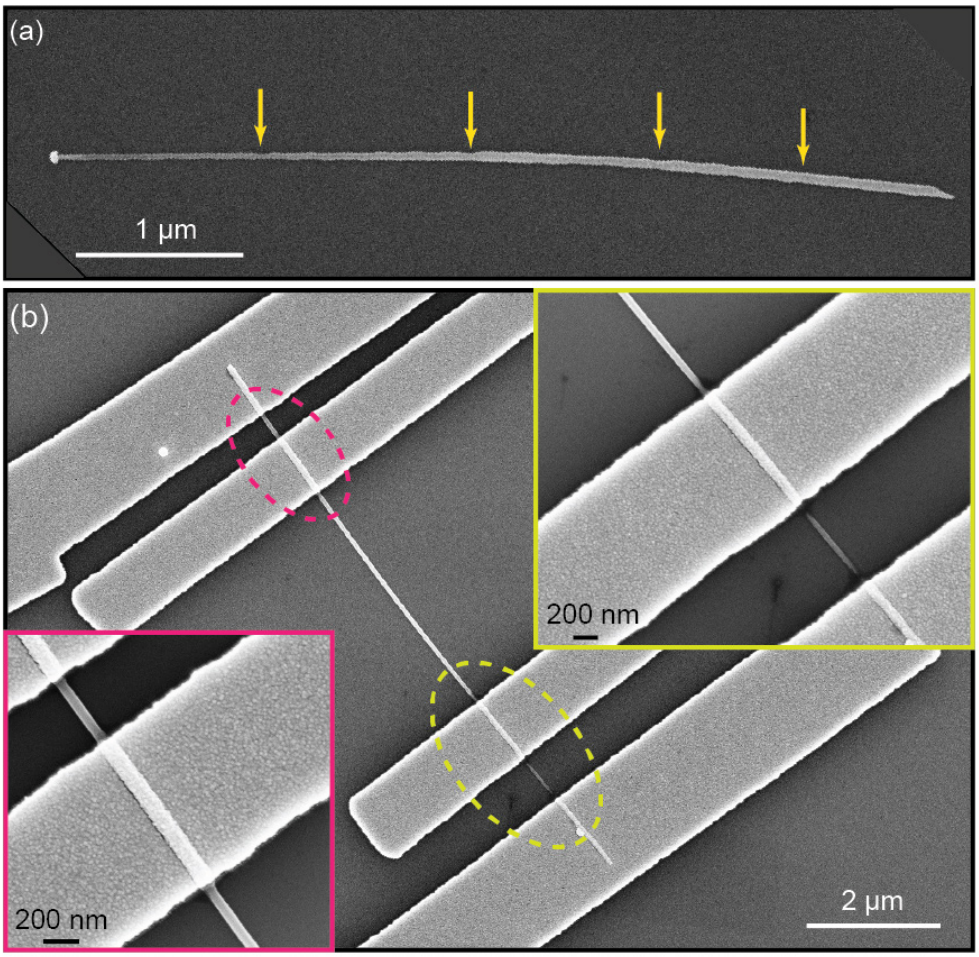

Figure 8.7 *(a) SEM image of selectively etched InAs/GaInAs nanowire deposited on SiO_2 substrate. Arrows indicate etched barriers. (b) SEM image of contacted nanowire. Inserts are higher magnification images of the marked areas with the same border color.*

Figure 8.7(b) shows a four-terminal device of a single barrier nanowire. Inserts are high magnification images of the contacts regions. In the yellow framed area, the central NW segment is completely separated from the contacts, while in the red area >1 MΩ resistance was subsequently measured. The high resistance is due to the low diameter of the NW[72].

We now turn to a detailed description of the electrical transport measurements. A direct comparison of the diameter-dependent resistance is presented in Figure 8.8(a), where

DC I-V measurements were performed on a three-terminal single barrier NW device, presented in Figure 8.8(b).

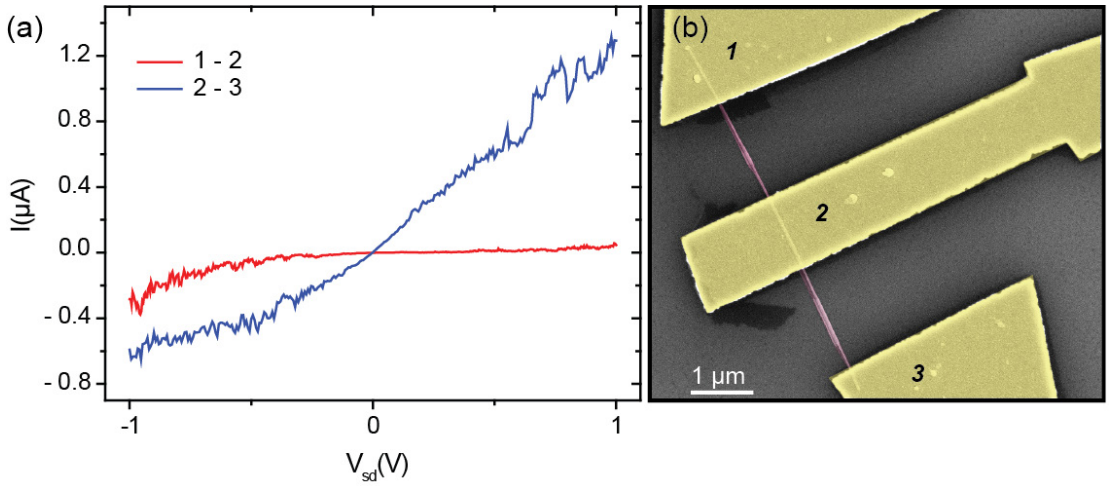

Figure 8.8 *(a) I-V curves of the parts indicated in (b). (b) SEM image of the measured device.*

The I-V curve for the segment enclosed by contacts 1-2 which has a diameter range of ~40-80 nm, reveals a high resistance (~300 MΩ) compared to the I-V curve of segment 2-3 (~2 MΩ), which has a diameter of ~50-100 nm. Such a device is not useful for intrinsic barrier characterization since, on top of the internal barrier, additional barriers are created at different positions of the NW due to the morphological modifications. This problem could be resolved by using a dry etching method instead of wet etching, when removing native oxides. Dry etching does not have an undercut etching effect and would thus lead to ideally sharp features without affecting the overall NW morphology.

8.3 Barrier determination by thermionic emission measurements

Three and four-terminal devices were fabricated on heterostructure InAs/$Ga_xIn_{1-x}As$/InAs NWs. Four-terminal devices would have been optimum to extract the barrier height without the contacts resistance contribution[130], but unfortunately none of the four terminal devices survived for low temperature measurements as they all lost one of the contacts at some parts of the device processing. Measurements were conducted in a standard setup based on the following elements. Lock-in detection was used to measure the

conductance with an AC bias voltage of 100 µV. Voltages were measured using a PC running LabVIEW software, equipped with a National Instruments data acquisition (DAQ) card. The device was cooled down, starting from room temperature 290 K to 300 mK, in a cryogen-free ^{3}He refrigerator. Temperature dependent measurements were performed on a three terminal device shown in Figure 8.9(b). The measured nanowire is a four barrier nanowire. In this particular device, at least one barrier is expected to be located at the segment G_2.

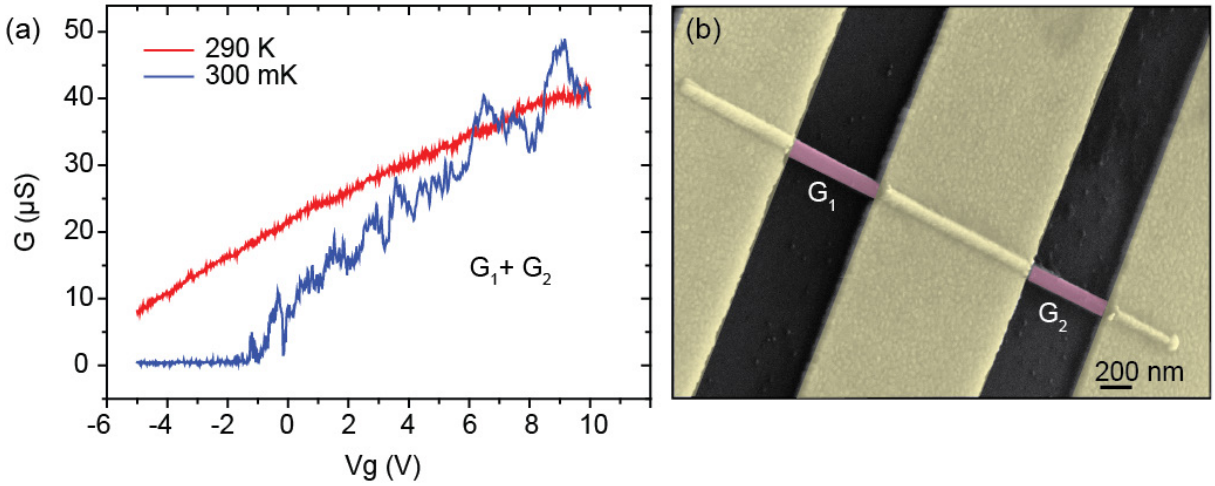

Figure 8.9 *(a) Conductance of the device shown in (b), measured between the outer contacts as a function of backgate voltage, at room temperature and 300 mK. (b) SEM image of the measured device.*

Figure 8.9(a) shows the zero-bias conductance at room temperature and 300 mK, as a function of backgate voltage. The increase in the conductance with increasing backgate voltage indicates an n-type conduction. At 300 mK, the device pinches-off at a gate voltage below -1.5 V.

The measurements of the two devices G_1 and G_2 are presented in Figure 8.10(a) and (b), which represent the conductance of G_1 and G_2, respectively, as a function of the back-gate voltage and temperature. In general, the two devices exhibit similar temperature dependences. At positive gate voltages the conductance increases non-linearly when decreasing the temperature (in the range of T=290-30 K). This is not consistent with thermally activated transport over a barrier, since the conductance is expected to decrease

with decreasing the temperature. The lack of a barrier behavior at positive backgate voltages can be attributed to the increase in carrier concentration induced by increasing backgate voltage. The higher Fermi level will exceed the intrinsic barriers in the NW[131,132].

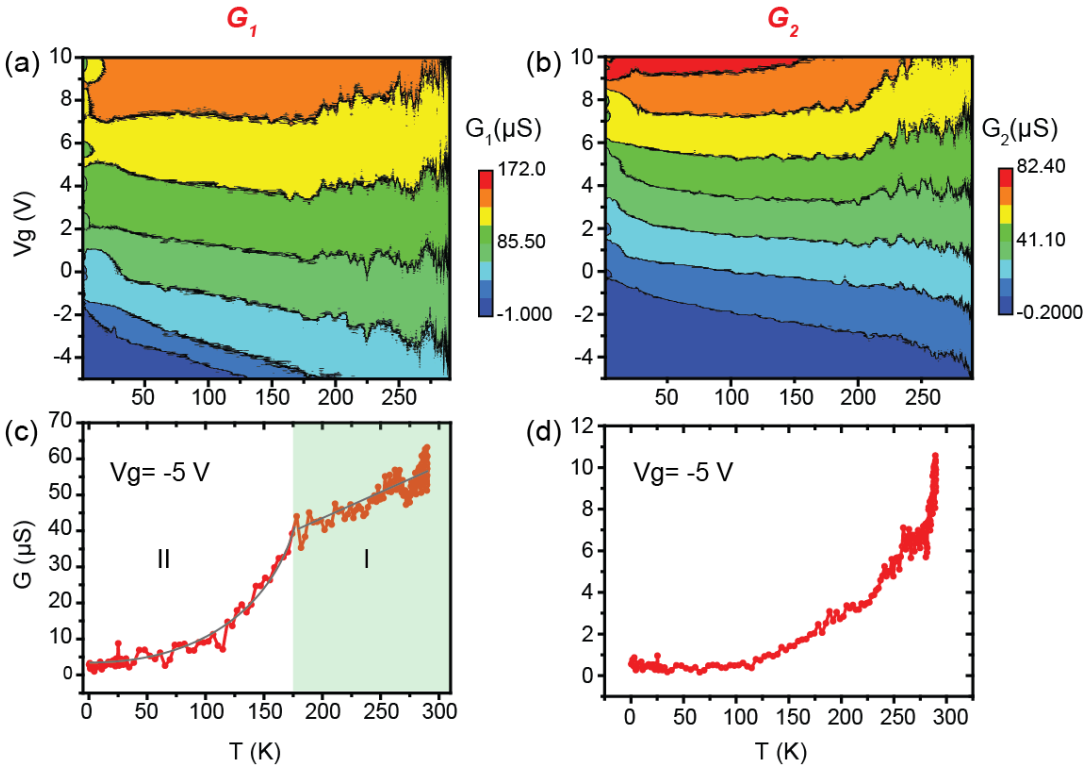

Figure 8.10 *(a) and (b) The conductance of devices G_1 and G_2, respectively, as a function of backgate voltage and temperature. (c) and (d) The conductance as a function of temperature at -5 V backgate voltage. The solid lines in (c) are guide to the eyes.*

At negative backgate voltage, the conductance of the two segments decreases differently with decreasing the temperature. Figure 8.10(c) and (d) show examples of the conductance trace as a function of the temperature at V_g=-5 V. In this range of backgate voltage, where carriers are almost depleted, the intrinsic barrier height is expected to be high enough to affect the transport. The behavior of device G_1 is not well understood, since two temperature ranges are observed in Figure 8.10(c). At T>175 K, region I, the conductance decreases linearly with decreasing temperature while at T<175 K, region II, the conductance decreases nonlinearly with decreasing temperature. Regarding device G_2, the conductance decreases nonlinearly with temperature in the whole temperature range, as shown in Figure 8.10(d).

The barrier height is extracted using equation (8.2), in the temperature region where thermally activated transport is dominant. At low temperature, tunneling through the barrier may be the dominant transport mechanism[119,133], giving rise to deviation from the activated transport behavior. The temperature range where tunneling contribute to the transport will not be part of the analysis presented in this work. Figure 8.11(a) and (b) present Arrhenius-type plots of **ln(G/T)** as a function of the inverse temperature **1000/T** for devices G_1 and G_2, respectively, in the thermally activated range defined by a linear negative slop in the plot, for different values of backgate voltage.

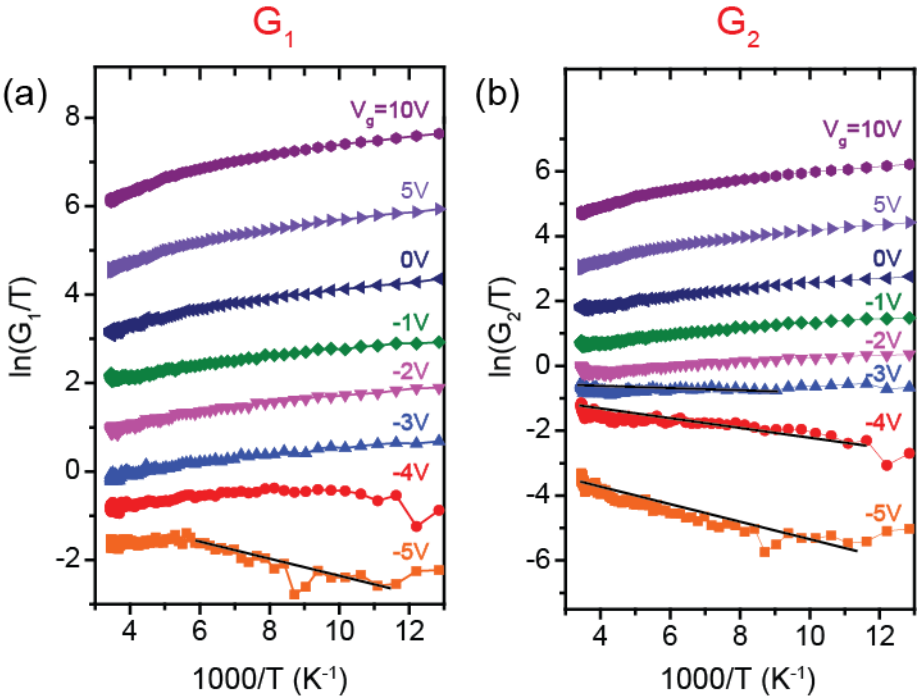

Figure 8.11 *Barrier extraction based on thermally activated transport at different backgate voltages. (a) and (b) represent ln(G/T) vs 1000/T for devices G_1 and G_2, respectively. The solid lines are guide for the eye indicating the fitted parts.*

This temperature range is determined by the linear part of $[\ln(\frac{G}{T}) \propto \frac{1000}{T}]$, and is found to be [290 – 90 K]. In the remaining temperature range, T<90 K, (the nonlinear part) other transport mechanisms will contribute to the conductance as discussed above. The

traces with negative slope represent thermally activated transport, presumably over the barrier[134]. Thus, only the plots for -5, -4, and -3V are fitted for device G_2. For device G_1, at -5 V, two types of linear trends are observed; a first part with a positive slope, and a second part with a negative slope (a similar feature appears at G_2 at the same temperature range). The negative part was fitted by the solid line in Figure 8.11(a). The barrier height values extracted from the fitted lines slopes are presented in Table 8.2.

Table 8.2 *Extracted barrier values for devices G_1 and G_2*

	G_1	G_2		
V_g (V)	-5	-5	-4	-3
E_B (meV)	27	28	17	10

The dependency of the extracted barrier height of device G_2 on the backgate voltage is consistent with a barrier behavior, since it decreases with increasing the backgate voltage. However, the barrier height is slightly lower than the value estimated in section 8.1.2, which is 33 meV and 220 meV at x~0.1, for the unstrained and strained barrier, respectively. The measured barrier height value is closer to the unstrained barrier which also agrees with ref[18], which suggests unstrained barriers in the same type of heterostructure NWs. Regarding device G_1, since the linearity was only found at V_g=-5 V for a limited region of temperature, the extracted barrier is not interpreted as an intrinsic barrier formed by material bandgap engineering, even though, its value is close to the value found for device G_2.

8.4 Conclusions

We have made a considerable experimental effort, mostly fabrication wise, in order to characterize electronic barriers formed in InAs/$Ga_xIn_{1-x}As$/InAs heterostructure NWs. Methods that enabled the identification of the barrier location were developed using chemical wet etching technique. This approach has the advantage of its simplicity and the disadvantage of re-engineering the band structure of the NW, by changing the morphology at certain positions. The latter disadvantage could be potentially turned around by

optimizing the etching technique to engineer uniform and homogenous morphologies of the NWs, and in turn implement these for quantum devices. Devices based on selective etching were fabricated, but unfortunately the NWs were over-etched resulting dramatically high resistance devices. A possible solution to this problem is using a dry etching method to remove the native oxides of the NWs.

A functioning three terminal device based on a four-barrier NW was fabricated. Thermally activated electronic transport showed a barrier behavior at one part of the device, only at negative backgate voltages, with a maximum barrier height value of ~27 meV. This value indicates an unstrained barrier and agree with the expected value based on the Ga mole fraction x, which is estimated based on the Ga flux during growth. However, the main motivation of such structures is the quantum confinement provided by the barriers in the NW band structure. Thus, heterostructure NWs with higher barrier height are required. This can be achieved by increasing the Ga mole fraction, and this is, indeed, a challenge in terms of growing these structures. Recently, at the Center for Quantum Devices, axial InAs NWs were grown including $Ga_xIn_{1-x}As$ segments with Ga mole fraction x~0.5. These NWs are good candidates for fabrication more well-defined electronic devices.

Appendices

A. Table with nanowire batches used in the thesis

Wire ID	Number of Barriers	Characteristics	measurements	Notes
NBI552	no	L=5-7 µm, D=40-140 nm	Raman measurements	Tapered
NBI831	no	Stem L=1µm, D=100nm Kink L=2µm, D=80 nm	Raman measurements	Kinked
NBI268	1	1B, L=2-3 µm, x~0.3-0.4	Two contacts, selective etching	
NBI700	1	1B, L=5-7 µm, x~0.2	selective etching, contact	no RT barrier detected (could be due to poor contact)
NBI791	1	1B, L~7 µm, x~?	Selective etching	
NBI640	1	1B, l~9 µm, x~0.05, barrier length~5nm	Contact	very poor contact due to the diameter of the wire D~30nm
NBI820	4	4B, L~5µm,	TEM images Selective etching, Contacts and transport measurements	Ga ration is too low (barrier ~10 meV)

List of publications

1. *Morphology and composition of oxidized InAs nanowires studied by combined Raman spectroscopy and transmission electron microscopy,* **Rawa Tanta**, Thomas Kanne, Francesca Amaduzzi, Zhiyu Liao, Morten H. Madsen, Esther Alarcón-Lladó, Peter Krogstrup, Erik Johnson, Anna F. I Morral, Tom Vosch, Jesper Nygård, Thomas S. Jespersen- submitted.

    - I did the samples preparation and Raman measurements and the data analysis and interpretation.

2. *Raman spectroscopy and electrical properties of InAs nanowires with local oxidation enabled by substrate micro-trenches and laser irradiation*, **R.Tanta**, M.H.Madsen, Z.Liao, P. Krogstrup, T.Vosch, J.Nygård, T.S.Jespersen – Accepted in Applied Physics Letters.
    - I did the main work in this paper including devices fabrication and installation of the electronic measurement setup on the Raman microscope. Also did the Raman measurements and data analysis and interpretation.

3. *Tuning the response of non-allowed Raman modes in GaAs nanowires,* Francesca Amaduzzi, Esther Alarcón-Lladó, Hubert Hautmann, **Rawa Tanta**, Federico Matteini, Gozde Tutuncuoglu, , T.Vosch, J.Nygård, T.S.Jespersen, Emanuele Uccelli, Anna Fontcuberta I Morral – submitted.
    - This work was based on our idea of substrate engineering. I also contributed in the discussion and data interpretation.

4. *Spin-orbit coupling in InAs nanowire devices: influence of the nanowires crystal orientation.* T. S. Jespersen, P. Krogstrup, A. M. Lunde, **R. Tanta**, E. Johanson, E. Rashba, C. M. Marcus, J. Nygård- in preparation
    - Fabricated some of the devices measured in this paper.

Bibliography

1. Duan, X. & Lieber, C. M. Nanoscience and the nano-bioelectronics frontier. *Nano Res.* **8,** 1–22 (2015).

2. Wallentin, J. *et al.* InP nanowire array solar cells achieving 13.8% efficiency by exceeding the ray optics limit. *Science* **339,** 1057–60 (2013).

3. Duan, X., Huang, Y., Cui, Y., Wang, J. & Lieber, C. M. Indium phosphide nanowires as building blocks for nanoscale electronic and optoelectronic devices. *Nature* **409,** 66–9 (2001).

4. Li, Y., Qian, F., Xiang, J. & Lieber, C. M. Nanowire electronic and optoelectronic devices. *Mater. Today* **9,** 18–27 (2006).

5. Krogstrup, P. *et al.* Single-nanowire solar cells beyond the Shockley–Queisser limit. *Nat. Photonics* **7,** 306–310 (2013).

6. Thelander, C. *et al.* Nanowire-based one-dimensional electronics. *Mater. Today* **9,** 28–35 (2006).

7. Frolov, S. M., Plissard, S. R., Nadj-Perge, S., Kouwenhoven, L. P. & Bakkers, E. P. A. M. Quantum computing based on semiconductor nanowires. *MRS Bull.* **38,** 809–815 (2013).

8. Hofstetter, L., Csonka, S., Nygård, J. & Schönenberger, C. Cooper pair splitter realized in a two-quantum-dot Y-junction. *Nature* **461,** 960–3 (2009).

9. Mourik, V. *et al.* Signatures of Majorana fermions in hybrid superconductor-semiconductor nanowire devices. *Science* **336,** 1003–7 (2012).

10. Affentauschegg, C. & Wieder, H. H. Properties of InAs/InAlAs heterostructures. *Semicond. Sci. Technol.* **16,** 708–714 (2001).

11. Pellegrini, V. New advances on collective phenomena in one-dimensional systems. *Solid State Commun.* **131,** 555 (2004).

12. Dick, K. A. & Caroff, P. Metal-seeded growth of III–V semiconductor nanowires: towards gold-free synthesis. *Nanoscale* **6,** 3006 (2014).

13. Caroff, P., Bolinsson, J. & Johansson, J. Crystal Phases in III--V Nanowires: From Random Toward Engineered Polytypism. *IEEE J. Sel. Top. Quantum Electron.* **17,** 829–846 (2011).

14. Krogstrup, P. Dynamical theory and experiments on GaAs nanowire growth for photovoltaic applications. (2012).

15. Bolinsson, J. The Crystal Structure of III_V Semiconductore Nanowires: Growth and Characterization. (2010).

16. Glas, F., Harmand, J.-C. & Patriarche, G. Why does wurtzite form in nanowires of III-V zinc blende semiconductors? *Phys. Rev. Lett.* **99,** 146101 (2007).

17. Dick, K. A. *et al.* Control of III–V nanowire crystal structure by growth parameter tuning. *Semicond. Sci. Technol.* **25,** 024009 (2010).

18. Krogstrup, P. *et al.* Junctions in axial III-V heterostructure nanowires obtained via an interchange of group III elements. *Nano Lett.* **9,** 3689–93 (2009).

19. YU, P. & Cardona, M. *Fundamentals of Semiconductors: Physics and Materials Properties*. (2010).

20. Alarcón-Lladó, E. Vibrational Properties of ZnO, Group III-Nitrides and Dilute Nitrides Alloys. *PhD thesis* (2009).

21. Möller, M. *et al.* Polarized and resonant Raman spectroscopy on single InAs nanowires. *Phys. Rev. B - Condens. Matter Mater. Phys.* **84,** 085318 (2011).

22. Raman, C. V. & Krishnan, K. S. A new type of secondary radiation. *Nature* (1928).

23. HIBBEN, J. H. THE RAMAN EFFECT and its CHEMICAL APPLICATIONS. *Ind. Eng. Chem., News Ed.* **17,** 556 (1939).

24. MAIMAN, T. H. Stimulated Optical Radiation in Ruby. *Nature* **187,** 493–494 (1960).

25. PORTO, S. P. S. & WOOD, D. L. Ruby Optical Maser as a Raman Source. *J. Opt. Soc. Am.* **52,** 251 (1962).

26. Begum, N. *et al.* Structural characterization of GaAs and InAs nanowires by means of Raman spectroscopy. *J. Appl. Phys.* **104,** 104311 (2008).

27. Cantoro, M. *et al.* Long-wavelength, confined optical phonons in InAs nanowires probed by Raman spectroscopy. *Eur. Phys. J. B* **79,** 423–428 (2011).

28. Hörmann, N. G. *et al.* Effects of stacking variations on the lattice dynamics of InAs nanowires. *Phys. Rev. B* **84,** 155301 (2011).

29. Kumar Panda, J. *et al.* Raman sensitivity to crystal structure in InAs nanowires. *Appl. Phys. Lett.* **100,** 143101 (2012).

30. Pal, S. *et al.* Low- and high-density InAs nanowires on Si(001) and their Raman imaging. *Semicond. Sci. Technol.* **28,** 015025 (2013).

31. Scarpellini, D. *et al.* InAs/GaAs Sharply Defined Axial Heterostructures in Self-Assisted Nanowires. *Nano Lett.* **15,** 3677–3683 (2015).

32. Zardo, I. *et al.* E1(A) electronic band gap in wurtzite InAs nanowires studied by resonant Raman scattering. *Nano Lett.* **13,** 3011–3016 (2013).

33. Yazji, S. *et al.* Pressure dependence of Raman spectrum in InAs nanowires. *J. Phys. Condens. Matter* **26,** 235301 (2014).

34. Pal, S., Aggarwal, R., Kumari Gupta, V. & Ingale, A. Time evolution studies of laser induced chemical changes in InAs nanowire using Raman spectroscopy. *Appl. Phys. Lett.* **105,** 012110 (2014).

35. *PELCO®, 21509-10, Silicon Nitride Support Film, 50nm with 9 each 0.1 x 0.1mm Windows.*

36. Suyatin, D. B., Thelander, C., Björk, M. T., Maximov, I. & Samuelson, L. Sulfur passivation for ohmic contact formation to InAs nanowires. *Nanotechnology* **18,** 105307 (2007).

37. Mizoguchi, K. & Nakashima, S. Determination of crystallographic orientations in silicon films by Raman-microprobe polarization measurements. *J. Appl. Phys.* **65,** 2583 (1989).

38. Zardo, I. *et al.* Raman spectroscopy of wurtzite and zinc-blende GaAs nanowires: Polarization dependence, selection rules, and strain effects. *Phys. Rev. B* **80,** 245324 (2009).

39. Arbiol, J., de la Mata, M., Eickhoff, M. & Morral, A. F. i. Bandgap engineering in a nanowire: self-assembled 0, 1 and 2D quantum structures. *Mater. Today* **16,** 213–219 (2013).

40. Zhang, S., Chou, J. Y. & Lauhon, L. J. Direct correlation of structural domain formation with the metal insulator transition in a VO2 nanobeam. *Nano Lett.* **9,** 4527–32 (2009).

41. Lopez, F. J., Hemesath, E. R. & Lauhon, L. J. Ordered stacking fault arrays in silicon nanowires. *Nano Lett.* **9,** 2774–9 (2009).

42. Dufouleur, J. *et al.* P-doping mechanisms in catalyst-free gallium arsenide nanowires. *Nano Lett.* **10,** 1734–40 (2010).

43. Stefaniak, E. A., Buczynska, A., Novakovic, V., Kuduk, R. & Grieken, R. Van. Determination of chemical composition of individual airborne particles by SEM/EDX and micro-Raman spectrometry: A review. *J. Phys. Conf. Ser.* **162,** 012019 (2009).

44. Majzner, K. *et al.* Raman imaging providing insights into chemical composition of lipid droplets of different size and origin: in hepatocytes and endothelium. *Anal. Chem.* **86,** 6666–74 (2014).

45. Millot, M. *et al.* Raman spectroscopy and magnetic properties of bulk ZnO:Co single crystal. *J. Alloys Compd.* **423,** 224–227 (2006).

46. Ketterer, B., Uccelli, E. & Fontcuberta i Morral, A. Mobility and carrier density in p-type GaAs nanowires measured by transmission Raman spectroscopy. *Nanoscale* **4,** 1789–93 (2012).

47. He, J., Chen, P., Lu, W., Dai, N. & Zhu, D.-M. Laser induced modification and ablation of InAs nanowires. *J. Appl. Phys.* **111,** 094316 (2012).

48. Lu, J. *et al.* Laser modified ZnO/CdSSe core-shell nanowire arrays for Micro-Steganography and improved photoconduction. *Sci. Rep.* **4,** 6350 (2014).

49. Yazji, S. *et al.* Local modification of GaAs nanowires induced by laser heating. *Nanotechnology* **22,** 325701 (2011).

50. Garnett, E. C. *et al.* Self-limited plasmonic welding of silver nanowire junctions. *Nat. Mater.* **11,** 241–9 (2012).

51. Xiong, Q., Chen, G., Gutierrez, H. . & Eklund, P. . Raman scattering studies of individual polar semiconducting nanowires: phonon splitting and antenna effects. *Appl. Phys. A* **85,** (2006).

52. Renucci, J. B., Richter, W., Cardona, M. & Schostherr, E. Resonance raman scattering in group Vb semimetals: As, Sb, and Bi. *Phys. Status Solidi* **60,** 299–308 (1973).

53. Farrow, R. L., Chang, R. K., Mroczkowski, S. & Pollak, F. H. Detection of excess crystalline As and Sb in III-V oxide interfaces by Raman scattering. *Appl. Phys. Lett.* **31,** 768 (1977).

54. Hollinger, G., Skheyta-Kabbani, R. & Gendry, M. Oxides on GaAs and InAs surfaces: An x-ray-photoelectron-spectroscopy study of reference compounds and thin oxide layers. *Phys. Rev. B* **49,** 11159–11167 (1994).

55. Schwartz, G. . Analysis of native oxide films and oxide-substrate reactions on III–V semiconductors using thermochemical phase diagrams. *Thin Solid Films* **103,** 3–16 (1983).

56. Laughlin, D. H. & Wilmsen, C. W. Thermal oxidation of InAs. *Thin Solid Films* **70,** 325–332 (1980).

57. Piscanec, S. *et al.* Raman spectroscopy of silicon nanowires. *Phys. Rev. B* **68,** 241312 (2003).

58. Krogstrup, P. *et al.* Advances in the theory of III–V nanowire growth dynamics. *J. Phys. D. Appl. Phys.* **46,** 313001 (2013).

59. Sibirev, N. V., Timofeeva, M. A., Bol'shakov, A. D., Nazarenko, M. V. & Dubrovskiĭ, V. G. Surface energy and crystal structure of nanowhiskers of III–V semiconductor compounds. *Phys. Solid State* **52,** 1531–1538 (2010).

60. *Elementary Ga is present on the stem due to the initiation of the kink during growth. This could have a catalyzing effect on the oxidation process, but was neglected since the same effect was observed on pure [0001] InAs nanowires.*

61. Oskooi, A. F. *et al.* Meep: A flexible free-software package for electromagnetic simulations by the FDTD method. *Comput. Phys. Commun.* **181,** 687–702 (2010).

62. Heiss, M. & Fontcuberta i Morral, A. Fundamental limits in the external quantum efficiency of single nanowire solar cells. *Appl. Phys. Lett.* **99,** 263102 (2011).

63. Fasth, C., Fuhrer, A., Samuelson, L., Golovach, V. N. & Loss, D. Direct Measurement of the Spin-Orbit Interaction in a Two-Electron InAs Nanowire Quantum Dot. *Phys. Rev. Lett.* **98,** 266801 (2007).

64. Björk, M. T. *et al.* One-dimensional Steeplechase for Electrons Realized. *Nano Lett.* **2,** 87–89 (2002).

65. Krogstrup, P. *et al.* Epitaxy of semiconductor-superconductor nanowires. *Nat. Mater.* (2015). doi:10.1038/nmat4176

66. Wallentin, J. *et al.* Semiconductor-oxide heterostructured nanowires using postgrowth oxidation. *Nano Lett.* **13,** 5961–6 (2013).

67. Tanta, R. *et al.* Morphology and somposition of ozidized InAs nanowires studied by combined Raman spectroscopy and transmission electron microscopy. *submitted* (2015).

68. Madsen, M. H. *et al.* Experimental determination of adatom diffusion lengths for growth of InAs nanowires. *J. Cryst. Growth* **364,** 16–22 (2013).

69. Zhou, F. *et al.* Thermal conductivity of indium arsenide nanowires with wurtzite and zinc blende phases. *Phys. Rev. B* **83,** 205416 (2011).

70. Samuelson, L. *et al.* Semiconductor nanowires for 0D and 1D physics and applications. *Phys. E Low-dimensional Syst. Nanostructures* **25,** 313–318 (2004).

71. Olsson, L. *et al.* Charge accumulation at InAs surfaces. *Phys. Rev. Lett.* **76,** 3626–3629 (1996).

72. Scheffler, M., Nadj-Perge, S., Kouwenhoven, L. P., Borgström, M. T. & Bakkers, E. P. A. M. Diameter-dependent conductance of InAs nanowires. *J. Appl. Phys.* **106,** 124303 (2009).

73. Boukai, A. I. *et al.* Silicon nanowires as efficient thermoelectric materials. *Nature* **451,** 168–71 (2008).

74. Olego, D. & Cardona, M. Raman scattering by coupled LO-phonon—plasmon modes and forbidden TO-phonon Raman scattering in heavily doped p-type GaAs. *Phys. Rev. B* **24,** 7217–7232 (1981).

75. Varga, B. Coupling of Plasmons to Polar Phonons in Degenerate Semiconductors. *Phys. Rev.* **137,** A1896–A1902 (1965).

76. Mooradian, A. & Wright, G. Observation of the Interaction of Plasmons with Longitudinal Optical Phonons in GaAs. *Phys. Rev. Lett.* **16,** 999–1001 (1966).

77. Irmer, G., Toporov, V. V., Bairamov, B. H. & Monecke, J. Determination of the charge carrier concentration and mobility in n-gap by Raman spectroscopy. *Phys. status solidi* **119,** 595–603 (1983).

78. Chen, Y., Hermanson, J. & Lapeyre, G. Coupled plasmon and phonon in the accumulation layer of InAs(110) cleaved surfaces. *Phys. Rev. B* **39,** 12682–12687 (1989).

79. Klein, M., Ganguly, B. & Colwell, P. Theoretical and Experimental Study of Raman Scattering from Coupled LO-Phonon-Plasmon Modes in Silicon Carbide. *Phys. Rev. B* **6,** 2380–2388 (1972).

80. Li, Y. B., Ferguson, I. T., Stradling, R. A. & Zallen, R. Raman scattering by plasmon-phonon modes in highly doped n-InAs grown by molecular beam epitaxy. *Semicond. Sci. Technol.* **7,** 1149–1154 (1992).

81. Irmer, G., Wenzel, M. & Monecke, J. Light scattering by a multicomponent plasma coupled with longitudinal-optical phonons: Raman spectra of p-type GaAs:Zn. *Phys. Rev. B* **56,** 9524–9538 (1997).

82. Gaur, N. K. S. Longitudinal optical phonon-plasmon coupling in InSb and InAs. *Phys. B+C* **82,** 262–270 (1976).

83. Hon, D. T. & Faust, W. L. Dielectric parameterization of raman lineshapes for GaP with a plasma of charge carriers. *Appl. Phys.* **1,** 241–256 (1973).

84. Irmer, G. *et al.* Determination of the hole concentration and mobility of p-GaP by Hall and by Raman measurements. *Semicond. Sci. Technol.* **6,** 1072–1078 (1991).

85. Mlayah, A., Carles, R., Landa, G., Bedel, E. & Muñoz-Yagüe, A. Raman study of longitudinal optical phonon-plasmon coupling and disorder effects in heavily Be-doped GaAs. *J. Appl. Phys.* **69,** 4064 (1991).

86. Demangeot, F. *et al.* Raman scattering by the longitudinal optical phonon in InN: Wave-vector nonconserving mechanisms. *Phys. Rev. B* **71,** 104305 (2005).

87. Cardona, M. & Guntherodt, G. *Light Scattering in Solids IV.* **54,** (Springer Berlin Heidelberg, 1984).

88. Jeganathan, K. *et al.* Raman scattering of phonon-plasmon coupled modes in self-assembled GaN nanowires. *J. Appl. Phys.* **105,** 123707 (2009).

89. Jeganathan, K., Purushothaman, V., Debnath, R. K., Calarco, R. & Luth, H. Raman scattering on intrinsic surface electron accumulation of InN nanowires. *Appl. Phys. Lett.* **97,** 093104 (2010).

90. Ketterer, B., Arbiol, J. & Fontcuberta i Morral, A. Phonon confinement and plasmon-phonon interaction in nanowire-based quantum wells. *Phys. Rev. B* **83,** 245327 (2011).

91. Patel, C. & Slusher, R. Light Scattering by Plasmons and Landau Levels of Electron Gas in InAs. *Phys. Rev.* **167,** 413–415 (1968).

92. Cardona, M. *Light Scattering in Solids I.* **8,** (Springer Berlin Heidelberg, 1983).

93. Buchner, S. & Burstein, E. Raman Scattering by Wave-Vector—Dependent LO-Phonon—Plasmon Modes in n-InAs. *Phys. Rev. Lett.* **33,** 908–911 (1974).

94. Jiang, X. *et al.* InAs/InP Radial Nanowire Heterostructures as High Electron Mobility Devices. *Nano Lett.* **7,** 3214–3218 (2007).

95. Lauhon, L. J., Gudiksen, M. S. & Lieber, C. M. Semiconductor nanowire heterostructures. *Philos. Trans. A. Math. Phys. Eng. Sci.* **362,** 1247–60 (2004).

96. Mori, M., Murata, K., Fujimoto, N., Tatsuyama, C. & Tambo, T. Effect of AlSb buffer layer thickness on heteroepitaxial growth of InSb films on a Si(001) substrate. *Thin Solid Films* **515,** 7861–7865 (2007).

97. Chyi, J.-I. *et al.* Molecular beam epitaxial growth and characterization of InSb on Si. *Appl. Phys. Lett.* **54,** 1016 (1989).

98. Larsson, M. W. *et al.* Strain mapping in free-standing heterostructured wurtzite InAs/InP nanowires. *Nanotechnology* **18,** 015504 (2007).

99. Huang, Y. & Lieber, C. M. Integrated nanoscale electronics and optoelectronics: Exploring nanoscale science and technology through semiconductor nanowires. *Pure Appl. Chem.* **76,** 2051–2068 (2004).

100. Haraguchi, K., Katsuyama, T., Hiruma, K. & Ogawa, K. GaAs p-n junction formed in quantum wire crystals. *Appl. Phys. Lett.* **60,** 745 (1992).

101. Wu, Y., Fan, R. & Yang, P. Block-by-Block Growth of Single-Crystalline Si/SiGe Superlattice Nanowires. *Nano Lett.* **2,** 83–86 (2002).

102. Björk, M. T. *et al.* Nanowire resonant tunneling diodes. *Appl. Phys. Lett.* **81,** 4458 (2002).

103. Nilsson, H. A. *et al.* A radio frequency single-electron transistor based on an InAs/InP heterostructure nanowire. *Nano Lett.* **8,** 872–5 (2008).

104. Borgström, M. T., Zwiller, V., Müller, E. & Imamoglu, A. Optically bright quantum dots in single Nanowires. *Nano Lett.* **5,** 1439–43 (2005).

105. Lind, E., Persson, A. I., Samuelson, L. & Wernersson, L.-E. Improved subthreshold slope in an InAs nanowire heterostructure field-effect transistor. *Nano Lett.* **6,** 1842–6 (2006).

106. Borgström, M. T., Verheijen, M. A., Immink, G., Smet, T. de & Bakkers, E. P. A. M. Interface study on heterostructured GaP-GaAs nanowires. *Nanotechnology* **17,** 4010–3 (2006).

107. Gudiksen, M. S., Lauhon, L. J., Wang, J., Smith, D. C. & Lieber, C. M. Growth of nanowire superlattice structures for nanoscale photonics and electronics. *Nature* **415,** 617–20 (2002).

108. Björk, M. T. *et al.* One-dimensional heterostructures in semiconductor nanowhiskers. *Appl. Phys. Lett.* **80,** 1058 (2002).

109. Samuelson, L. *et al.* Semiconductor nanowires for novel one-dimensional devices. *Phys. E Low-dimensional Syst. Nanostructures* **21,** 560–567 (2004).

110. Dick, K. A. *et al.* The morphology of axial and branched nanowire heterostructures. *Nano Lett.* **7,** 1817–22 (2007).

111. Paladugu, M. *et al.* Nature of heterointerfaces in GaAs/InAs and InAs/GaAs axial nanowire heterostructures. *Appl. Phys. Lett.* **93,** 101911 (2008).

112. Ohlsson, B. . *et al.* Growth and characterization of GaAs and InAs nano-whiskers and InAs/GaAs heterostructures. *Phys. E Low-dimensional Syst. Nanostructures* **13,** 1126–1130 (2002).

113. Paladugu, M. *et al.* Novel growth phenomena observed in axial InAs/GaAs nanowire heterostructures. *Small* **3,** 1873–7 (2007).

114. Venkatesan, S. *et al.* Direct observation of interface and nanoscale compositional modulation in ternary III-As heterostructure nanowires. *Appl. Phys. Lett.* **103,** 063106 (2013).

115. Messing, M. E. *et al.* Growth of straight InAs-on-GaAs nanowire heterostructures. *Nano Lett.* **11,** 3899–905 (2011).

116. Dick, K. A., Bolinsson, J., Borg, B. M. & Johansson, J. Controlling the abruptness of axial heterojunctions in III-V nanowires: beyond the reservoir effect. *Nano Lett.* **12,** 3200–6 (2012).

117. Ferry, D. *Quantum Mechanics: An Introduction for Device Physicists and Electrical Engineers, Second Edition.* (CRC Press, 2001).

118. S.M.Sze. *Physics of Semiconductor Devices.* (Wiley, 1981).

119. Dahl Nissen, P. *et al.* Comparison of gate geometries for tunable, local barriers in InAs nanowires. *J. Appl. Phys.* **112,** 084323 (2012).

120. Palankovski, V. Simulation of Heterojuntion Bipolar Transistors. (2000).

121. Nam, H. *et al.* Electronic subband structure in InAs-GaAs quantum dots in an asymmetric-well infrared photodetector structure. (2005).

122. Bhattacharya, P. Properties of Lattice-Matched and Strained Indium Gallium Arsenide EMIS Datareviews Series.

123. Adachi, S. Material parameters of In1−xGaxAsyP1−y and related binaries. *J. Appl. Phys.* **53,** 8775 (1982).

124. Ji, G. *et al.* Optical investigation of highly strained InGaAs-GaAs multiple quantum wells. *J. Appl. Phys.* **62,** 3366 (1987).

125. O'Reilly, E. P. Valence band engineering in strained-layer structures. *Semicond. Sci. Technol.* **4,** 121–137 (1989).

126. DeSalvo, G. C. Etch Rates and Selectivities of Citric Acid/Hydrogen Peroxide on GaAs, Al0.3Ga0.7As, In0.2Ga0.8As, In0.53Ga0.47As, In0.52Al0.48As, and InP. *J. Electrochem. Soc.* **139,** 831 (1992).

127. Christesen, J. D., Pinion, C. W., Grumstrup, E. M., Papanikolas, J. M. & Cahoon, J. F. Synthetically encoding 10 nm morphology in silicon nanowires. *Nano Lett.* **13,** 6281–6 (2013).

128. Schukfeh, M. I. *et al.* Formation of nanogaps in InAs nanowires by selectively etching embedded InP segments. *Nanotechnology* **25,** 465306 (2014).

129. Kallesøe, C. *et al.* Integration, gap formation, and sharpening of III-V heterostructure nanowires by selective etching. *J. Vac. Sci. Technol. B Microelectron. Nanom. Struct.* **28,** 21 (2010).

130. Thelander, C. *et al.* Electron transport in InAs nanowires and heterostructure nanowire devices. *Solid State Commun.* **131,** 573–579 (2004).

131. Mohney, S. E. *et al.* Measuring the specific contact resistance of contacts to semiconductor nanowires. *Solid. State. Electron.* **49,** 227–232 (2005).

132. Stern, E., Cheng, G., Young, M. P. & Reed, M. A. Specific contact resistivity of nanowire devices. *Appl. Phys. Lett.* **88,** 053106 (2006).

133. Wang, Z. L. *Nanowires and Nanobelts. Materials, Properties and Devices. Springe* (2003).

134. Dahl Nissen, P. Spin Qubits in GaAs hetrostructures and gating of InAs nanowires for low-temperature measurements. (2012).